T2R2 東京科学大学 リサーチリポジトリ
Science Tokyo Research Repository

論文 / 著書情報
Article / Book Information

題目(和文)	共鳴トンネルダイオードテラヘルツ発振素子の高周波化に関する研究
Title(English)	Study of Resonant-Tunneling-Diode Terahertz Oscillators for High Frequency
著者(和文)	金谷英敏
Author(English)	Hidetoshi Kanaya
出典(和文)	学位:博士(工学), 学位授与機関:東京工業大学, 報告番号:甲第10035号, 授与年月日:2015年12月31日, 学位の種別:課程博士, 審査員:淺田 雅洋,小山 二三夫,植之原 裕行,渡辺 正裕,宮本 智之,内田 貴司
Citation(English)	Degree:Doctor (Engineering), Conferring organization: Tokyo Institute of Technology, Report number:甲第10035号, Conferred date:2015/12/31, Degree Type:Course doctor, Examiner:,,,,,
学位種別(和文)	博士論文
Type(English)	Doctoral Thesis

Powered by T2R2 (Science Tokyo Research Repository)

Tokyo Institute of Technology

Doctor Thesis

Study of Resonant-Tunneling-Diode Terahertz Oscillators for High Frequency

December 2015

Directed by Professor Masahiro Asada

Department of Electronics and Applied Physics
Interdisciplinary Graduate School of Science and Engineering

Hidetoshi Kanaya

Contents

Chapter 1
Introduction

1.1 Introduction

The terahertz (THz) range is between approximately 100 GHz and 10 THz, or the top edge of the millimeter wave range and the bottom edge of the optical wave range, and has been almost unutilized because of a lack of compact sources. However, recent technological innovations in nanotechnology for electronics and photonics are enabling terahertz research and applications, including those in the fields of ultrahigh-speed wireless communication, imaging, and spectroscopy.

I studied ways to achieve a compact terahertz source for terahertz applications by developing resonant-tunneling-diode (RTD) terahertz oscillators. This chapter first discusses the unique features of the terahertz frequency range, along with some applications. Next, the candidates for terahertz sources with those characteristics are described. The advantages of RTDs are compared with those of other devices, and the development history of RTD oscillators is reviewed. Finally, the purpose and outline of this thesis are shown.

1.2 General introduction of terahertz band

The term “terahertz band” is broadly applied to the submillimeter-wave range that covers the frequencies between approximately 100 GHz and 10 THz (3 mm to 30 μm and 3.3 cm^{-1} to 330 cm^{-1}), as shown in Fig. 1.1. This frequency region has a photon energy range of 0.4–40 meV. The terahertz frequency band exists between the upper limit of the millimeter wave band and the lower limit of the optical wave band. The terahertz frequency range has received considerable attention because of its unique features [1.1–5].

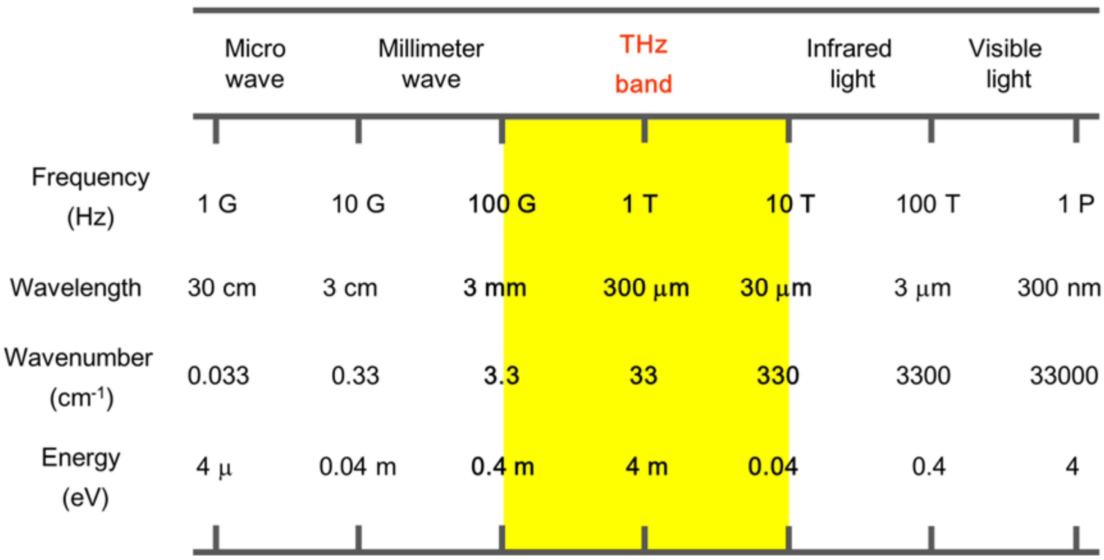

Fig 1.1　Explanation of terahertz band and its characteristics.

Some of these unique features and applications are discussed in this chapter. Terahertz electric fields strongly interact with polar substances but penetrate those that are non-polar. Thus, the absorption spectra of many polar molecules such as H_2O, CO_2, N_2, and O_2 have many distinct spectral peaks in the terahertz range. Fig. 1.2 shows the atmospheric loss caused by attenuation in the terahertz region, as calculated by the National Institute of Information and Communication Technology (NICT), Japan. This calculation shows transmission windows that can be used for wireless communication.

Much of the interest in terahertz applications has centered on terahertz imaging and spectroscopy [1.6–58]. The imaging and spectroscopy of numerous materials are utilized in many research areas, including biology, pharmacology, medical science, non-destructive evaluation, material science, environment monitoring, security, astronomy, and art. Moreover, terahertz communication is able to send or receive a huge quantity of information. Terahertz signals are expected to be used as information carriers with the ability to send around 1 Tbps, similar to optical communication systems. This area of research is now being developed and is expected to become the next frontier of wireless communication [1.59–69].

Compact sources that can increase the usability and reduce the cost are needed to develop various applications in the terahertz frequency range. Electronic solid-state sources based on semiconductors are some of the candidates and are now being intensively developed.

Compact optical sources (i.e., solid-state lasers like p-Ge and quantum cascade lasers) operate at an energy level of several milli-electron volts, which is comparable to that of lattice phonons at room temperature. Thus, cryogenic cooling is needed to resolve this problem.

Recent technological innovations in electronics and photonics are enabling terahertz research and numerous applications, including those in ultrahigh-speed wireless communication, imaging, and spectroscopy, as shown in the next section.

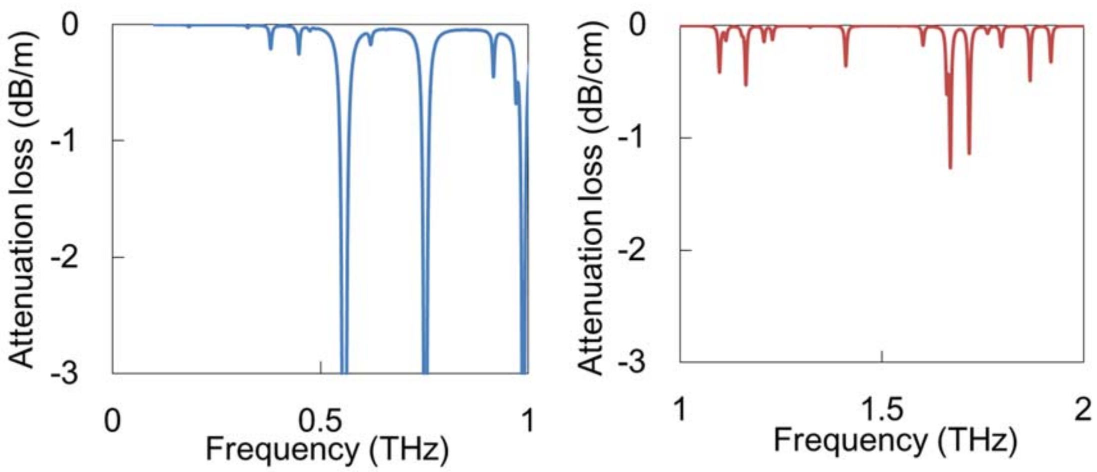

Fig 1.2 Atmospheric attenuation of terahertz region. The data was calculated by Amaterasu offered by NICT

1.3 Terahertz applications

1.3.1 Wireless communication

Everything will connect to the Internet in the future [1.61]. Information and communication technology has a large market potential. The information flow in modern society is accelerating, and the carrier frequencies used for signals continue to increase. Fiber-linked optical communication is successfully growing, realizing data rates exceeding a terabyte per second, whereas the data rate of wireless communication remains low compared to that of optical communication. The realization of terahertz wireless communication would be of great benefit to society by enabling high-performance wireless connections for applications such as chip-to-chip communication, touch-and-go downloading, body-area networks, wireless hot spots, and cell phone bases mounted on telephone poles, which are mentioned in the THz communication reviews of Refs. 1.62, 63, 65, and 69.

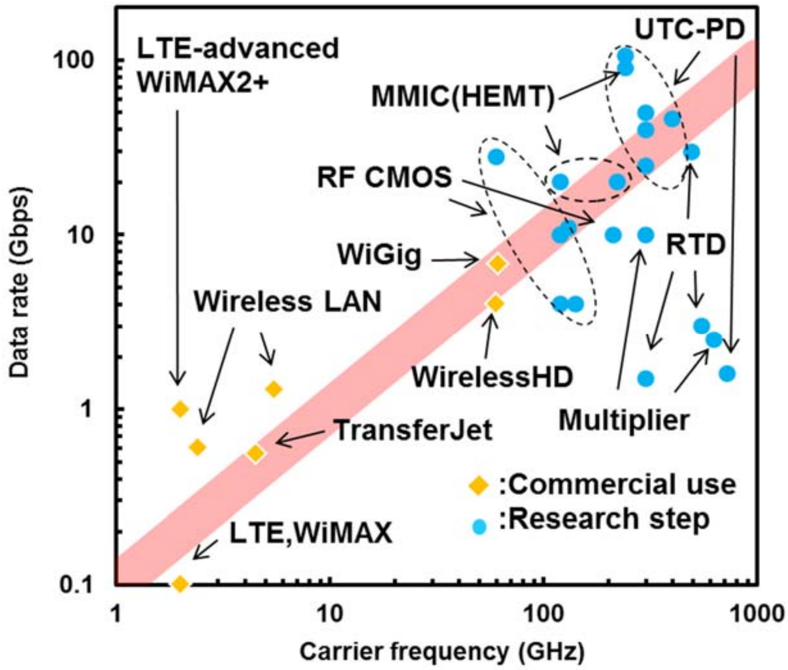

Fig 1.3 Recent progress of wireless communication data rate as a function of carrier frequency in THz range.

As a famous example, 120-GHz-band millimeter-wave wireless links using uni-traveling-carrier photodiodes (UTC-PDs) integrated with high-electron mobility transistor (HEMT) monolithic microwave integrated circuits (MMICs) have been developed, and field tests have demonstrated operations at over 10 Gbps [1.60]. This system of wireless communication was used to transfer data for high-definition television (high-vision) at the XXIX Olympiad in Beijing.

Because of the previously mentioned atmospheric attenuation, short-range (<10 m) communication has been expected using frequencies of less than 1 THz, whereas near-field communication such as for touch-and-go systems (<10 cm) has been expected for frequencies of about 1–2 THz, depending on the low-attenuation windows in the atmosphere. An estimation of wireless communication at a carrier frequency of 1.5 THz is shown in Fig. 1.4, based on Friis' law. A transmission rate of more than several tens of giga-bits per second over several centimeters is expected, with an output power is 0.1 μW and transmitter and receiver antenna gains of 20 dB. The required signal-to-noise ratio is 15 dB. This equals a bit error rate of 2×10^{-3}, which is the limit of forward error correction. The noise figure of the receiver-side amplifier is assumed to be 13 dB, and the transition loss is ignored at this frequency range.

Furthermore, a rate of more than 1 Tbps is expected with about 30 channels at approximately 50 Gbps per channel in a frequency range of less than 2 THz by applying a frequency division diplex scheme, as shown in Fig. 1.5. If orthogonal polarization multiplexing is used, the data rate will double.

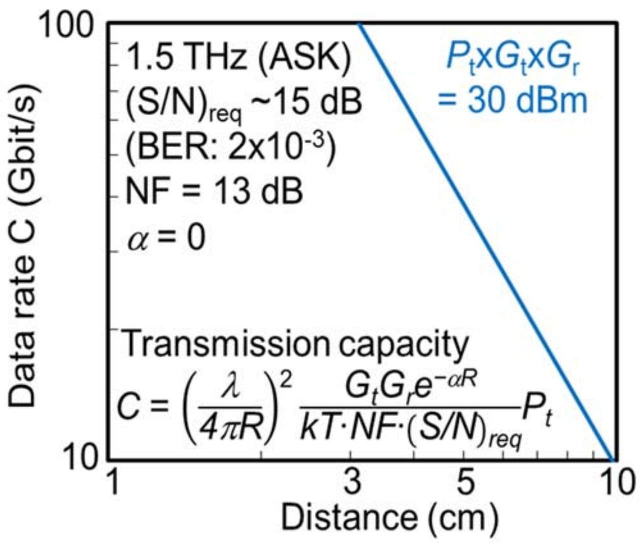

Fig. 1.4 Examples of transmission capacity as a function of distance.

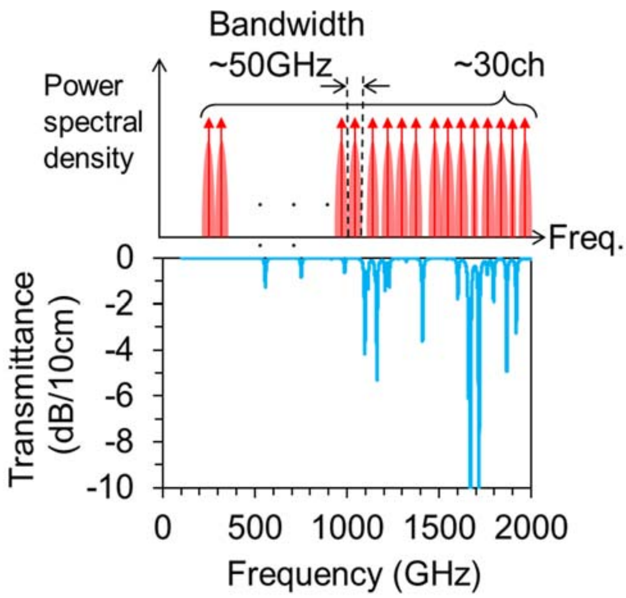

Fig. 1.5 Examples of frequency division duplex under 2 THz.

1.3.2 Imaging

Terahertz waves can penetrate various materials, including paper, clothes, plastics, and leaves. It is difficult to detect these soft materials using X-rays. The resolution of terahertz imaging is better than that of millimeter wave imaging because the terahertz wavelength is smaller than that of millimeter waves. These features are attractive for the non-destructive testing and non-invasive inspection of various opaque materials for obtaining the internal structure. Imaging in the terahertz range has been developed for various areas applications, including plastic card inspection using a backward-wave oscillator [1.18]. Soft material imaging such as a red pepper and prawn [1.19], real-time standoff imaging using a quantum cascade laser [1.28] , noninvasive mail inspection systems [1.39], waveguide-based all-electronic imaging [1.41], food inspection [1.49], and terahertz imaging with silicon MOSFETs [1.54] have also been reported. Many groups of researchers and enterprises have worked hard to explore the attractive terahertz region. The required imaging quality, including the resolution, area, and acquisition time, depend on the items being inspected. However, a sub-millimeter resolution (300 μm at 1 THz) will be satisfactory for numerous applications such as searching for foreign materials in food and packaging, penetrating the thickness of a coating such as in medicine and the automobile industry, and medial disease investigations such as searching for tumors.

A schematic of an imaging system transmission is shown in Fig. 1.6. The noise-equivalent power of the detector is assumed to be 20 pW/$\sqrt{\text{Hz}}$. The pixel number is set at 320 × 240. The required signal-to-noise ratio is assumed to be 30 dB. The time constant is set at 100 ms. Under these conditions, the required power is more than 1 mW.

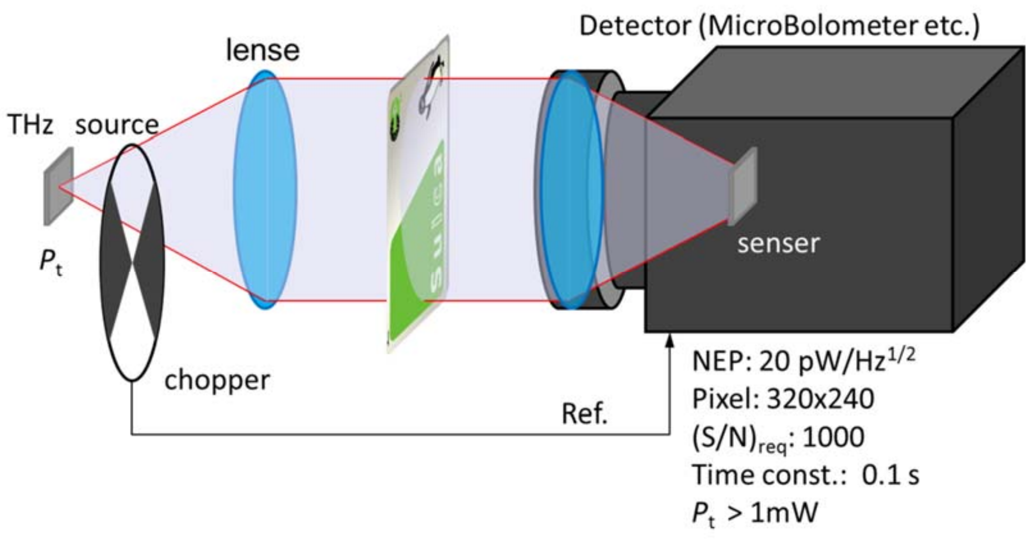

Fig. 1.6 Schematic of imaging system transmission.

1.3.3 Spectroscopy

Just as in the development of imaging applications, terahertz spectroscopy has also been the focus of intensive research to develop numerous applications, including those in the fields of security, pharmacology, and biology. Research has been conducted on inspection methods for illicit drugs and explosives. Similar research has been reported in the security field. In the biochemistry field, carcinoma investigation was researched.

There are many fingerprint frequencies for major drugs and explosives especially in the 1–2 THz range according to J. F. Federici et al. in Ref. 1.24 (2005), as listed in Table 1.1. Thus, to prevent drug related crime and terrorism, a 2-THz oscillator is required, especially in the inspection field for these items. The first fingerprints of major drugs and explosives in the 0–10 THz range are also shown in Fig. 1.7, which are the lowest fingerprints of each material as described in Ref. 1.24.

In Fig 1.8, an example of a transmission spectroscopy system is shown. The required signal-to-noise ratio is assumed to be 40 dB. The rock-in technique is used, and the time constant is 100 ms. A noise equivalent power (NEP) of 100 pW/$\sqrt{\mathrm{Hz}}$ is normally used as the value of a commercialized Shottkey barrier diode detector. In this theoretical calculation, the required output power is estimated to be about 1 μW.

In Fig. 1.9, an example of a reflection spectroscopy system is shown. The lens diameter, focal point, and spot diameter are set at 5 cm, 5 cm, and 0.5 mm at 0.5 THz, respectively. The reflection loss and frame rate are simply assumed to be 40 dB and 30 fps, respectively. In this estimation, an increase in output power is needed for a real-time reflection application.

Table. 1.1 Specific finger print of major explosive and drugs according to J. F. Federici, et al. in Ref. 1.24.

material	Fingerprint frequency [THz]							type
Semtex-H	0.72	1.29	1.73	1.88	2.15	2.45	2.57	explosive
PE4	0.72	1.29	1.73	1.94	2.21	2.48	2.69	explosive
RDX/ C4	0.72	1.26	1.73					explosive
PETN[a]	1.73	2.51						explosive
PETN[b]	2.01							explosive
HMX[a]	1.58	1.91	2.21	2.57				explosive
HMX[b]	1.84							explosive
TNT[a]	1.44	1.91						explosive
TNT[b]	1.7							explosive
TNT	5.6	8.2	9.1	9.9				explosive
NH_4NO_3	4	7						explosive
Methamphetamine	1.2	1.7						drug
MDMA	1.4	1.8						drug
Lactose α-monohydrate	0.54	1.2	1.38	1.82	2.54	2.87	3.29	drug
Icing sugar	1.44	1.61	1.82	2.24	2.57	2.84	3.44	drug
Co-codamol	1.85	2.09	2.93					drug
Aspirin/ soluble	1.38	3.26						drug
Aspirin/caplets	1.4	2.24						drug
Acetaminophen	6.5							drug
Terfenadine	3.2							drug
Naproxen sodium	5.2	6.5						drug

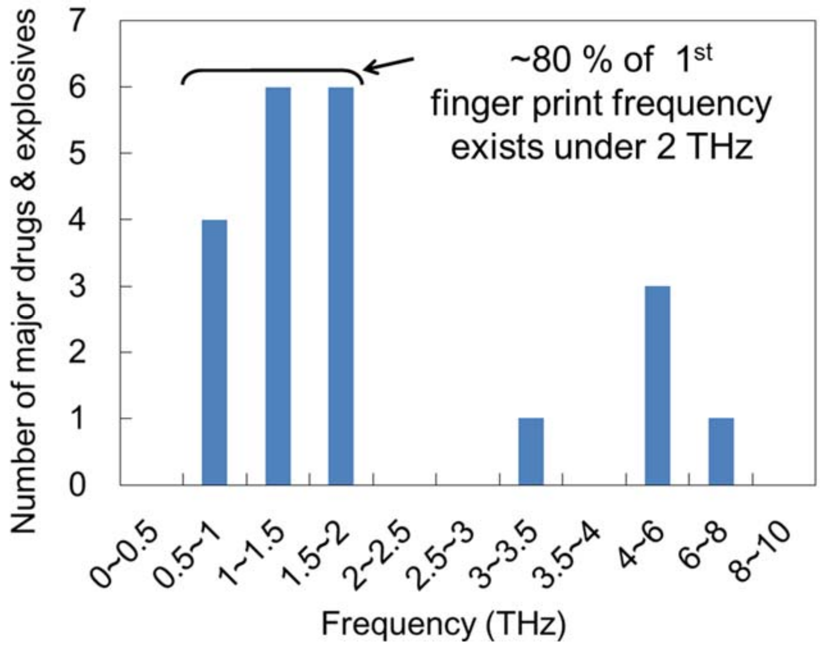

Fig. 1.7 The number of 1st finger print in major drugs and explosives from 0 to 10 THz described in Ref. 1.24.

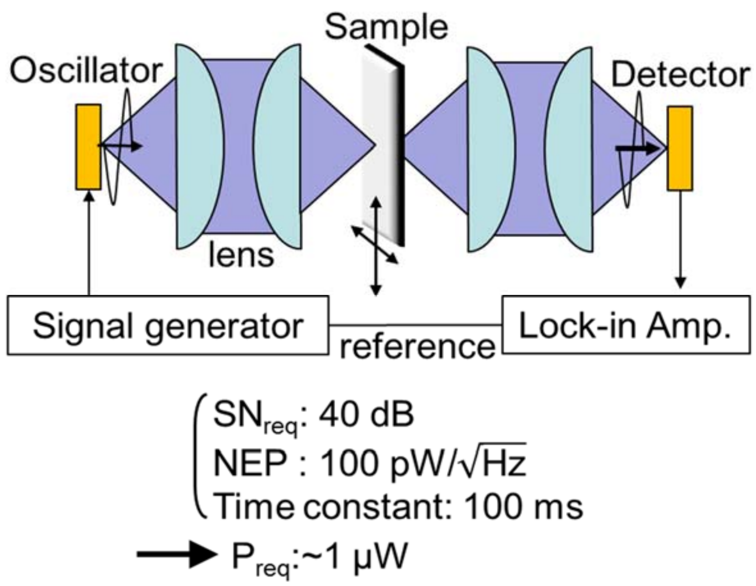

Fig 1. 8 Schematic measurement system of transmission spectroscopy.

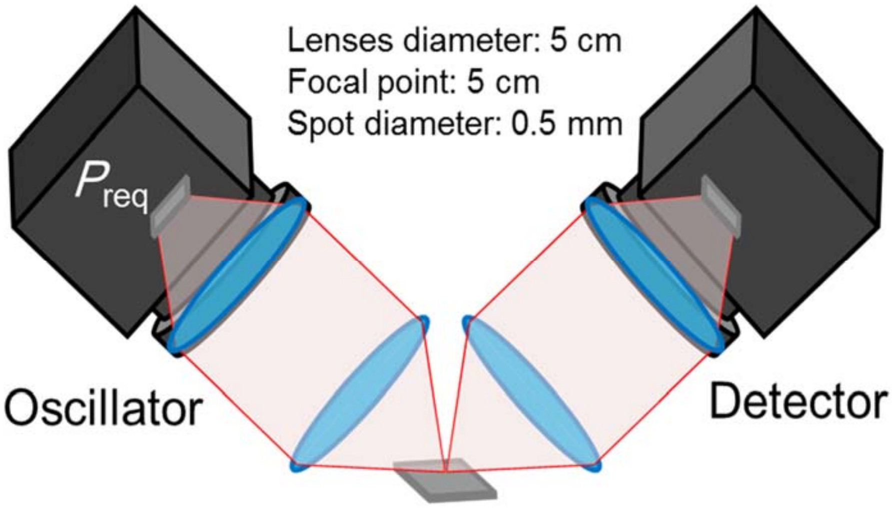

Fig 1.9 Schematic diagram of reflection sensing.

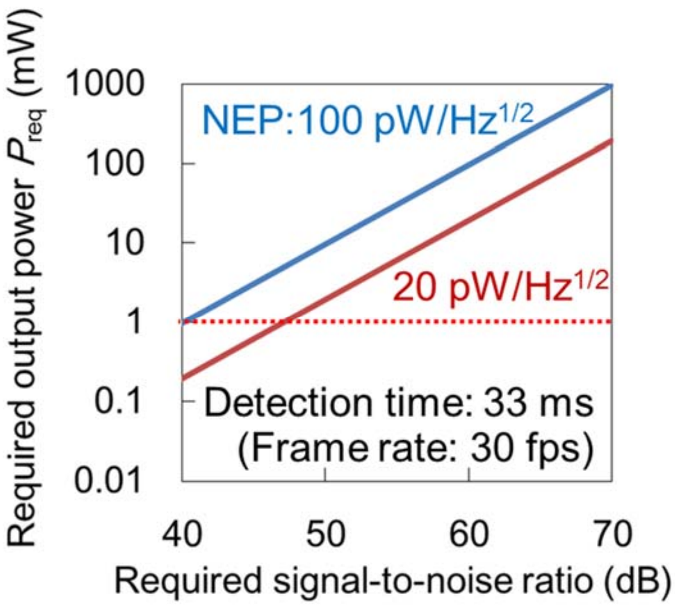

Fig 1.10 Required output power versus required signal-to-noise-ratio with the NEP of 100 and 20 pW/$\sqrt{\text{Hz}}$.

1.4 Terahertz sources

A variety of techniques for generating terahertz frequencies have been demonstrated using gas lasers; free-electron lasers; gyrotrons; optical mixing in nonlinear crystals such as DAST and $LiNbO_3$; photomixing with uni-traveling carrier photodiodes, which used optical difference frequency mixing in a photoconductor coupled to an RF radiator; femtosecond laser pulsing and photoconductive antennas, which are often used in a terahertz time domain system (THz-TDS); and Schottky-diode-based multiplier circuits with a waveguide [1.70-90]. Good progress is being made on these types of sources, with especially good features from the perspective of output power. However, because they are slightly bulky, they are not yet ideal for terahertz applications. Some of these technology such as systems of THz-TDS or optical frequency mixing in a photoconductor coupled to an RF radiator have been commercialized, but they are slightly expensive because of the high cost of laser systems. The oscillation frequencies, output power values, and some features of these sources are listed in Table 1.2, and these specifications are compared from the viewpoint of the previously mentioned application. Among these sources, solid-state sources can only be the candidates for compact sources.

Table 1.2 Frequency, output power, and size of major THz sources.

Technology		Frequency (THz)	output power (mW)	Size	
fs-laser & photoconductive antenna		○ (broad, <10)	△ (<0.3)	△	table top
Nd:YAG laser & Nonlinercrystal (is-TPG)		○ (<3)	○ (50 kW peak)	△	
UTC-PD		△ (<2)	○ (<10)	△	
Multiplying of microwave		○ (<2.7)	○ ($\lesssim$1)	△	
Free electron laser		○	○	×	floor size
BWO		△ (<1.5)	○ (<100)	×	high voltage & cooling needed
Solid-state source	Opt-electronics	△	○	○	low temperature
	Electronics	△	△	◎	

Terahertz solid single oscillators with a compact size in 2015 including the results of this thesis are shown in Fig 1.11. On the optical device side, p-Ge lasers and terahertz quantum cascade lasers [1.91–97] are being studied. A p-Ge laser has high power, but requires a magnetic field. The quantum cascade laser (QCL) was first developed in 1994, and it had a lasing frequency of about 70 THz. After much research, this was followed by a demonstration at 4.4 THz in 2002. The terahertz waves are emitted using electron relaxation between the sub-bands of quantum wells, such as between several GaAs layers that are a few nanometers thick separated by AlGaAs barriers, whose emission blocks are serially connected to generate the terahertz frequency. The main operational methods are referred to as “chirped superlattice,” “bound-to-continuum,” “resonant-phonon,” and “hybrid/interlaced.” The difference is the mechanism by which the electrons scatter after the terahertz-photon emission from the inversion of the population. The continuous-wave (cw) emission power is around 1 to 100 mW. At present, lasing frequencies as low as 1.2 THz with pulsed mode operation up to 69 K and cw mode operation at 10 K have been achieved in a bound-to-continuum THz-QCL. For high-temperature performance, improvements in the active regions and waveguides have brought the maximum operation temperature up to 169 K in the pulsed mode at 2.9 THz and 200 K at 3.2 THz. However, room-temperature operation at about 1 THz seems to be difficult. To achieve the goal of room temperature operation, new designs for structures are being intensively studied [1.97]. Although this approach has made room temperature operation possible, the power consumption is very high.

In the superconductor device field, a high-temperature superconducting $Bi_2Sr_2CaCu_2O_{8+d}$ intrinsic Josephson junction (IJJ) emitter is being investigated. This source is tunable and can generate a frequency range of 0.5–2.4 THz at temperatures of less than 40 K [1.98, 99].

On the electron device side, two-terminal devices are being developed, including impact ionization avalanche transit-time (IMPATT) diodes, tunneling transit-time (TUNNETT) diodes, and Gunn diodes. Devices based on the plasma effect, Bloch oscillation, and velocity modulation are also being studied for terahertz oscillators and amplifiers [1.100–111].

The cutoff frequency and maximum oscillation frequency of transistors are also moving toward the terahertz range [1.112–127]. In particular, InP-based transistors such as heterojunction bipolar transistors (HBTs) and high electron mobility transistors (HEMTs) have rapidly been developed in recent years. HBT and HEMT oscillators have shown great success in microwave, millimeter-wave, and terahertz-wave applications. Both device technologies are excellent approaches for operation in the terahertz band.

InP-based HEMTs and HBTs have held the frequency response record, as assessed by the cutoff frequency f_t and maximum oscillation frequency f_{max}. Recent reports have shown f_t values of 750 GHz in pseudomorphic InGaAs/InP HBTs and 660 GHz in InAs composite channel HEMTs, along with f_{max} values of 1.1 THz in DHBTs and 1.5 THz in InAs/InGaAs composite channel HEMTs. These results have been achieved by combining downscaling of the minimum feature size, especially the gate length, and a reduction in parasitic elements such as the series resistance and stray capacitance.

MMIC amplifiers and oscillators using high-speed HEMTs and HBTs have been studied and developed to increase f_t and f_{max}. Such oscillators have demonstrated values of up to 350 GHz for an InP HEMT, with an f_{max} value of 0.6 THz [1.120], and up to 570 GHz for an InP HBT, with an f_{max} value greater than 800 GHz [1.117]. Recently, an amplifier that could handle frequencies greater than 1 THz was reported by the research group of the Northrop Grumman Corp. [1.127].

There have been rapid increases in the development of silicon technology [1.128–133]. Signal generation at 0.54 THz with 40-nm bulk CMOS technology [1.132] and 0.53-THz oscillation with 1 mW by a 0.13-μm SiGe BiCMOS using an array configuration have been reported [1.133].

RTD oscillators for the terahertz range are being pursued [1.134–168]. After fundamental oscillation at 1.04 THz was reported in an RTD oscillator, the progress on the oscillation frequency accelerated [1.153]. When this study began in 2011, the highest frequency was achieved in an experiment using a single semiconductor electronic oscillator. The next section discusses our research on RTD terahertz oscillators. For the applications in section 1.3, light sources for frequencies up to 2 THz were required, as previously described.

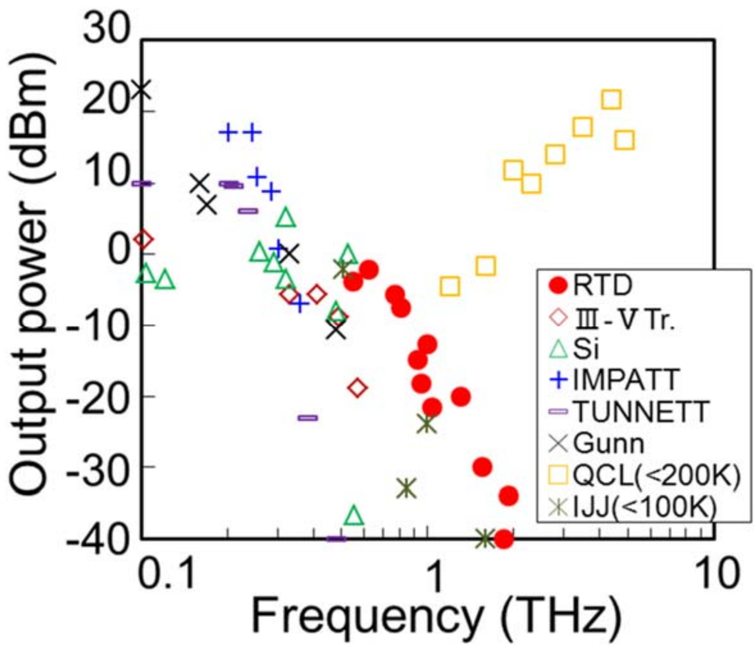

Fig 1.11 Output power as a function of frequency of solid-state terahertz sources in 2015

1.5 Resonant-tunneling-diode terahertz oscillators

RTDs have the highest oscillation frequency among the previously mentioned electron devices. Room-temperature operation is an attractive feature because it has not yet been achieved in a single optical device with low power consumption. The research on RTDs began with a theoretical prediction by Tsu and Esaki in 1973 [1.134], and their negative differential resistance behavior was experimentally demonstrated at liquid-nitrogen-cooled temperatures in 1974 [1.135] and at room temperature in 1985 [1.138]. Oscillation in the microwave range was demonstrated at a low temperature in

1984 [1.137] and at room temperature in 1985 [1.139]. The oscillation frequency has been updated many times to reach several hundred gigahertz until the early 1990s, as shown in Fig 1.12. In 1987, millimeter-wave fundamental oscillation at 56 GHz with a second harmonic of 87 GHz was observed at room temperature in an AlGaAs/GaAs RTD. A rectangular waveguide resonator was used to generate terahertz oscillations with an RTD [1.140]. In 1988, fundamental oscillation up to 200 GHz was obtained in an AlAs/GaAs RTD [1.143]. Submillimeter oscillation at 420 GHz was achieved in a high-current-density RTD as a result of its thin AlAs barrier in 1989 [1.145]. In 1991, fundamental oscillation at 712 GHz was reported using an InAs/AlSb RTD [1.147] A 64-element arrayed oscillator containing RTDs has been reported, with an oscillation at 650 GHz using an output power of 2–3 μW [1.150]. GaInAs/AlAs RTDs on InP wafers are used in an arrayed oscillator.

In our group's study, fundamental oscillation at 587 GHz with an output power of 8 μW using GaInAs/AlAs RTDs integrated with the planar circuit of a slot antenna has been achieved. A third harmonic of 1.02 THz with a fundamental component of 342 GHz was reported [1.151]. The VCO characteristics of a sub-terahertz oscillating RTD were demonstrated and calculated theoretically [1.152]. A fundamental oscillation of 1.04 THz has been achieved with an increase in the current density associated with a decrease in the barrier thickness and increase in the emitter doping [1.153]. The recent results are shown in Refs. 1.154–168.

For wireless communication applications, a data rate of 2 Gbps was demonstrated [1.158]. An RTD can operate at over 30 GHz with a structure improvement of modulation circuit [1.165]. In addition, an RTD can change the oscillation frequency using varactor diodes [1.166], because the capacitance of varactor diodes are independently controlled by the bias voltage.

Based on these studies, RTDs have the potential of being used for terahertz light sources in many terahertz applications. In the numerous applications discussed in section 1.3, light sources that can operate at frequencies of at least 2 THz are required, as previously described.

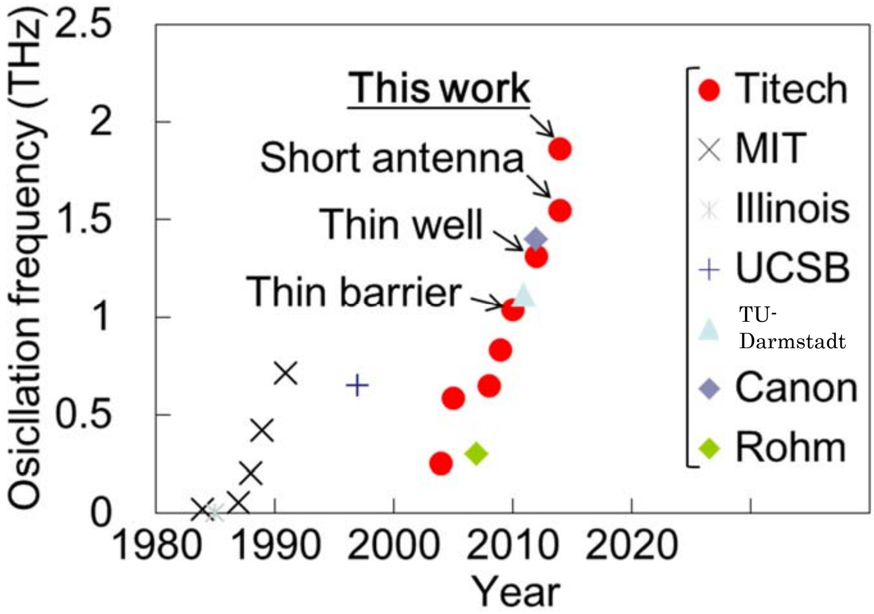

Fig 1.12 The history of increase in oscillation frequency for RTD oscillators

1.6 Purpose and outline of this thesis

A summary of my research on the increases in the oscillation frequency of RTD oscillators is shown in Fig. 1.12. RTDs have application potential as compact sources at room temperature. The frequency performance of RTD oscillators has not yet been sufficient for terahertz applications such as spectroscopy, as shown in section 1.3.

Therefore, this study had the purpose of developing a “resonant-tunneling-diode terahertz oscillators for high frequency” to realize compact terahertz sources for various terahertz applications. The target value for the oscillator frequency was 2 THz. The outline of this study is shown in Fig. 1.13.

In Chapter 2, a proposal is given for achieving high-frequency oscillation by reducing the total delay time. The factors for increasing the oscillation frequency are mentioned, including the intrinsic and extrinsic times, and the antenna structure. In Chapter 3, the high-frequency oscillation achieved by reducing the dwell time is discussed, based on the principal of tunneling in quantum mechanics. In Chapter 4, the argument for achieving high-frequency oscillation by reducing the transit time through the optimization of the collector-spacer thickness is given. Chapter 5 discusses the integration of the well and spacer improvements, RTD series resistance, and antenna structure changes to achieve a higher frequency, and the estimated oscillation characteristics are analyzed and a preliminary work with some improvements discussed in this chapter is shown. Chapter 6 provides the conclusions of this study.

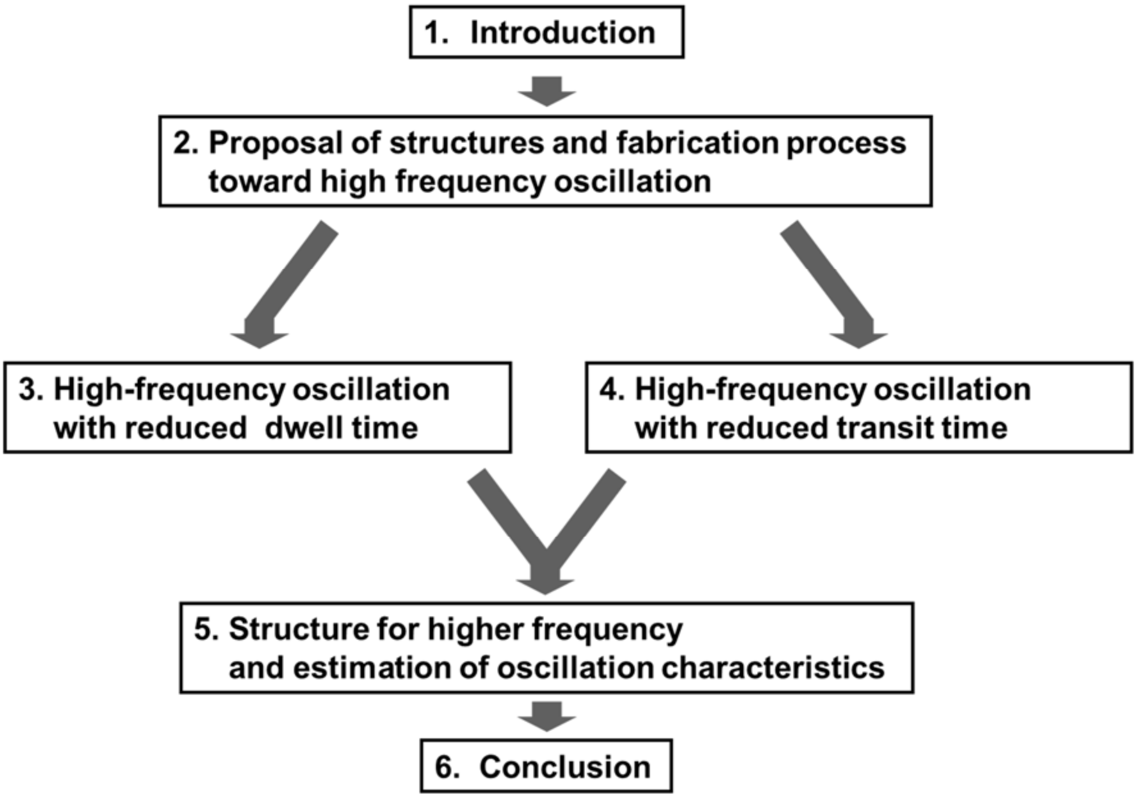

Fig 1.13 Outline of this thesis

Chapter 2
Proposal of structures and fabrication process toward high frequency oscillation

2.1 Introduction

This chapter explains the device structure, fabrication process, and principal oscillation of RTD-terahertz oscillators. I first explain the structure and fabrication process of a RTD-terahertz oscillator. Next, I describe the total delay time, which consists of the intrinsic delay and extrinsic delay, and the obstructive factors of the oscillation frequency limit produced by the antenna parameters are discussed. The equivalent circuit of the device is then shown. The relationship between the negative conductance and oscillation condition is also explained. In addition, I provide details about the total delay time and the approach to achieve a high oscillation frequency.

2.2 Device structure

The oscillator was fabricated by integrating an RTD with a slot antenna, as shown in Fig. 2.1. The slot forms a standing wave of an electromagnetic field as a resonator and also acts as an antenna by radiating output power at the same time [2.1]. Most of the output power radiates into the substrate because an InP substrate has a larger dielectric constant (~12) than air, and the effective wavelength in the substrate becomes shorter than that in air (the length becomes ~2.5) [2.2]. The RTD mesa and the upper electrode are connected to each other through an air-bridge structure to reduction the conduction loss of antenna and parasitic capacitance near mesa. A metal-insulator-metal (MIM) capacitance is fabricated using Au and SiO_2 on the side of the slot antenna. The MIM capacitance becomes short circuit at THz frequency range because MIM capacitance is ~3 pF in this thesis and slot structure is formed. The MIM structure is also used as a contact pad to check *I*-*V* characteristics without the InGaAs resistance to suppress parasitic oscillation. A sheet resistance with a heavily doped InGaAs layer is fabricated in parallel with the RTD to prevent low-frequency parasitic oscillation (several tens of GHz) in a parasitic circuit composed of such as bias line and power supply. This structure of InGaAs resistance is suitable for high-frequency direct modulation of the output power because of small inductance in the resistance which causes parasitic oscillation [2.3].

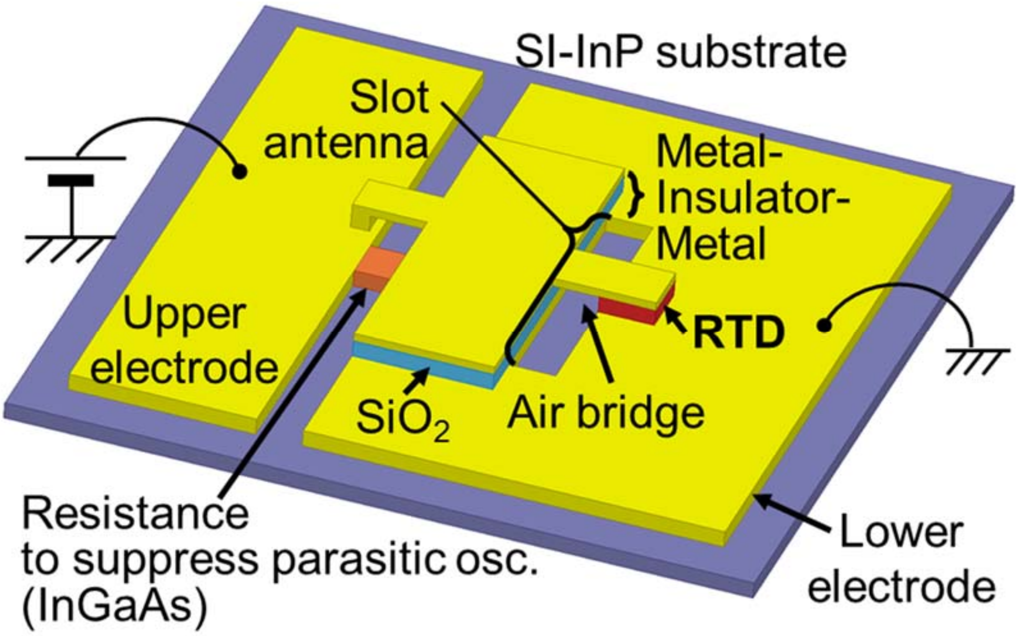

Fig. 2.1 Fabricated structure of RTD oscillator with slot antenna.

2.3 Fabrication process

The fabrication of the oscillator can be summarized as follows. The wafer is cleaned with DI water using ultrasonic cleaning, acetone boiling, and methyl alcohol. Next, two resist layers are applied using a spin coater. The bottom resist layer is

PMGI-SF6, and the top layer is ZEP-520A. These resists are tolerant to acid, which is used for surface cleaning before the contact metal deposition. The RTD mesa with an electrode on the top and a contact electrode is first formed by a sequence that includes electron-beam (EB) lithography, surface cleaning (O_2 ashing at 50 W and 50 sccm for 1 min and wet cleaning with $HCl:H_2O$ = 1:5 for 2 min at 0°), the deposition of Ti/Pd/Au = 20/20/200 nm, and wet chemical etching ($H_2SO_4:H_2O_2:H_2O$ = 1:1:40 at 0°) for mesa fabrication. The mask of the wet etching is the contact electrode. The lower electrode (LE) around the slot antenna was then fabricated by a sequence that included EB lithography, 2-layer resist coating, exposure and development, and the deposition of Ti/Pd/Au/Ti = 20/20/50/5 nm. The 5-nm Ti surface layer is used to improve the adhesion between the Ti and SiO_2. A 50-nm SiO_2 layer was deposited as the etching mask using plasma chemical vapor deposition (PVCD). Using reactive ion etching (RIE, $CH_4:H_2$ = 1:4), device isolation was obtained between the antenna electrodes and previously mentioned sheet resistance as part of the heavily doped InGaAs underlayer was formed. The air bridge and MIM capacitance were formed by the deposition of a 50-nm-thick SiO_2 layer using PVCD again for passivation, where the total thickness became ~100 nm; the formation of a contact hole on top of the RTD mesa by RIE (CF_4 and O_2) using a thick PMMA A8 resist mask to cover the edges of the large difference in the level of the device; EB lithography for the air bridge and MIM capacitance, with three resist layers of PMMA A8, PMGI SF9, and ZEP:Anisole = 2:1 from the bottom to top; and the deposition of Cr/Au = 10/1000–1500 nm to overcome the large difference in level. These process procedures are also shown in Figs. 2.2–5. The precise recipe of the fabrication process, including some techniques based on experience, is included in the appendix.

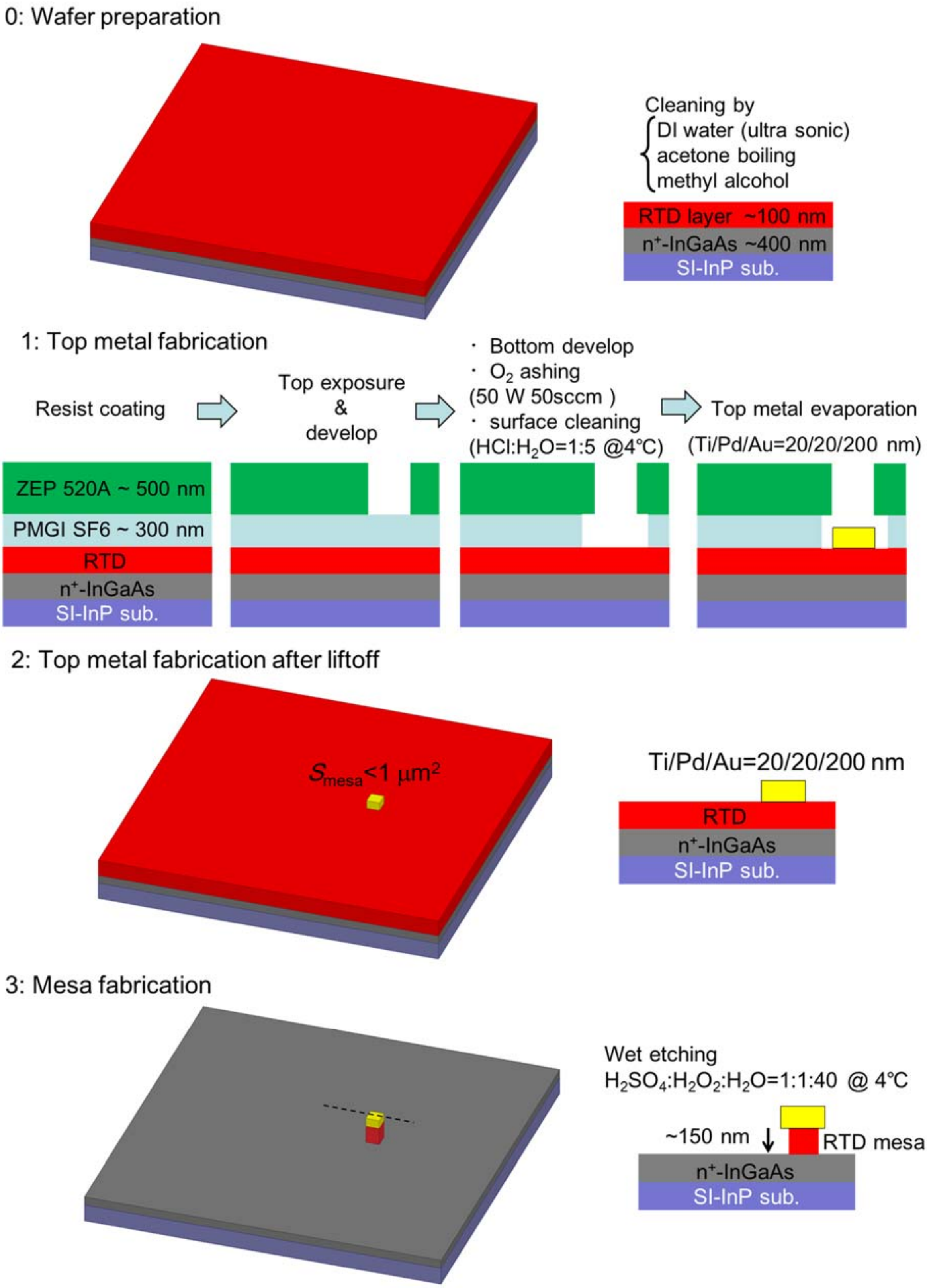

Fig. 2.2 Fabrication process 1.

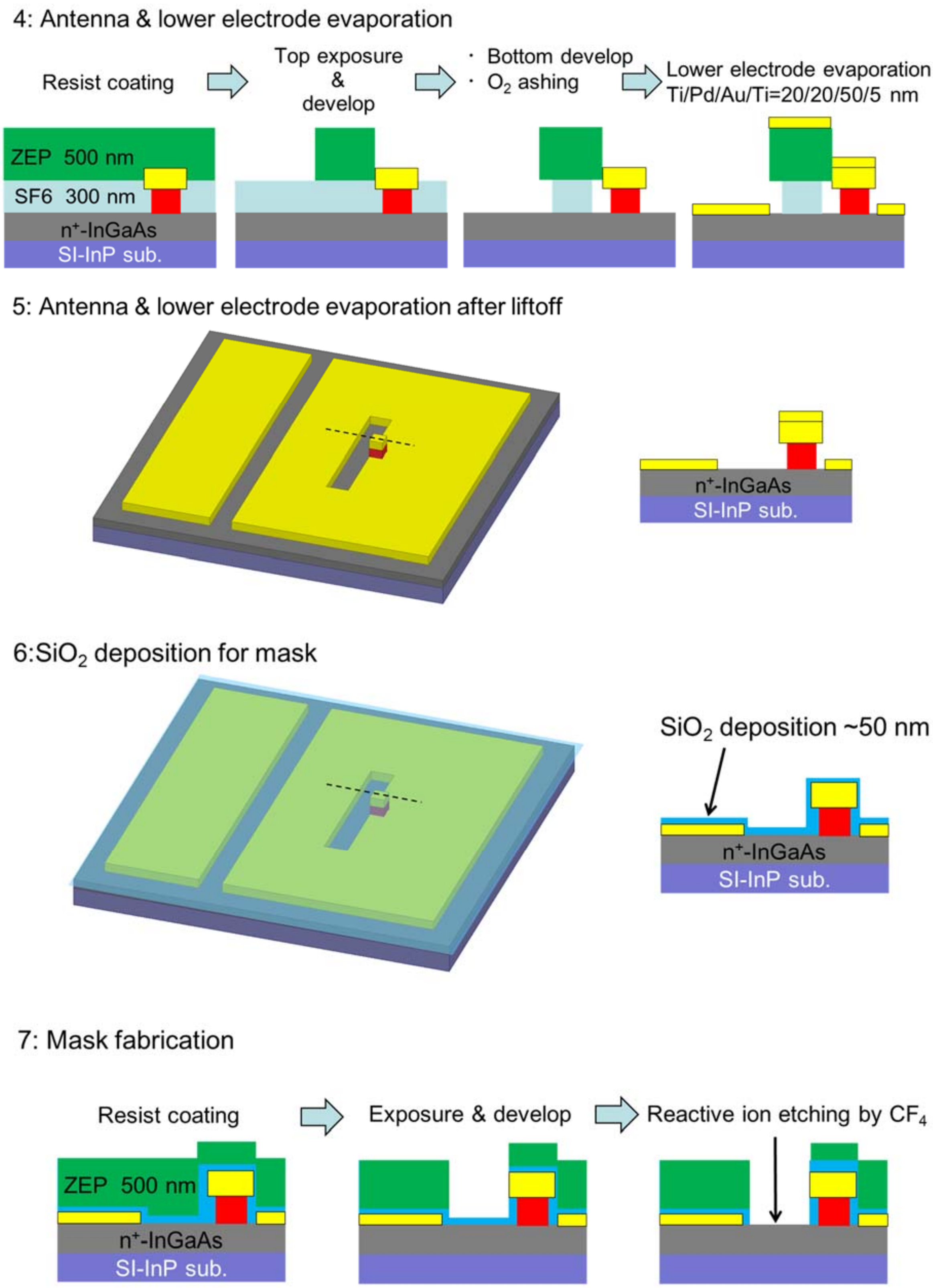

Fig. 2.3 Fabrication process 2.

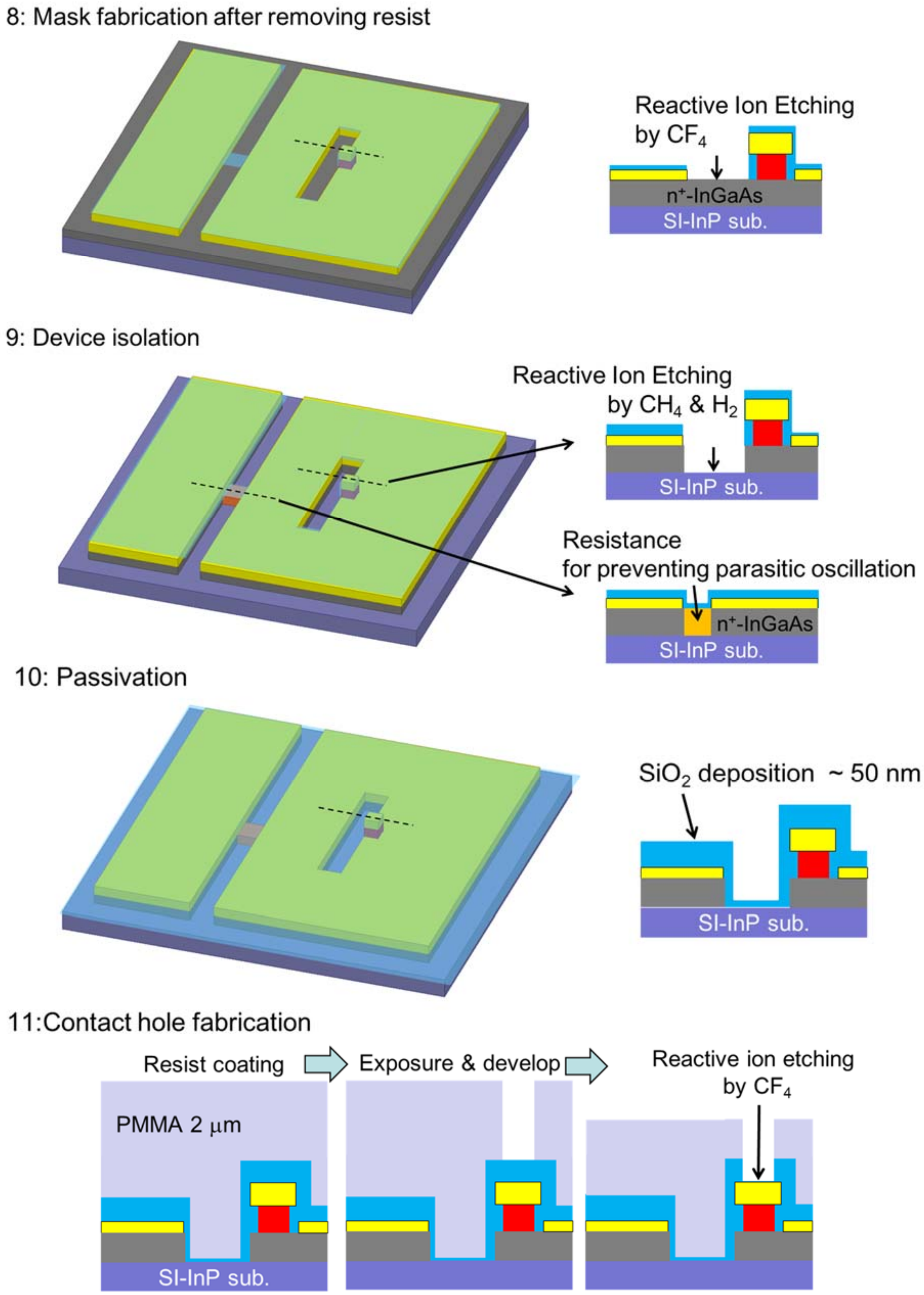

Fig. 2.4 Fabrication process 3.

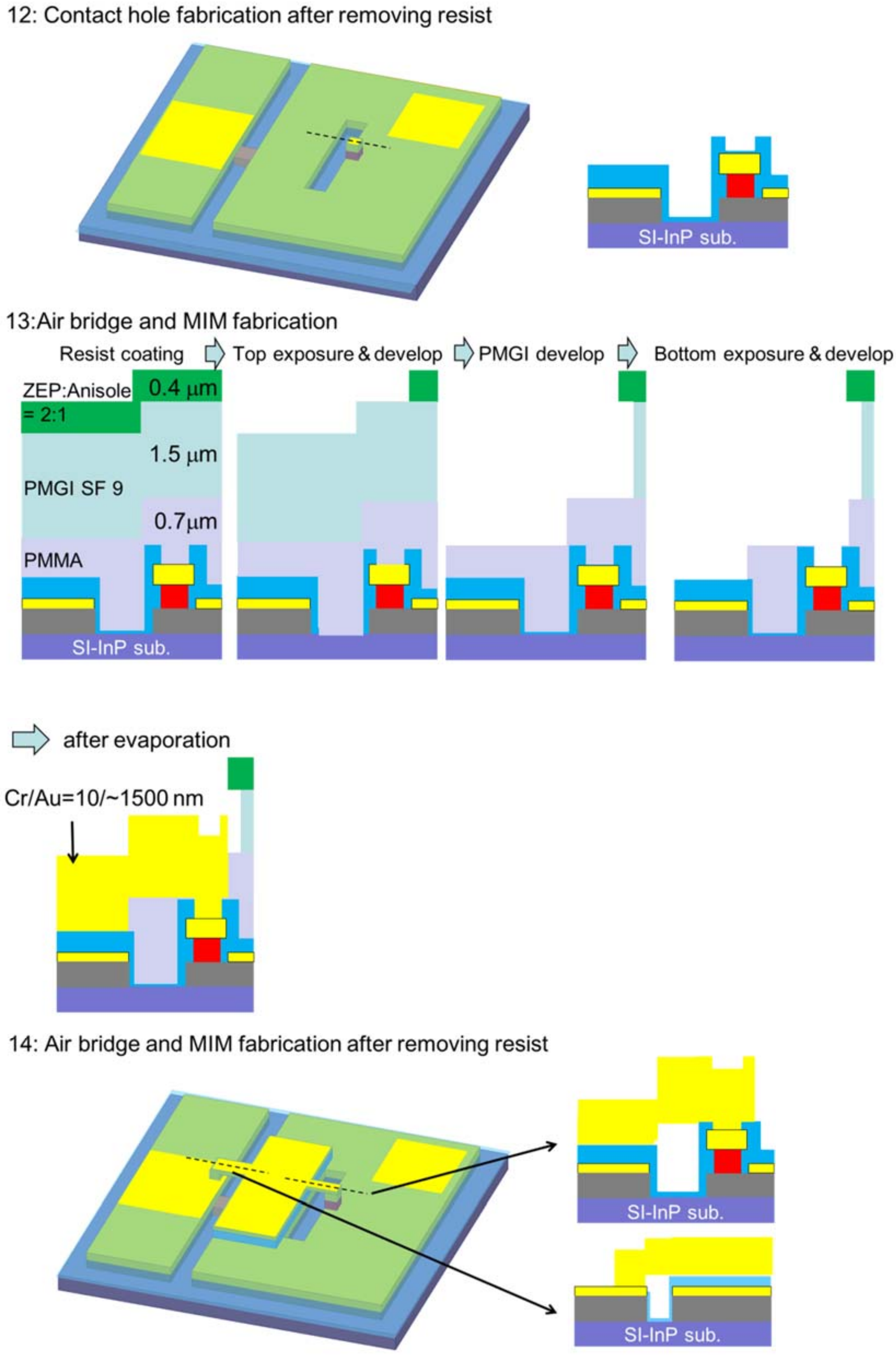

Fig. 2.5 Fabrication process 4.

2.4 Total delay time, antenna parameters, and oscillation frequency limit

2.4.1 RTD characteristics and equivalent circuit

The typical layer structure of the RTD is shown in Fig. 2.6. From the top layer to the substrate, the structure comprises a cap, n^+-$In_xGa_{1-x}As$ (5×10^{19} cm^{-3}, x= 0.8, 0.7, and 0.6 with 3 nm each); collector, n^+-$In_{0.53}Ga_{0.47}As$ (5×10^{19} cm^{-3}, 15 nm); collector spacer, $In_{0.53}Ga_{0.47}As$ (undoped: 6, 12, and 25 nm); barrier, AlAs (undoped, 1 nm); well, $In_{0.9}Ga_{0.1}As$ (undoped: 3 and 2.5 nm); barrier, AlAs (undoped, 1 nm); emitter spacer, InAlGaAs (undoped, 2 nm); emitter, n-InAlGaAs (3×10^{18} cm^{-3}, 20 nm), n^+-InAlGaAs (5×10^{19} cm^{-3}, 5 nm or 3-step 15 nm), n^+-$In_{0.53}Ga_{0.47}As$ (5×10^{19} cm^{-3}, 400 nm); buffer, $In_{0.53}Ga_{0.47}As$ (undoped).

These layers were grown on a semi-insulating InP substrate by molecular beam epitaxy. The wafers were fabricated by IQE. Fabrication of similar RTD layer by MOCVD was also accomplished by NTT group [2.4]. A cap layer with an indium-rich strained and graded composition and a high doping concentration was used to reduce the contact resistance of the electrode with decrease in the effective schottky barrier thickness. Indium-rich InGaAs was deposited on the well layer to reduce the bias voltage for NDC through the depression of the well bottom, which will be mentioned in Chapter 3. The bias voltage must be reduced to improve the device efficiency and also to prevent the generation of a high electric field in the collector spacer layer, which causes device breakdown. The breakdown voltages of $In_{0.53}Ga_{0.47}As$ is ~4×10^5 V/cm. A lattice-matched InAlGaAs emitter layer, which has a conduction-band edge closer to the resonance level in the well than that of $In_{0.53}Ga_{0.47}As$, was also used to reduce the bias voltage for NDC. Details of the emitter structure are described in also Chapter 3.

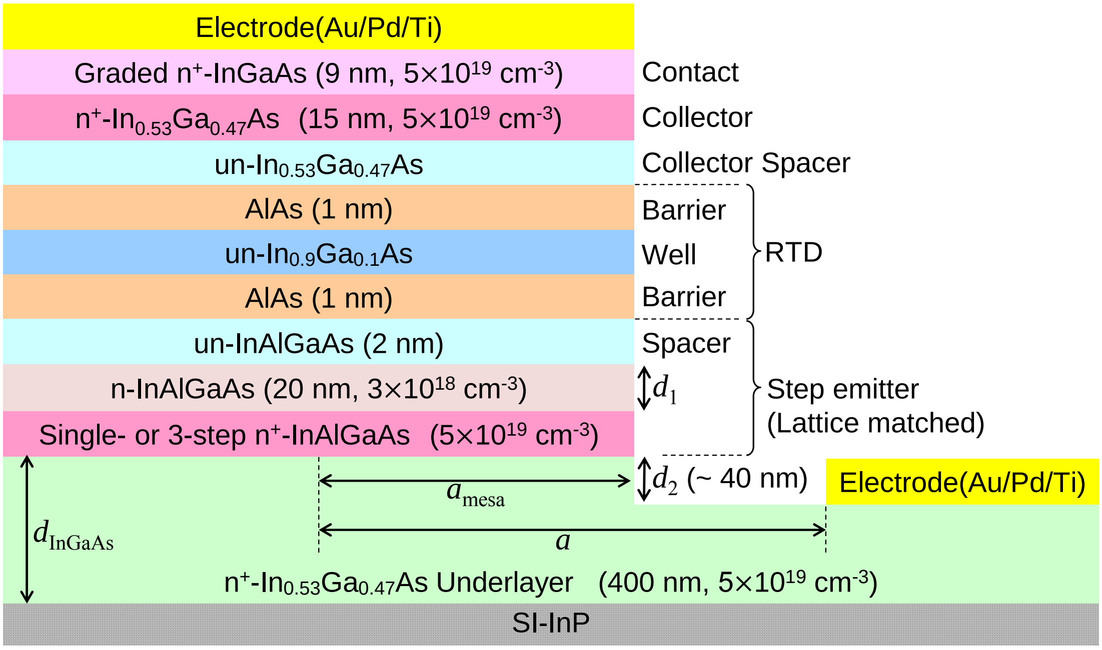

Fig. 2.6 Typical layer structure of RTD in this thesis. An InAlGaAs step emitter, details of which are described in Chapter 3, and an indium-rich deep quantum well were employed to reduce the bias voltage for NDC.

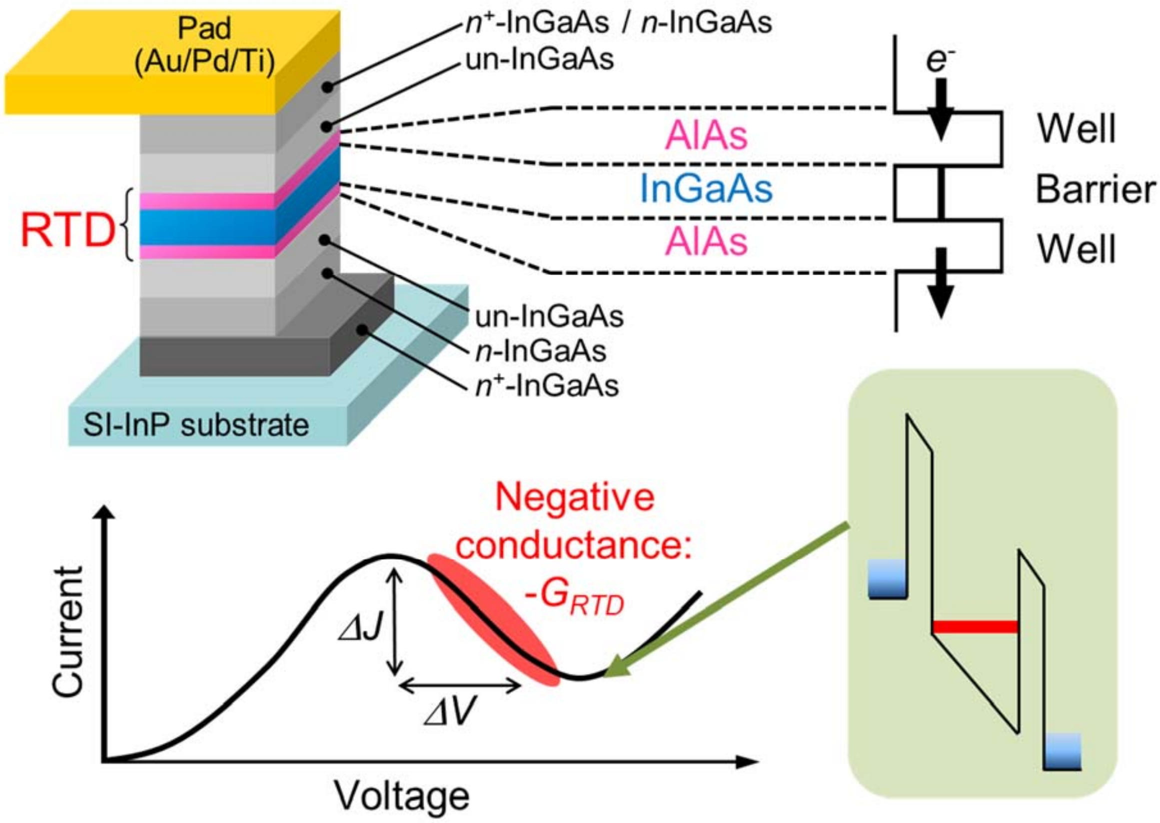

Fig. 2.7 Schematic diagram of *I-V* curve, energy band, and negative differential conductance region.

An RTD has a current peak and valley in its *I-V* characteristics caused by quantum well and negative differential conductance was occurred as shown in Fig 2.7. A schematic structure of the RTD mesa with the elements of the equivalent circuit is shown in Fig. 2.8 and an equivalent circuit of the oscillator including parasitic elements is also illustrated in Fig. 2.9, where $-G_{RTD}$ is the negative differential conductance (NDC) of an intrinsic RTD without parasitic elements, C_{RTD} is the capacitance of the RTD (details of which are described below) R_c and C_c are the contact resistance and capacitance, respectively, R_s is the series resistance composed of the bulk resistance of the RTD mesa and spread resistance, and Y_a is the admittance of the slot antenna calculated by using a three-dimensional electromagnetic simulator (ANSYS HFSS). The inductance of the RTD mesa is negligible because the length is very short (less than 200 nm).

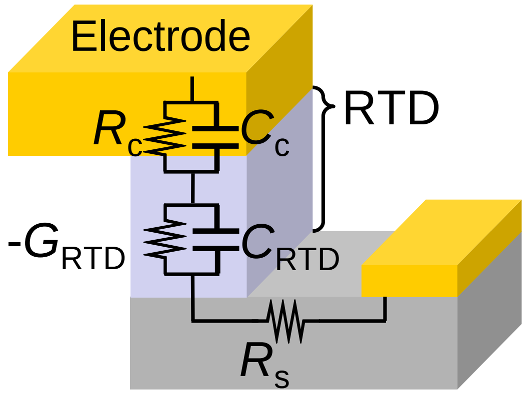

Fig. 2.8 Schematic structure of RTD mesa with equivalent circuit.

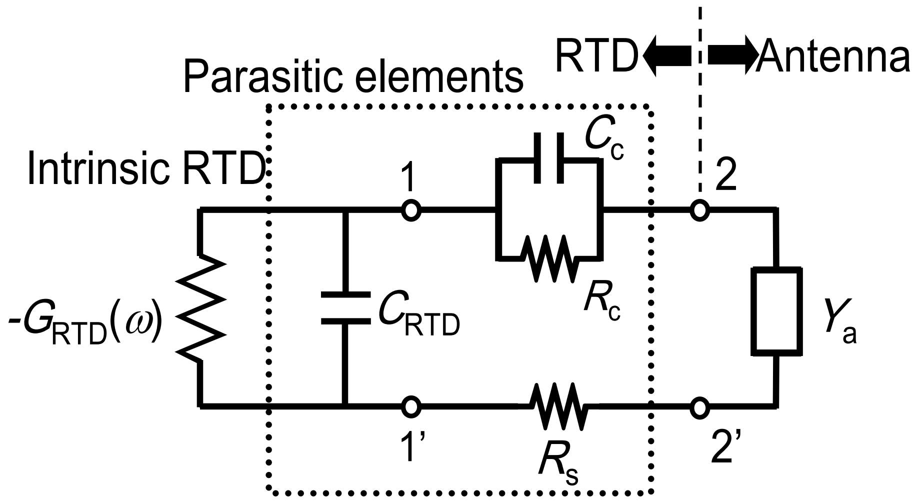

Fig. 2.9 Equivalent circuit of RTD oscillator with parasitic elements.

2.4.2 Slot antenna admittance and parameters

The antenna admittance was calculated using an HFSS model, as shown in Fig 2.10. A 50-Ω lumped port with a height of 200 nm and length of 1 μm was placed at the RTD mesa. The material parameters were set using the HFSS values listed in Table 2.1. The air surface was set to radiation. The “solve inside” option was applied to all of the materials, including metals. The air size was 440 × 400 × 100 μm, and the InP thickness was 20 μm to reduce the calculation time, which did not affect the calculation results. Other 3-D structure model sizes were set to the designed values of the oscillator. The solution frequency was set at 2 THz. The other settings were the default values of HFSS. The antenna circuit model is shown in Fig 2.11, where L_{ant} and C_{ant} are the antenna inductance and capacitance, respectively, and R_{cond} is the antenna resistance caused by the conduction loss, which is considered to be a skin effect and proportional to the square root of the oscillation frequency. G_{rad} was calculated using a lossless model whose materials of gold and SiO_2 were changed into the perfect conductor. These antenna parameters were obtained by fitting the simulation results for the admittances by HFSS and the equivalent circuit model in Fig 2.11.

Table 2.1 Material parameters in HFSS calculation.

Name	Air	Gold	Silver	InP	SiO_2	n^{++}-InGaAs	Perfect conductor
Relative permittivity	1.0006	1	1	12.1	4	11.6	1
Relative permeability	1.0000004	0.99996	0.99998	1	1	1	1
Bulk conductivity [S/m]	0	41000000	61000000	0	0	500000	1×10^{30}
Dielectric loss tangent				0			
Magnetic saturation [T]				0			
Lande G factor				2			
Delta H [A/m]				0			
Measured frequency [Hz]				9.4×10^{9}			
Mass density [kg/m^3]	1.1614	19300	10500	4800	2220	5500	0

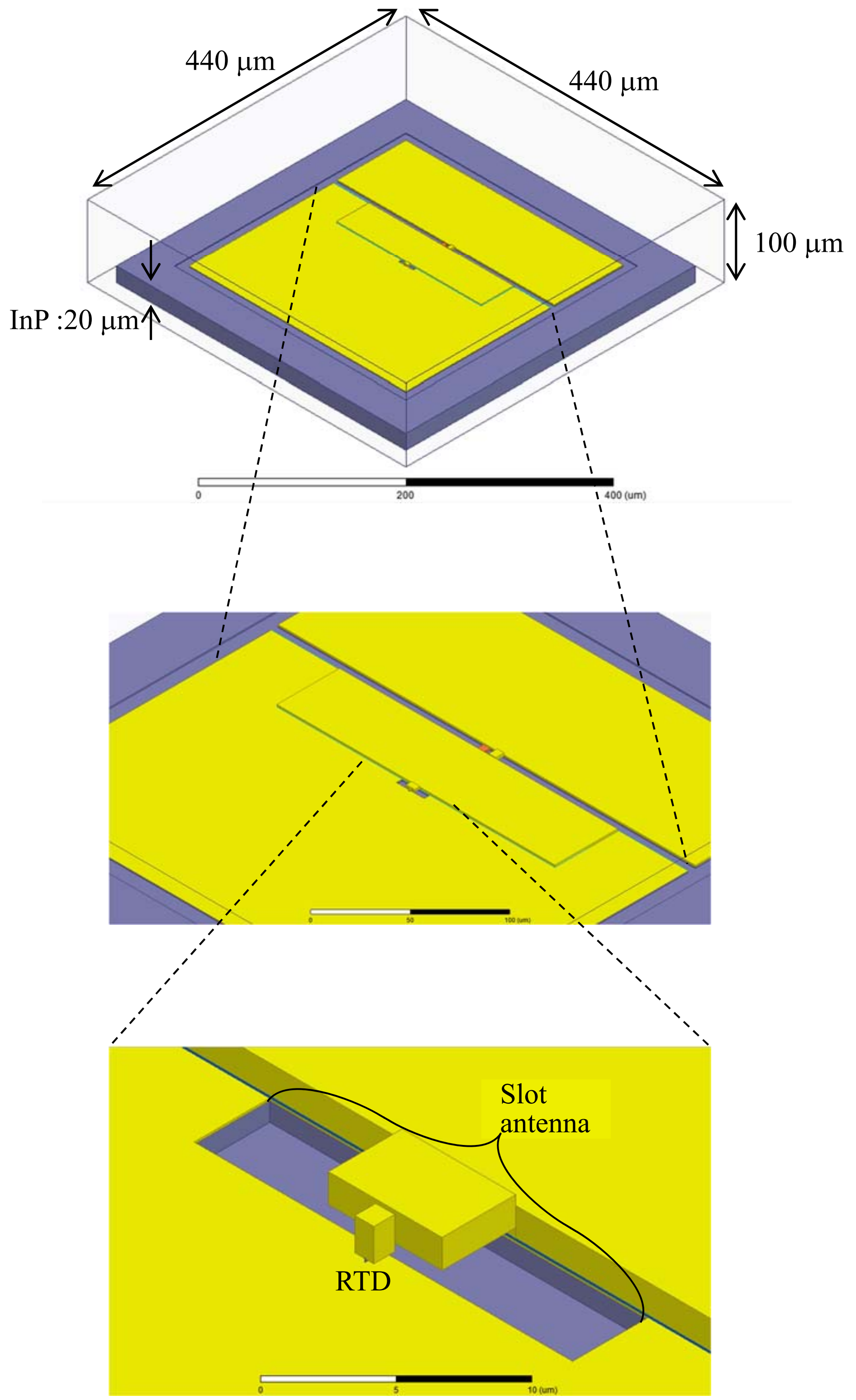

Fig. 2.10 Calculated antenna model of HFSS.

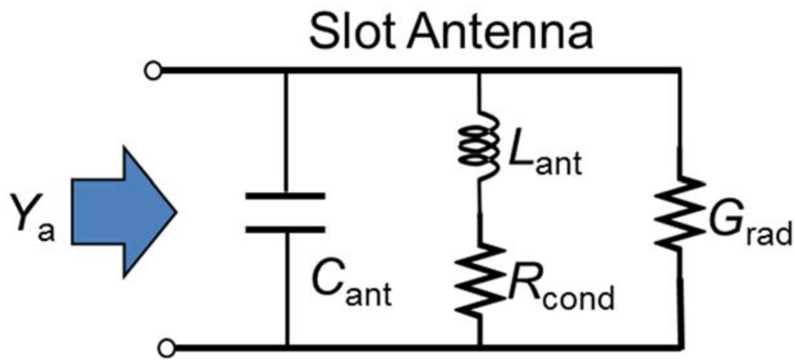

Fig. 2.11 Equivalent circuit of slot antenna.

2.4.3 Negative conductance and oscillation condition

The intrinsic NDC, $-G_{RTD}$, degrades with increasing frequency as [2.6,7]

$$-G_{RTD}(\omega) \cong -G_{RTD0}\cos\omega\tau_{int}\,, \qquad (1)$$

where G_{RTD0} is the absolute value of the NDC in the DC characteristics, approximately given by $(3/2)\Delta I/\Delta V$ for the widths of current and voltage (ΔI and ΔV, respectively) between a peak and a valley as shown in Fig 2.7, ω is the angular frequency, and τ_{int} is the intrinsic delay time mentioned above.

The oscillation condition is expressed as $G_{RTD}(\omega) \geq \mathrm{Re}(Y_a)$ if the parasitic elements are neglected. Antenna loss $\mathrm{Re}(Y_a)$ consists of the radiation conductance and the conductance due to the conduction loss in the antenna electrode and the leakage of radiation into the MIM capacitance. The oscillation frequency is given by the condition $\mathrm{Im}(Y_a) + \omega C_{RTD} = 0$. C_{RTD} is expressed as $\tau_{int}\,G_{RTD0} + C_{dep}$ [2.6,7], where the first term is the capacitance associated with the intrinsic delay and C_{dep} is the conventional parallel-plate capacitance from the emitter accumulation region to the collector depletion region in the RTD.

The output power is expressed as, if the parasitic elements are neglected, $P \cong (G_{rad}/2G_{RTD0})(G_{RTD0}\text{-}G_{rad}/\cos\omega\tau_{int})\Delta V^2$, where G_{rad} is the radiation conductance included in Re(Y_a). This equation implies that, if the radiation conductance is small, the oscillation easily takes place even for RTDs with small value of G_{RTD0} due to the factor in the brackets but the radiation power is small. The output power has the maximum at G_{rad} = (1/2) $G_{RTD}(\omega)$ if the antenna conduction loss is neglected and the maximum power is expressed as, $P_{max} \cong (3/16)\, \Delta I \Delta V \cos\, \omega\tau_{int}$. The ideal efficiency is calculated using P_{max} per the sum of power consumption at the center of NDC and at the InGaAs resistance for preventing parasitic oscillation.

2.4.4 Total delay time and oscillation frequency limit

τ_{int} is expressed in terms of the dwell time τ_{dwell} in the resonant tunneling region and the transit time τ_{dep} in the collector depletion region as [2.6,7]

$$\tau_{int} = \tau_{dwell} + \tau_{dep}/2. \tag{2}$$

For RTDs with a very short τ_{int}, the effect of the parasitic elements on the NDC is not negligible. The NDC of an RTD including the parasitic elements shown in Fig. 2.9 is equal to the real part of the admittance on the RTD side, which is given by

$$-[\mathrm{G}_{RTD}(\omega) - \omega^2 R_s C_{RTD}{}^2] \,/\, (1 + \omega^2 R_s{}^2 C_{RTD}{}^2)\ , \tag{3}$$

where R_c and C_c are neglected because the impedance of these elements is much smaller than R_s at the oscillation frequencies discussed later in this chapter.

Equation (3) is approximated using Eq. (1) as

$$-G_{RTD0}\, \cos\omega\tau_{all}, \tag{4}$$

where τ_{all} is the total delay time given by

$$\tau_{\mathrm{all}} = \sqrt{\tau_{\mathrm{int}}{}^2 + \tau_{\mathrm{ext}}{}^2}, \qquad (5)$$

with the intrinsic time τ_{int} given in Eq. (2) and the extrinsic delay time τ_{ext} approximately expressed as

$$\tau_{\mathrm{ext}} = (\pi/2)C_{\mathrm{RTD}}\sqrt{R_{\mathrm{s}}/G_{\mathrm{RTD0}}}\ . \qquad (6)$$

In the derivation of Eqs. (4)–(6), we assumed that $R_{\mathrm{s}}G_{\mathrm{RTD}}(\omega) << 1$ and used the reasonably good approximation of $\cos x \cong 1 - (2x/\pi)^2$ for $0 \leq x \leq \pi/2$.

The highest limit of the oscillation frequency f_{lmt}, above which the NDC cannot sufficiently compensate for the antenna losses, is approximately written from Eq. (4) as $G_{\mathrm{RTD0}}\cos(2\pi f_{\mathrm{lmt}}\tau_{\mathrm{all}}) = \mathrm{Re}(Y_{\mathrm{a}})$. Thus, in order to increase f_{lmt}, the reduction in the total delay time τ_{all} in Eq. (5) and reduction in $\mathrm{Re}(Y_{\mathrm{a}})$, which equals to reduction in antenna loss are necessary. For the intrinsic delay time in Eq. (2), τ_{dwell} can be reduced by a thin quantum well [2.7, 8] because τ_{dwell} is inversely proportional to the full width at half maximum (FWHM) of the energy spectrum of the tunneling transmission coefficient, which increases with decreasing well thickness. τ_{dwell} can also be reduced by thin barriers [2.9–10]. τ_{dep} in Eq. (2) can be reduced by thinning the collector spacer. However, an optimum spacer thickness exists because C_{dep} included in C_{RTD} increases simultaneously [2.11]. This situation is equivalent to simultaneous optimization of the intrinsic and extrinsic delay times. The extrinsic delay time can be reduced by a small C_{RTD} and R_{s}, as shown in Eq. (6).

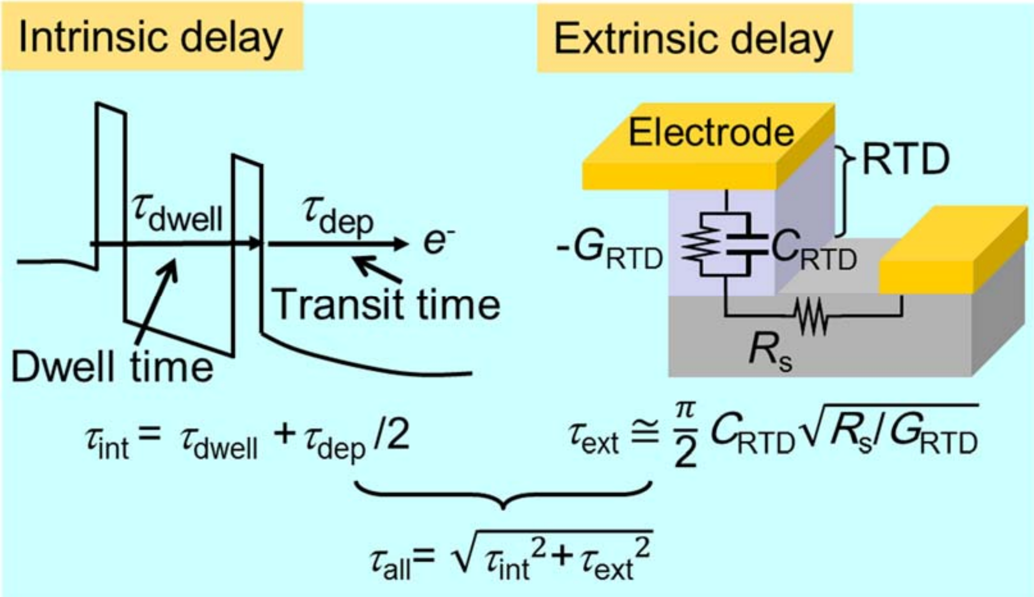

Fig. 2.12 Components of total, intrinsic, and extrinsic delay time.

2.4.5 Extraction of intrinsic delay time

The intrinsic delay time was extracted from the experimental results by the comparison with the results of theoretical analysis using the equivalent circuit in Fig. 2.9. In the theoretical analysis, the oscillation frequency and output power were calculated by the method described in Refs. 2.5, 6 using the parameter values mentioned below and the assumed values of τ_{int} and the capacitance C_{dep} per unit mesa area mentioned in this chapter. τ_{int} was then determined by fitting the highest limit of the oscillation frequency f_{lmt} and the mesa area at f_{lmt} in the theoretical calculation to those in the measured results. The thickness providing C_{dep} per unit mesa area could also be estimated from the potential profile including the accumulation and depletion layers. However, C_{dep} per unit mesa area was treated as a fitting parameter here because the oscillation frequency strongly depends on C_{dep} per unit mesa area. In this process, the effect of τ_{ext} is implicitly included as those of the parasitic elements, and only τ_{int} is extracted. The schematic diagram of the parameters fitting is shown in Fig 2.13.

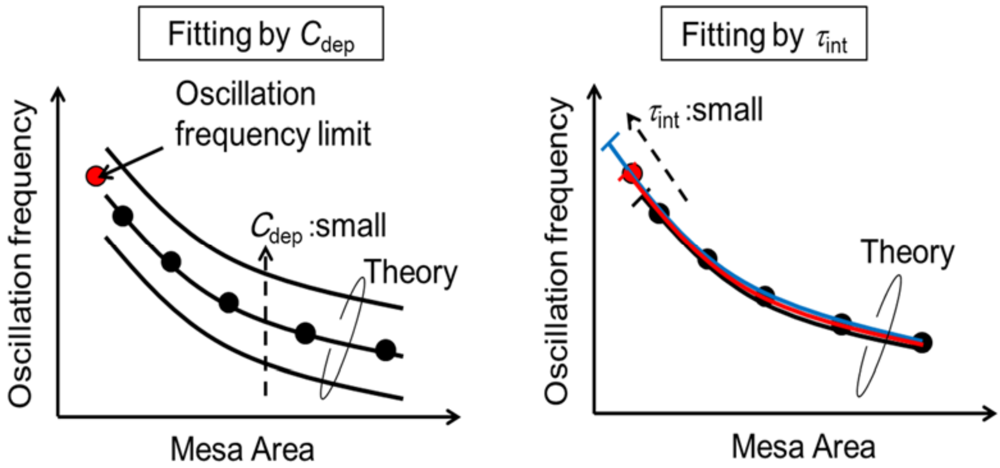

Fig. 2.13 Schematic diagram of procedure for fitting of C_{dep} and τ_{int}.

For the parameter values, $G_{RTD}(\omega)$ was estimated using the equations mentioned in this chapter. The admittance of the actual antenna structure was calculated using ANSYS HFSS. The series resistance R_s is the sum of the bulk and spread resistances. The bulk resistance was calculated as the sum of those for doped InGaAs and InAlGaAs layers in the RTD mesa. The spread resistance of the InGaAs underlayer was approximated as $1/(\pi\sigma d_{InGaAs})\ln(a/a_{mesa})$ [2.12], where σ is the conductivity, and d_{InGaAs}, a, and a_m are the lengths indicated in Fig. 2.6. This resistance was approximately calculated as that of a material with conductivity σ between two coaxial half-cylindrical electrodes with inner and outer radiuses a_{mesa} and a, respectively, and length d_{InGaAs}. d_{InGaAs} in the above formula must be replaced with the skin depth δ if $\delta < d_{InGaAs}$.

The frequency dependence of σ was included as $\sigma(\omega) = \sigma(0)/[1+(\omega\tau_{rel})^2]$, where

$\tau_{rel} = \mu m^* / e$ with μ, m^*, and e being the mobility, effective mass, and electron charge, respectively. The values of m^* and μ were estimated by extrapolation of the heavily doped data in Refs. 2.13 and 2.14. This conductivity is the real part of the complex conductivity $\sigma(\omega) = \sigma(0)/(1+j\omega\tau_{rel})$. The imaginary part of the complex conductivity works as an inductance, although this inductance is not taken into account in the present analysis. Owing to this inductance, the absolute value of the real part of the RTD admittance including parasitic elements, i.e., the absolute values of NDC with respect to the electrodes, appears slightly higher. The change in the imaginary part of the RTD admittance is much smaller than that of the real part. Exact treatment of the complex conductivity is a subject for future study. The skin effect was neglected because the mesa size and layer thicknesses are much smaller than the skin depth.

R_c was estimated from the measurement using the transmission line method (~15 $\Omega\mu m^2$), as shown in Fig 2.14, and C_c was calculated for the top metal-semiconductor contact, although the real part of the impedance due to these elements was much smaller than R_s, as shown in Fig 2.15. The Schottky height was estimated to be 0.17 eV with the typical contact resistance. The contact resistance between the InGaAs underlayer and the lower electrode in Fig. 2.6 was neglected because of the large area.

In real experimental results, unknown stray capacitance C_{ex} is observed. The oscillation frequency f_{osc} approximately given by $f_{osc} \approx 1/\sqrt{2\pi L_{ant}(C_{RTD}'S+C_{ant}+C_{ex})}$ for C_{RTD}' is the RTD capacitance per unit area and S is the RTD mesa area. C_{ex} is estimated by the dependence $1/f_{osc}^2$ as a function of mesa area and the stray capacitance which is obtained experimentally is considered in this extraction of intrinsic delay time. The reason of the stray capacitance is not clear at present. Exact treatment of this stray capacitance is a subject for future study.

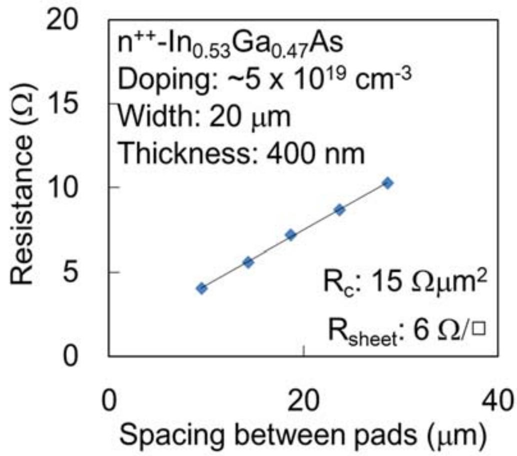

Fig. 2.14 Typical experimental result of contact resistance measured with transmission line method.

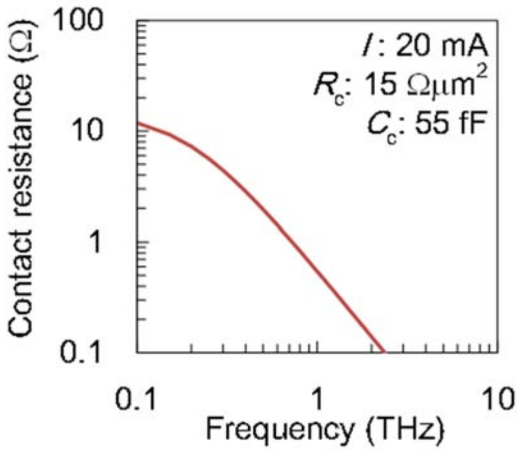

Fig. 2.15 Decrease in contact resistance caused by contact capacitance of RTD.

2.4.6 Toward higher frequency

It is important to reduce the intrinsic and extrinsic delays, along with the antenna length and conduction loss, to increase the oscillation frequency limit. The intrinsic delay consists of the dwell time through the barrier and well and the transit time across the collector depletion layer. The extrinsic delay consists of such as the capacitance and series resistance of RTD. Optimizing the antenna length and reducing the antenna conduction loss are important to further increase the oscillation frequency limit. The results of a theoretical analysis are shown in Fig 2.16. The assumed values for the antenna and RTD are also shown. Reducing the total delay time increases the oscillation frequency limit. Although reducing the antenna length decreases the antenna inductance, it simultaneously increases the antenna loss. Thus, an optimum antenna length exists. After optimizing the antenna length, a reduction in the antenna conduction loss is needed.

To obtain an oscillation frequency greater than 2 THz, it is necessary to reduce the total delay to 70 fs and the antenna loss to less than 8 mS using a 9-μm antenna as shown in Fig 2.16. The next chapters discuss reductions in the dwell, transit, and extrinsic times, as well as antenna structure improvements.

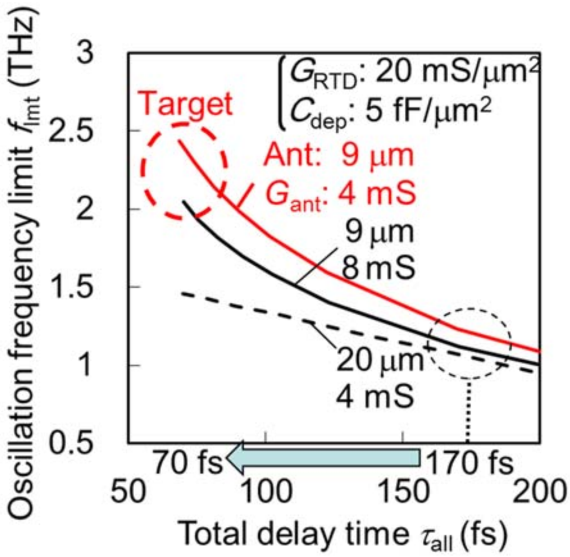

Fig. 2.16 Reduction in total delay time and reduction in antenna length and loss for higher oscillation frequency limit.

2.5 Conclusion

In this chapter, I explained the theoretical analysis of an RTD terahertz oscillator and the methods for achieving a high frequency. Reductions in the total delay time and antenna length and loss are important. The dwell time will be reduced using a thin barrier and well, and the transit time will be reduced by optimizing the spacer thickness. Improvements in the antenna length and conduction loss are also important. In the next chapters, the reductions in these factors will be discussed.

Chapter 3
High-frequency oscillation with reduced dwell time

3.1 Introduction

This chapter discusses methods to reduce the dwell time by improving the RTD layer structure. It first discusses the qualitative mechanism for reducing the dwell time by reducing the barrier and well thicknesses and decreasing the bias voltage with a deep well and step emitter structure. Next, the experimental results of reducing the barrier and well thicknesses and using a deep well and step emitter are discussed. A decrease in the dwell time and increase in the oscillation frequency limit were experimentally achieved using the optimum barrier thickness, reducing the well thickness, and suppressing the bias voltage with an appropriate InGaAs well depth and InAlGaAs step-emitter height.

3.2 Reductions in dwell time and bias voltage

3.2.1 Calculation of tunneling transmission coefficient with thin barrier and well

At a reduced well thickness, a high value is expected for the current-density width ΔJ in the NDC region [3.1]. This is because the resonance levels moves up, and the full width at half-maximum (FWHM) of the tunneling transmission coefficient increases. Simultaneously, a thin well reduces the valley current generated by the leakage through the second resonance level, because the energy separation between the first and second resonance levels also increases in the thin-well structure. Thus, a large ΔV is also expected with a thin-well structure. The wide FWHM is effective for reducing the dwell time, because the dwell time is inversely proportional to the FWHM. The dwell time also decreases with thinner barriers as a result of the increase in the tunneling transmission coefficient, as shown in Fig. 3.1.

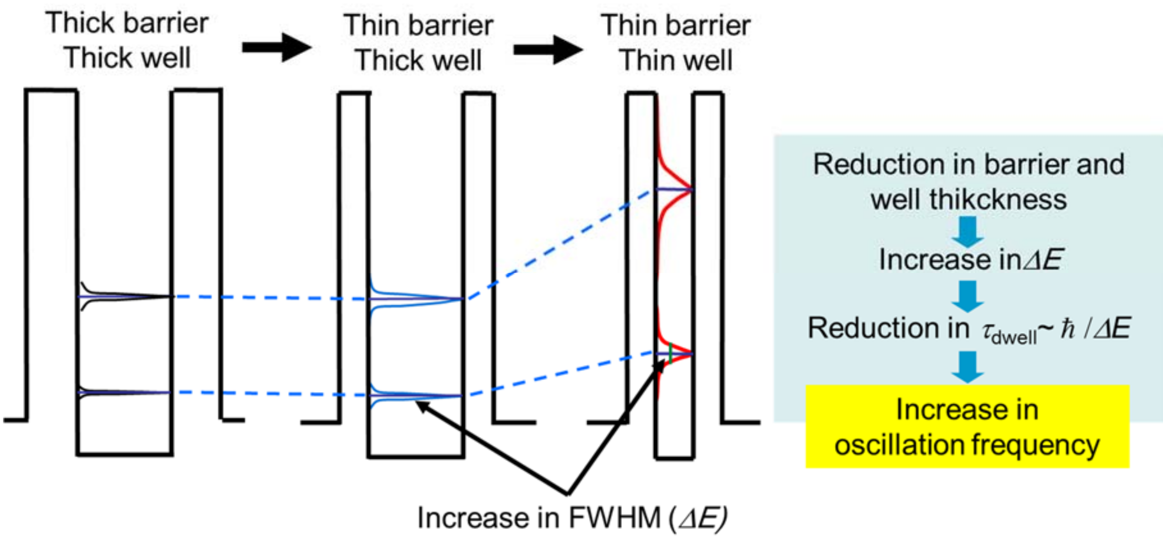

Fig. 3.1 Reduction in dwell time with increase in FWHM associated by thin barrier and well.

Although decreasing the barrier thickness was effective for increasing the current density [3.2–5], the simultaneous increase in the leak current causes a decrease in the width of the peak and valley current. Thus, an optimum thickness (~1 nm) was found in previous experiments of our study group [3.6].

The tunneling transmission coefficient is calculated using the transfer matrix. A model of the band gap is shown in Fig. 3.2. The parameters are as follows: E_b is the barrier height, E_e is the emitter height, E_d is the well depth, V_b is the bias voltage, and α is the electric field in the RTD. ΔE_1 to ΔE_4 are the band heights, and E is the incident energy. The effective mass of the barrier is fixed at 0.15. I performed calculations for well widths between 5 and 1 nm (in 1-nm steps). The barrier thickness, height, and effective mass of d_{B1} and d_{B2} are 1 nm, 0.8 eV, and 0.14, respectively. The well depth and effective mass are 0.26 eV and 0.027, respectively, with $In_{0.9}Ga_{0.1}As$. An increase in the effective mass with the energy caused by the non-parabolicity of the quantum well is assumed [3.7,8], as shown in Fig. 3.3. The bias voltage is considered using an asymmetric rectangular potential. This calculation is very simple, but it is sufficient to obtain the tendency of the increase in ΔE. Based on the estimation, a decrease in the well thickness causes an increase in the tunneling transmission coefficient. However, making the well too thin causes a reduction in the peak-to-valley ratio, and the negative conductance region will decrease with leakage above the barrier and through the 2^{nd} resonance level.

The calculation results for the well-thickness dependence are shown in Fig. 3.4 The tunneling transmission coefficient of FWHM increases with a decrease in the well thickness because of the increase in the resonance level. Making the well too thin causes increased leakage by the 2^{nd} resonance. Thus, an optimum well thickness exists.

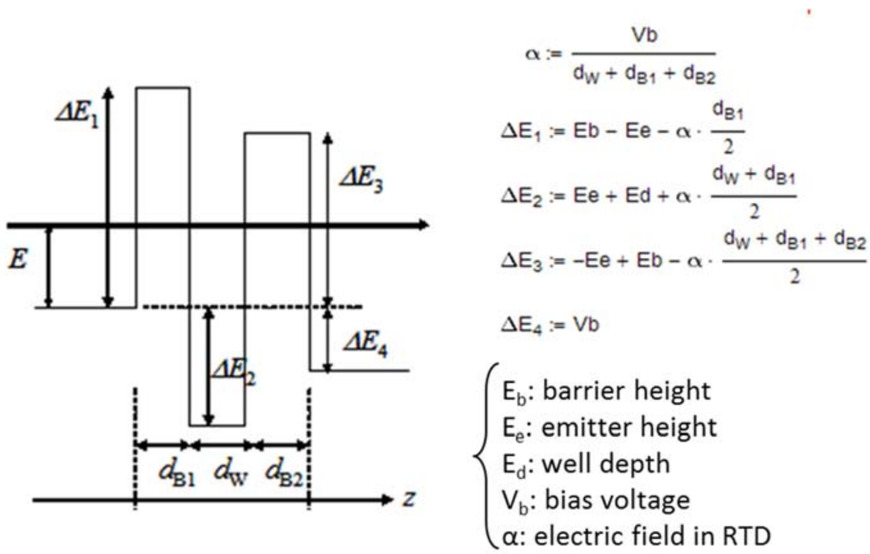

Fig. 3.2 Calculation model of band diagram for tunneling transmission coefficient and the parameters of the rectangular potential of RTD.

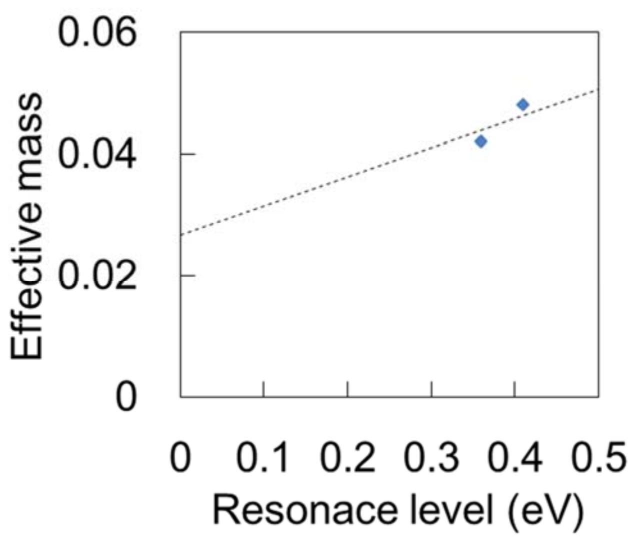

Fig. 3.3 Increase in effective mass with resonance level from bottom of the well.

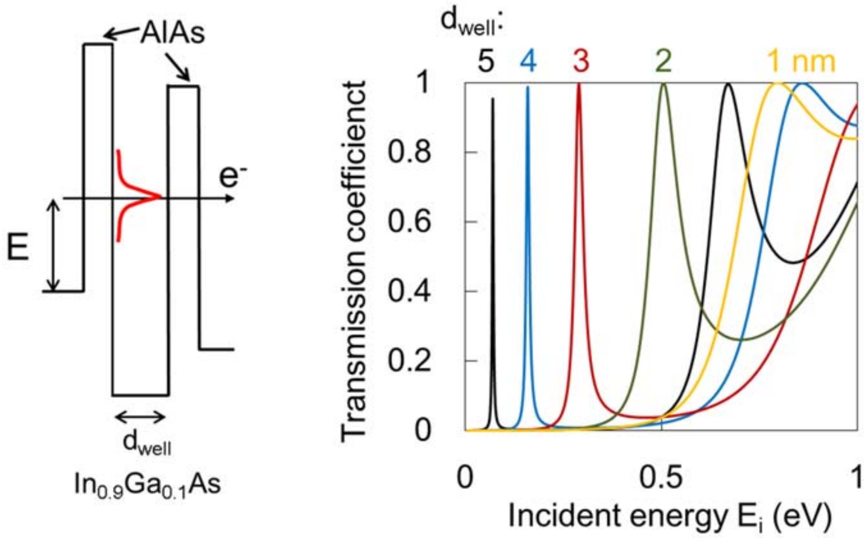

Fig. 3.4 Estimation of tunneling coefficient with rectangular potential of RTD.

3.2.2 Increasing well depth to decrease bias voltage

Increasing the well depth is an effective way to reduce the bias voltage. The well depth is determined by the indium composition rate of the InGaAs well. Fig. 3.5 shows the calculation results for the transmission coefficient with two different well depths: 0.2 eV ($In_{0.8}Ga_{0.2}As$) and 0.26 eV ($In_{0.9}Ga_{0.1}As$). The well and barrier thicknesses are 3 nm and 1 nm, respectively. Increasing the well depth decreases the peak of the transmission coefficient by almost the same value as the increase in the well depth. Thus, the bias voltage will be reduced.

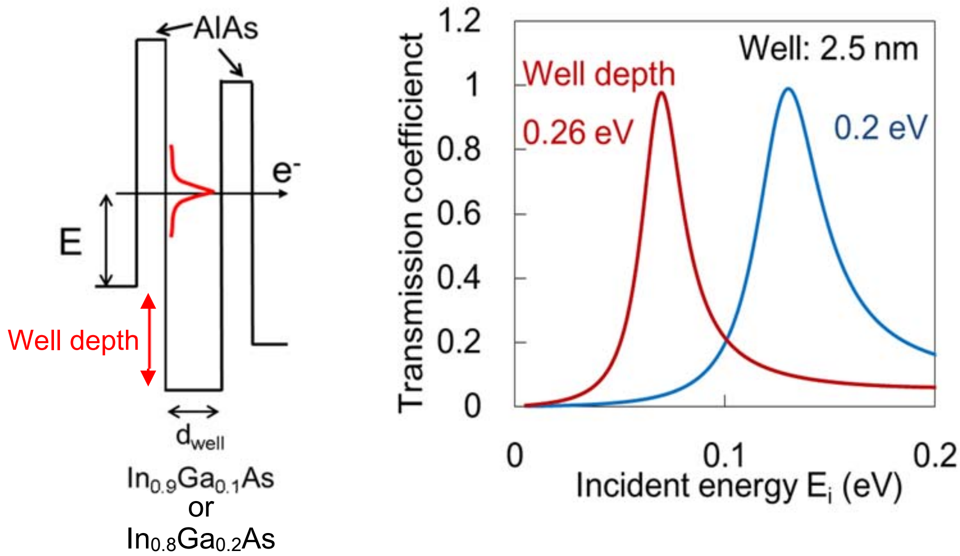

Fig. 3.5 Tunneling coefficient rates with two different well depth.

3.2.3 Step emitter to decrease bias voltage

Increasing the well thickness causes an increase in the bias voltage. A graded emitter that changed the indium composition of the emitter was applied in a previous study [3.6]. However, it caused a lattice mismatch and limited the epitaxy. To prevent this mismatch, InAlGaAs was applied to the emitter layer as shown in Fig. 3.6. The increase in the Al composition was balanced by a decrease in the Ga composition. The increase in the Al composition caused an increase in the energy gap, which decreased the resonance level difference between the well and emitter conduction band. This caused a reduction in the bias voltage. Reduction in bias voltage is also effective for increase in the efficiency. The value of the Al composition was decided based on the previous experimental results on the tendency of the bias voltage to increase with a decrease in the well thickness.

Estimations of the tunneling coefficient with decreases in the well thickness and increases in the emitter height are shown in Fig. 3.7. In these calculations, the emitter height and bias voltage were assumed to maintain the same peak (0.07 eV) and electric field in the RTD (0.01 V/nm). The FWHM of the transmission coefficient increased with a decrease in the well thickness and adjustment of the step emitter height. From about a 2-nm-thick well, the resonance shape collapsed with an increase in the transmission coefficient rate caused by the 2nd resonance level in the well.

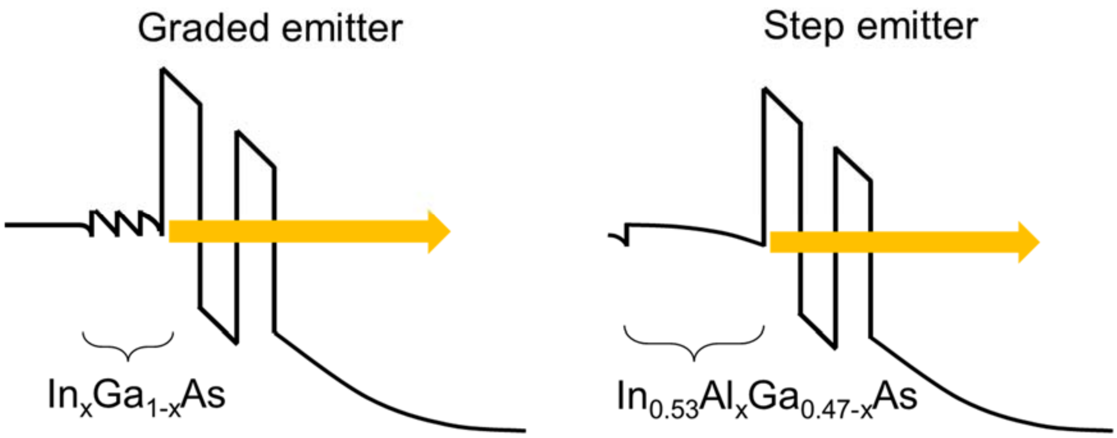

Fig. 3.6 Schematic band diagram of graded emitter and step emitter.

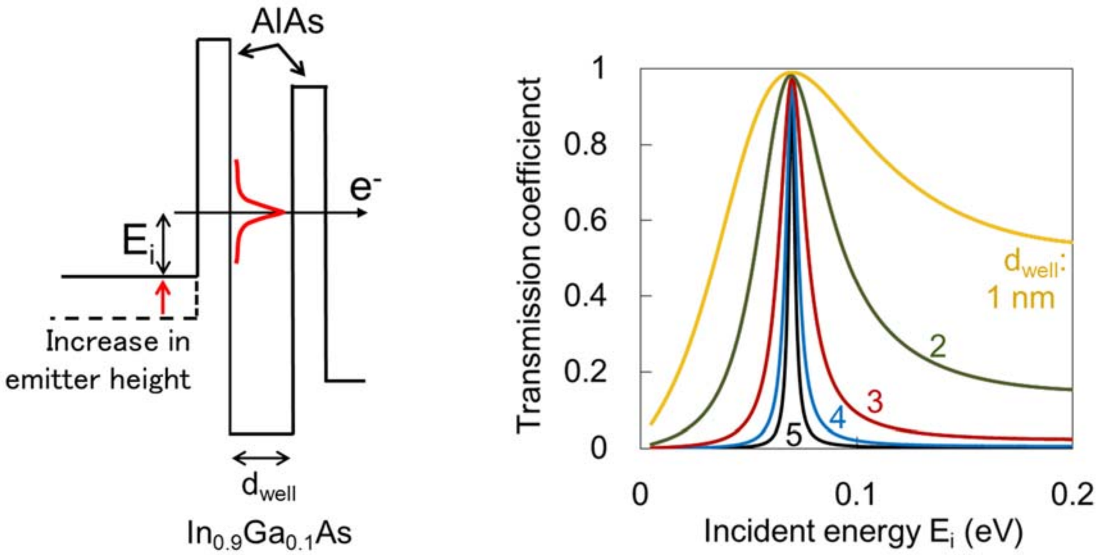

Fig. 3.7 Estimation of tunneling coefficient with reduction in well thickness and increase in emitter height.

3.3 Experimental results and discussions

3.3.1 Reduction in barrier thickness

Reducing the barrier thickness was an effective way to reduce the dwell time, because of the increase in the FWHM of transmission coefficient rate. The barrier dependence was investigated in Refs. 3.4–6, and the optimum barrier thickness was experimentally found to be about 1 nm, as shown in Fig. 3.8. In Fig. 3.9, E_1 and E_2 are the 1st and 2nd resonance levels, respectively. I_p, V_p, I_v, and V_v are the peak current, peak voltage, valley current, and valley voltage, respectively. A barrier that was too thin caused an increase in valley current I_v because of the increase in the transmission coefficient of the 2nd level resonance in the RTD, as shown in Fig. 3.9. Thus, I used a 1-nm barrier thickness for all the RTDs in this investigation.

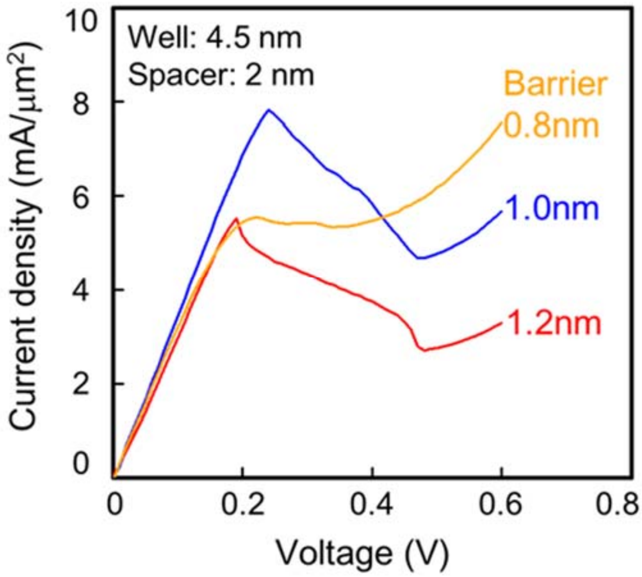

Fig. 3.8 I-V characteristics for the RTDs with different barrier thickness from Ref. 3.6.

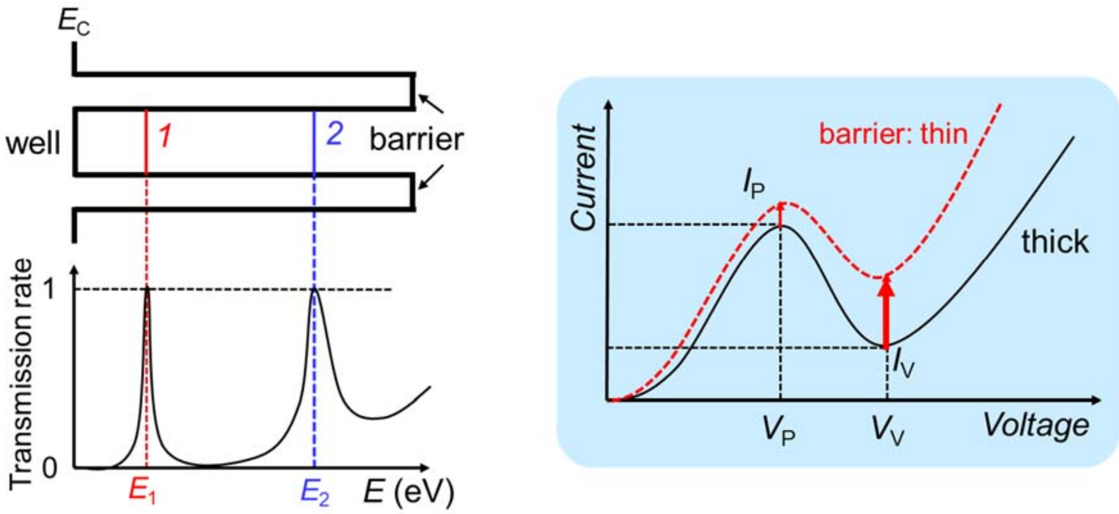

Fig. 3.9 Schematic diagram of increase in valley current because of increase in transmission rate of 2nd level resonance from Ref. 3.6.

Figs 3.10 and 3.11 compare the previous RTD results with those for a well thickness of 4 nm and barrier thicknesses of 1.2 and 1 nm, respectively. The thickness was observed with a transmission electron microscope. The oscillation frequency increased with decreasing mesa area as a result of the decrease in the capacitance of RTD. The oscillation frequency with a barrier thickness of 1 nm was higher than that with 1.2 nm at the same mesa area, because as previously mentioned, the additional capacitance $\tau_{\mathrm{int}}G_{\mathrm{RTD}}$ decreased with a decrease in the intrinsic delay τ_{int}. The oscillation frequency increased from 1.04 THz to 1.31 THz with a decrease in the barrier thickness. The intrinsic delay time was fitted using these results. A decrease in the barrier thickness causes a decrease in the intrinsic delay from 170 to 120 fs. The output power was several tens of microwatts. To further increase the oscillation frequency, the delay time was decreased without decreasing the barrier thickness in the next sections, because a further decrease in the barrier thickness was ineffective.

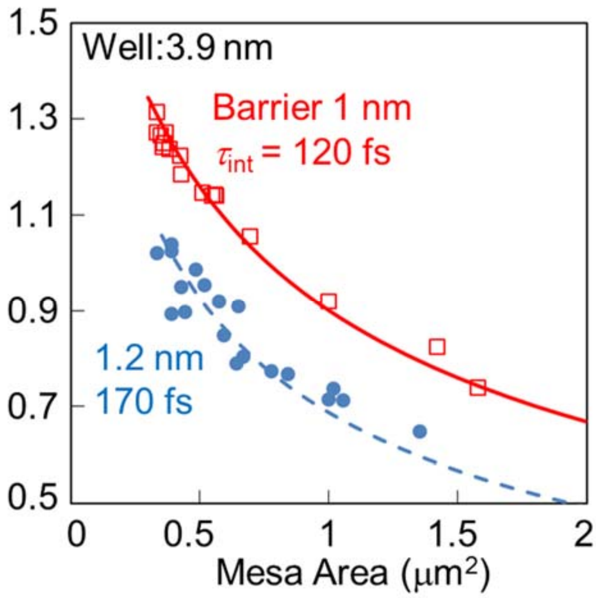

Fig. 3.10 Oscillation frequency vs mesa area with two different barrier thicknesses. The intrinsic delay of the RTD with 1.2-thick barrier is recalculated with resent discussion of increase in series resistance with frequency mentioned in chapter 2.

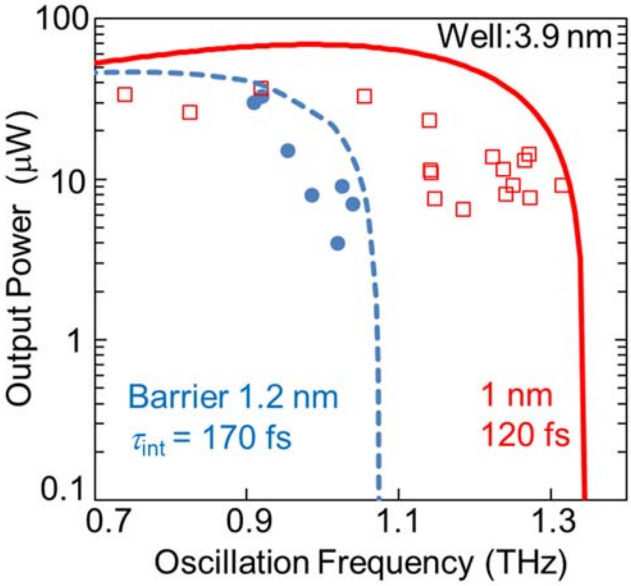

Fig. 3.11 Output power vs oscillation frequency of two RTDs with 1.2- and 1-nm barrier with 20-μm antenna.

3.3.2 Reduction in well thickness

Fig. 3.12 shows the dependences of the fundamental oscillation frequency on the mesa area of the RTD with well thicknesses of 4.5 and 3.9 nm. The oscillation frequency increased with decreasing mesa area as a result of the decrease in capacitance. The oscillation frequency of the 3.9-nm RTD was higher than that of the 4.5-nm RTD with the same mesa area, because as previously mentioned, the additional capacitance $\tau_{int}G_{RTD}$ decreased with a decrease in the intrinsic delay τ_{int}.

The absolute value of G_{RTD} decreased with an increase in the oscillation frequency as a result of the intrinsic delay and decrease in the mesa area. This effect results in the existence of the smallest limit for the mesa area, below which the oscillation cannot be obtained because of the insufficient G_{RTD} to compensate for the radiation loss. I obtained fundamental oscillations at 770 GHz and 1.31 THz for RTDs with well thicknesses of 4.5 nm and 3.9 nm near the smallest limit for the mesa area, respectively. The limit for the mesa area of the RTD with the 3.9-nm well was smaller than that of the RTD with the 4.5-nm well, because G_{RTD} remained high at a high frequency as a result of the short dwell time. The oscillation spectrum at the highest frequency of 1.31 THz is shown in the inset of Fig. 3.12. The output power was around 10 μW, and the mesa area was 0.33 μm^2.

I estimated the intrinsic delay time τ_{int} by fitting the theoretical calculation to the experimental results. The details of the estimation method were already described. The fitting curves are shown in Fig. 3.12. The estimated values of τ_{int} were 230 and 120 fs for the RTDs with the 4.5-nm and 3.9-nm wells, respectively. The delay time was significantly reduced by decreasing the well thickness.

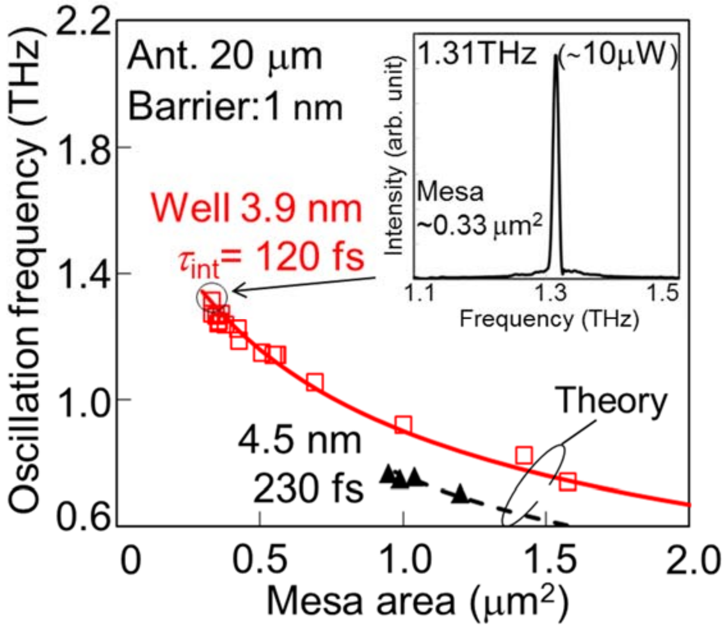

Fig. 3.12 Dependence of oscillation frequency on RTD mesa area of 4.5- and 3.9-nm-thick wells and measured spectrum of fundamental oscillation of 1.31 THz. The intrinsic delay of the RTD with 4.5nm-thick well is recalculated with resent discussion of increase in series resistance with frequency mentioned in chapter 2.

3.3.3 Deep and thin well structure

A reduction in the electron dwell time was expected with a thin quantum well as a result of the increase in the width of the tunneling transmission coefficient, because the dwell time is inversely proportional to this width. However, a high bias voltage was required because of the increase in the resonance level. Depressing the bottom of the quantum well using indium-rich InGaAs is an effective way to decrease the bias voltage.

I prepared two RTDs with different quantum well layers, 3.5-nm-thick $In_{0.8}Ga_{0.2}As$ and 3-nm-thick $In_{0.9}Ga_{0.1}As$ (thin and deep wells), as shown in Fig. 3.13.

The former indium composition was the same as that in the RTD of Ref. 3.4. The collector spacer thickness was 2 nm and the step emitter structure was not applied.

I also tried InAs wells with thicknesses of 3 and 2.5 nm, but I could not observe the NDC. By checking the RTD well layer using a scanning electron microscope, it seemed that the layer could not made because of the large difference in the lattice constants between AlAs and InAs.

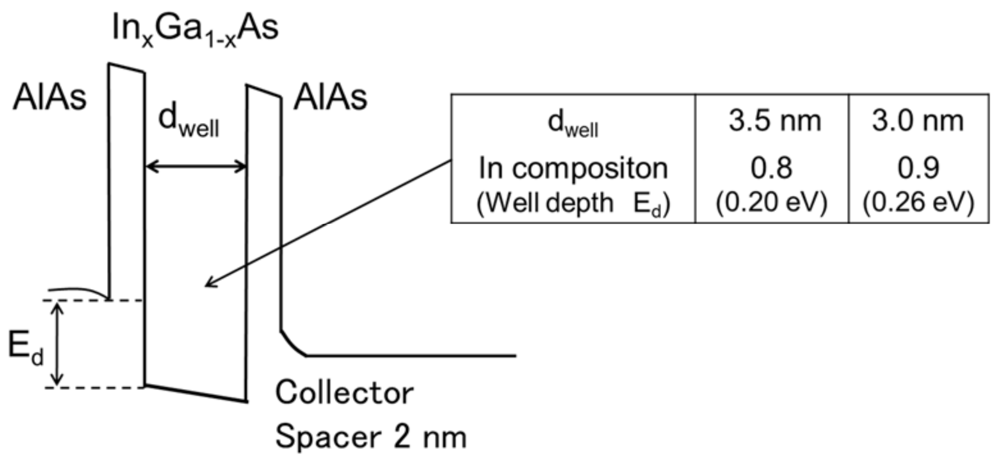

Fig. 3.13 Schematic band diagram of with and without thin and deep well.

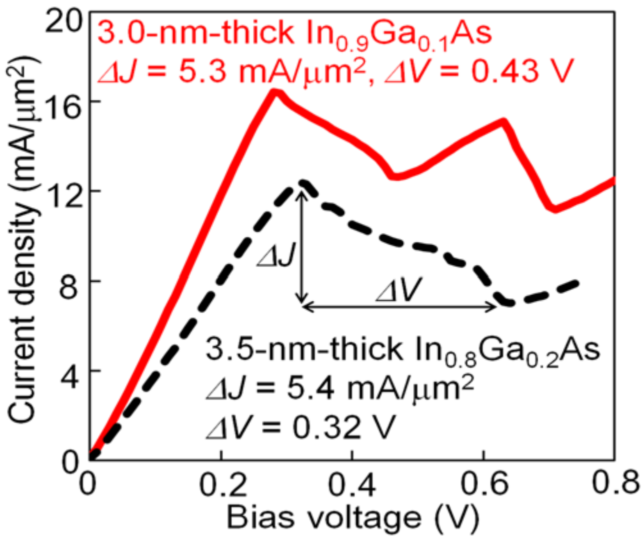

Fig. 3.14 *I*–*V* characteristics for the RTDs with and without deep quantum well.

Fig. 3.14 shows the *I*–*V* characteristics for the two RTDs mentioned above. The voltage at the current peak without the deep and thin well was 0.31 V, whereas a similar but slightly reduced peak voltage of 0.28 V was obtained for the deep and thin well despite the decreased well thickness. We also obtained ΔJ (the density of ΔI) and ΔV values of 5.4 mA/μm^2 and 0.32 V for the RTD without the deep and thin well, and 5.3 mA/μm^2 and 0.43 V for that with the deep and thin well, respectively.

I fabricated the RTD oscillators with an integrated 20-μm-long slot antenna. Fig. 3.15 shows the dependences of the fundamental oscillation frequency on the mesa area for RTDs with and without a deep and thin well. For both RTDs, the oscillation frequency increased with decreasing mesa area as a result of the decrease in the capacitance. I obtained fundamental oscillations of up to 1.27 and 0.96 THz with and without the deep and thin well, respectively. The highest oscillation frequency in this experiment was 1.27 THz with a mesa area of 0.25 μm^2. The output power of the device oscillating at

1.27 THz was ~1 μW.

Because the absolute value of G_{RTD} decreased with an increase in the oscillation frequency as a result of the intrinsic delay and decrease in the mesa area, there was a limit to the mesa area, below which the oscillation could not be obtained because there was insufficient G_{RTD} to compensate for the radiation loss. This limit of the mesa area was smaller for a thinner well, because G_{RTD} was less degraded as a result of the shorter dwell time. Because of this condition, a higher frequency oscillation was obtained in the deep and thin well in Fig. 3.15, as mentioned above. The oscillation frequency at the same area was also higher for the deep and thin well, because the additional capacitance generated by the intrinsic delay time, including the dwell time, was smaller.

I estimated the intrinsic delay time by fitting the theoretical calculation to the experimental results. The fitting curves are also shown in Fig. 3.15. The estimated intrinsic delay times τ_{int} were 40 and 110 fs for the RTDs with and without the deep and thin well, respectively. A further increase in the oscillation frequency will be expected with an optimized structure in terms of the thickness and material of the well and spacer layer.

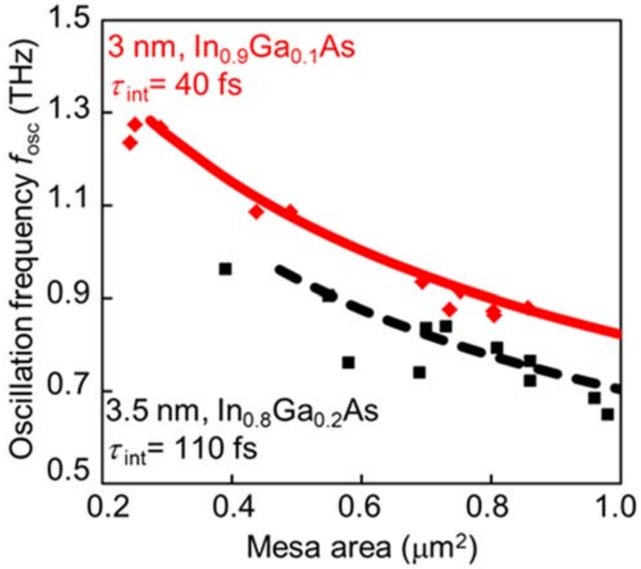

Fig. 3.15 Dependence of oscillation frequency on RTD mesa area of 3-nm-thick $In_{0.9}Ga_{0.1}As$ and 3.5-nm-thick $In_{0.8}Ga_{0.2}As$.

3.3.4 Step emitter structure

A step emitter was employed to reduce the bias voltage for NDC in this section. From the top side, the structure was composed of undoped $In_{0.53}Al_{0.1}Ga_{0.37}As$ (2 nm)/n-$In_{0.53}Al_{0.1}Ga_{0.37}As$ (20 nm)/n^{+}-$In_{0.53}Al_{0.1}Ga_{0.37}As$ (5 nm), which step height is 100 meV and $In_{0.53}Al_{0.08}Ga_{0.372}As$ (2 nm)/n-$In_{0.53}Al_{0.08}Ga_{0.372}As$ (20 nm)/n^{+}-$In_{0.53}Al_{0.08}Ga_{0.372}As$ (5 nm), which step height is 80 meV for the RTDs, with 1-nm barrier, 3-nm well, and 25-nm spacer as shown in Fig. 3.16. Fig. 3.17 shows *I-V* characteristics and the peak voltage decreases with increase in the step emitter height. The dependence of oscillation frequency on the mesa area is shown in Fig. 18. The experiment was the first time oscillation of InAlGaAs step emitter structure.

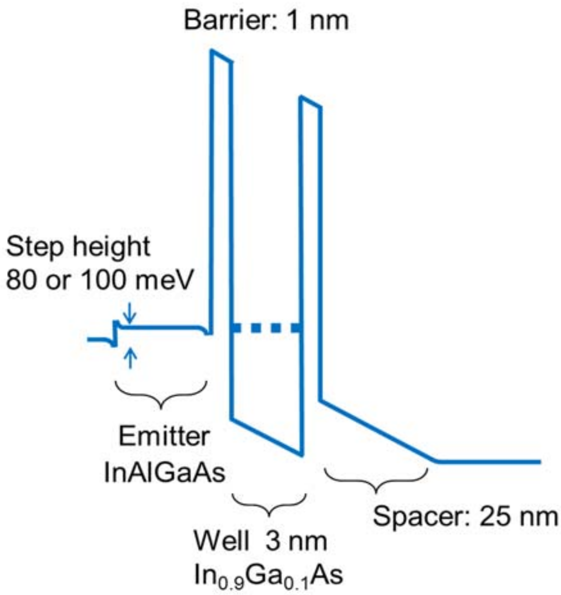

Fig. 3.16 Schematic band diagram of step emitter structure.

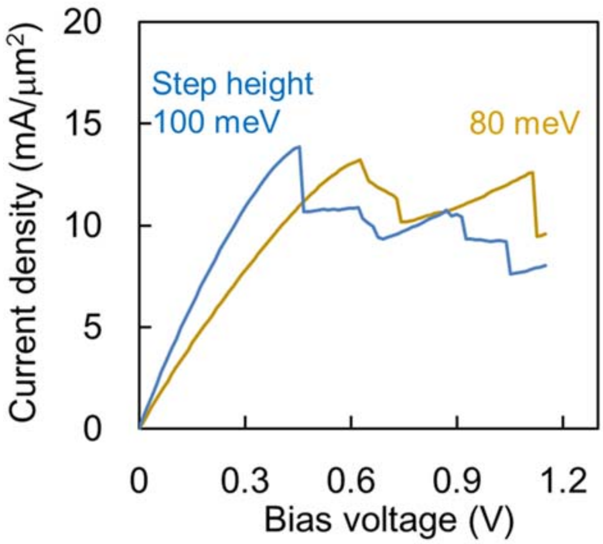

Fig. 3.17 Experimental results of *I*-*V* characteristics for two step emitter height.

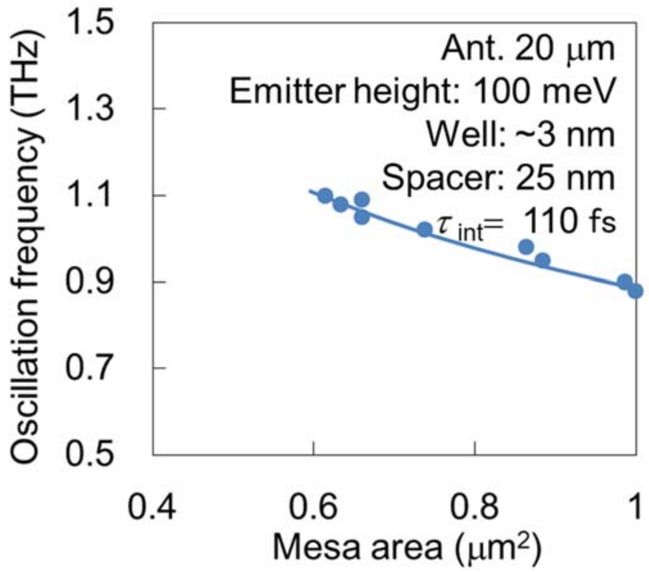

Fig. 3.18 Oscillation frequency versus mesa area for the RTD with 100-meV step emitter.

3.3.5 Reduction in well thickness with step emitter

In order to reduce τ_{dwell} and the bias voltage for NDC, I employed step emitter structure and thin well simultaneously. The emitter structure is as follows. From the top side, the structure was composed of undoped $In_{0.53}Al_{0.1}Ga_{0.37}As$ (2 nm)/n-$In_{0.53}Al_{0.1}Ga_{0.37}As$ (20 nm)/n^+-$In_{0.53}Al_{0.1}Ga_{0.37}As$ (5 nm) for the RTD with the 3-nm well and undoped $In_{0.53}Al_{0.15}Ga_{0.32}As$ (2 nm)/ n-$In_{0.53}Al_{0.15}Ga_{0.32}As$ (20 nm)/3-step n^+-$In_{0.53}Al_xGa_{0.47-x}As$ (x = 0.15, 0.1, and 0.05, 5 nm each) for the RTD with the 2.5-nm-thick well, as shown in Figs. 3.19-20. The InAlGaAs composition was designed to obtain nearly the same bias voltage for NDC in the samples with different well thicknesses. The three-step structure was introduced to avoid a large step at the conduction-band edge between the InAlGaAs emitter and the InGaAs underlayer. Two

RTDs with 3- and 2.5-nm-thick wells, along with a 1-nm barrier and 6-nm spacer, were prepared for this experiment. The current density-voltage characteristics of these RTDs are shown in Fig. 3.21 for different quantum-well thicknesses. The current-density and voltage widths of NDC (ΔJ and ΔV, respectively) are also extracted and shown in Fig 3.22. I obtained ΔJ (the density of ΔI) and ΔV values of 18 mA/μm^2 and 0.4 V for the RTD with the 2.5-nm-thick well, and 11 mA/μm^2 and 0.24 V for the RTD with the 3-nm-thick well, respectively.

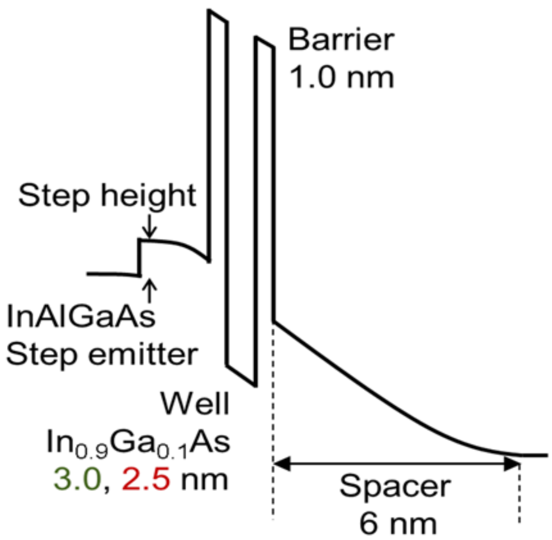

Fig. 3.19 Schematic band diagram of RTDs with different quantum-well thickness.

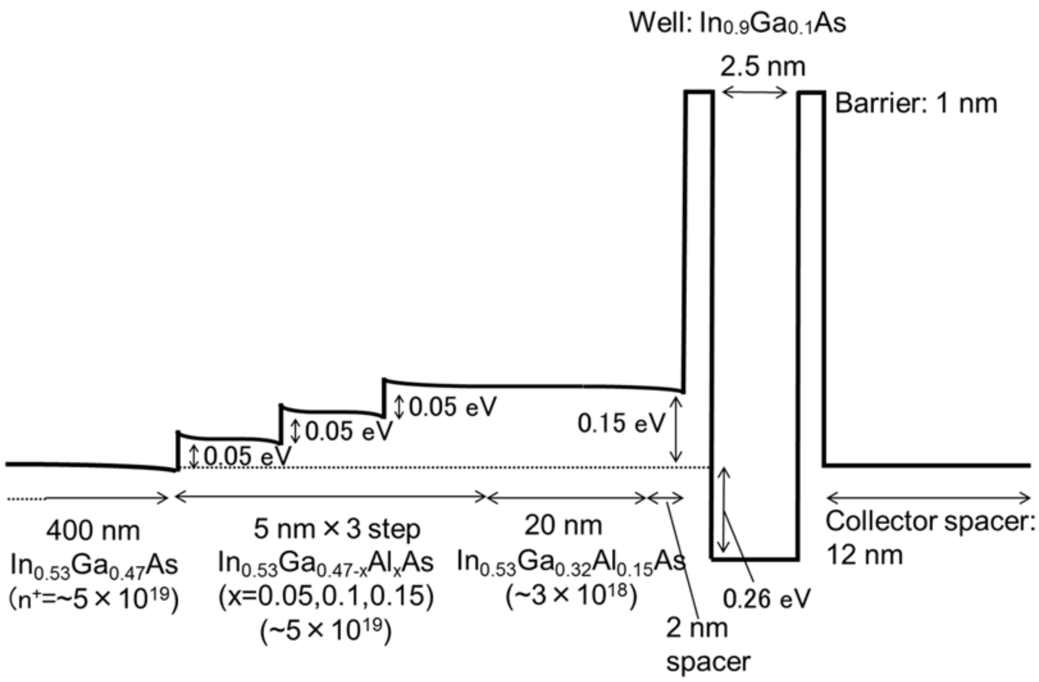

Fig. 3.20 Band diagram of RTD with the well thickness of 2.5-nm well and 3-step emitter structure.

Because the full width at half-maximum of the tunneling transmission coefficient was increased, ΔJ was larger for the thinner quantum well. Simultaneously, the thin well resulted in a reduction in the valley current generated by the leakage through the second resonance level, because the energy separation between the first and second resonance levels also increased. Because of this effect, ΔV also increased with decreasing well thickness, as seen in Figs. 3.21-22. As seen in Fig. 3.21, the bias voltage at the current peak is almost the same because of the effect of the InAlGaAs emitter layer, as previously mentioned.

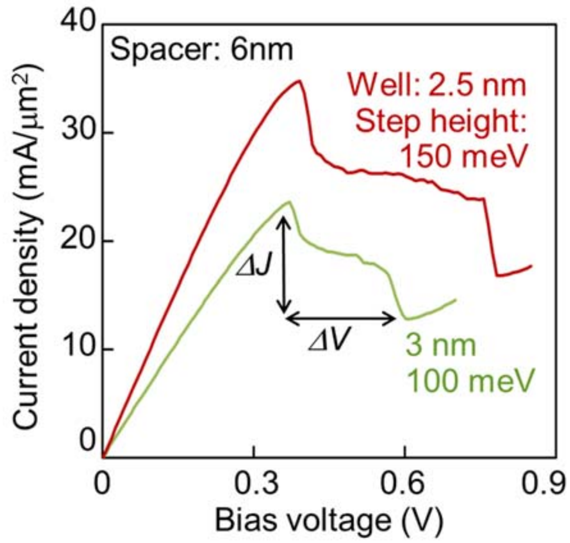

Fig. 3.21 Measured current density-voltage characteristics of RTDs with different quantum-well thicknesses.

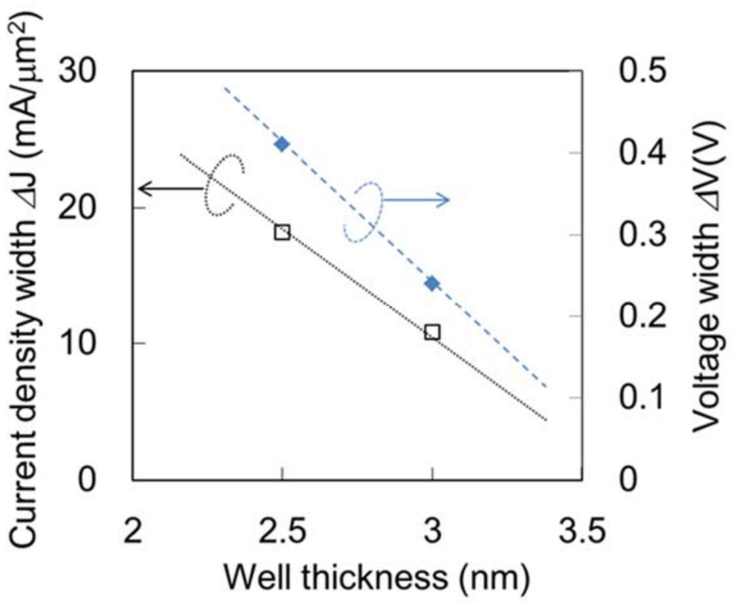

Fig. 3.22 Measured current density and voltage widths as a function of well thicknesses of RTD.

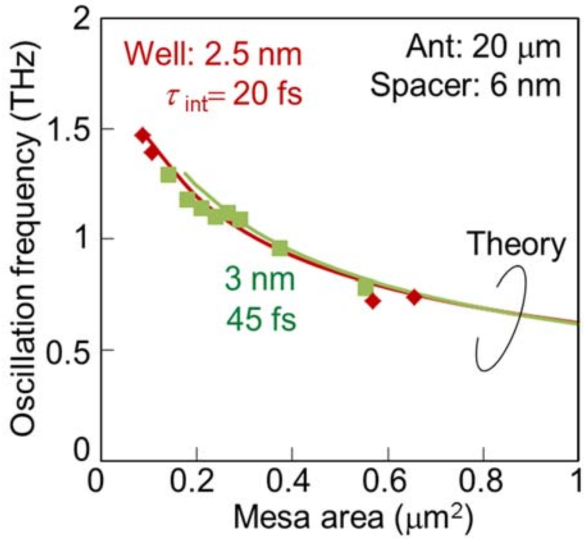

Fig. 3.23 Measured oscillation frequency as a function of RTD mesa area of RTDs with two different quantum-well thicknesses.

Next, oscillators were fabricated with the two RTDs, which had several mesa areas. I measured the dependence of the oscillation frequency on the thicknesses of the quantum well to obtain τ_{int} and its variation with the structure. The narrow-part widths of the air bridge from the top of the RTD to the MIM capacitance in Fig. 2.1 were 0.25 μm for the RTD with the 3-nm-thick well and 1 μm without InGaAs under air bridge for the RTD with the 2.5-nm-thick well , which reduced the antenna loss by improving the antenna structure, as discussed in Chapter 5. Fig. 3.23 shows the experimental results for the fundamental oscillation frequency as a function of the RTD mesa area. The length of the slot antenna is 20 μm. In addition to the difference in well thickness, the antenna structures in Fig. 2.1 also differ between the two RTDs. I estimated the intrinsic delay time τ_{int} and capacitance by fitting the theoretical calculation to the experimental results. The estimated τ_{int} were 45 and 20 fs for RTDs with 3- and 2.5-nm-thick well,

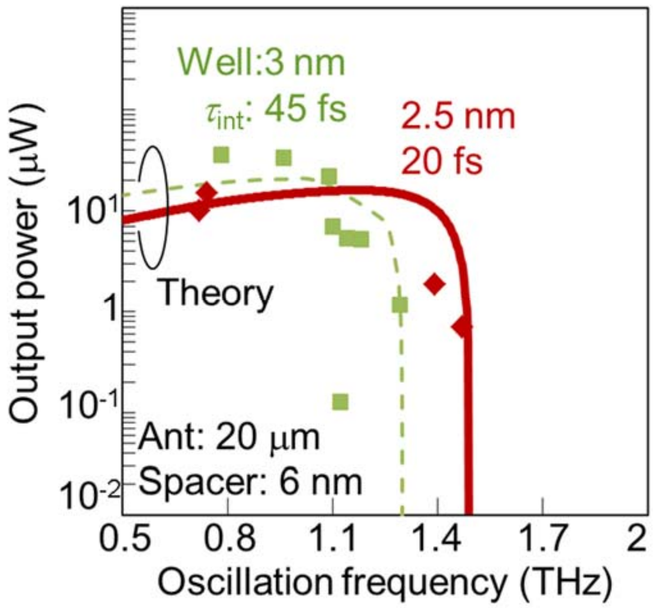

Fig. 3.24 Measured output power as a function of oscillation frequency of RTDs with different well thickness. The antenna length is 20 μm. Theoretical curves and extracted intrinsic delay time are also shown.

respectively. The estimated τ_{all} were 120 and 100 fs for RTDs with 3- and 2.5-nm-thick well, respectively. Details of the estimation method for τ_{int} were described in Chapter 2 and Ref. 3.9. The highest oscillation frequency increased by about 0.2 THz from 1.29 THz in the RTD with the 3-nm-thick well to 1.47 THz in the RTD with the 2.5-nm-thick well, as shown in Fig. 3.23. This was due to the reductions in the dwell time from the thin well and in the antenna loss from the antenna structure improvement, as discussed in Chapter 5. In this result, the contribution of the short dwell time to the increase in the highest oscillation frequency was comparable to or slightly larger than that of the small antenna loss. Although the reduction in the antenna loss was included in this experiment, the extraction of the intrinsic delay time for different well thicknesses was not affected by the difference in the antenna loss because the antenna parameter change calculated by HFSS was included. The output power was low because the oscillation frequency was very close to the highest limit as shown in Fig. 3.24. A higher output power is possible by improving the highest frequency limit, as discussed in Chapter 5. In the oscillation characteristics described above, the oscillation frequency and estimated delay time were improved by the thin well, as I expected.

3.4 Conclusion

This chapter discussed a mechanism for reducing the dwell time by reducing the well thickness for high frequency oscillation and the structures for reduction in bias voltage, which are deep well and step emitter structure. Next, the dependence of the *I*-*V* curve and oscillation characteristics on these structures were reported. An increase in the resonance level caused an increase in the FWHM of tunneling transmission coefficient and reduced dwell time. An increase in the bias voltage was suppressed using a deep well and an appropriate InAlGaAs step-emitter height. A decrease in the dwell time and increase in the oscillation frequency limit by a decrease in the well thickness without increase in bias voltage were achieved experimentally, as shown by comparing two RTDs with different well thicknesses and step emitter structure.

Chapter 4
High-frequency oscillation with reduced transit time

4.1 Introduction

This chapter analyzes the increase in the oscillation frequency of an RTD terahertz oscillator by a decrease in the transit time. The intrinsic delay, which is composed of the dwell time in the resonance region and the transit time in the collector depletion region, must be reduced to achieve the high-frequency oscillation of RTDs, as discussed in Chapter 2. Reducing the dwell time was discussed in Chapter 3. Although the transit time can be reduced using a thin collector spacer, the capacitance increases. Thus, an optimum thickness for the collector spacer layer exists. In this discussion, I investigate the dependence of *I*-*V* and the oscillation characteristics on the collector spacer thickness for obtaining optimum spacer thickness. The electron velocity in the collector depletion region, the dwell time, and transit time are also extracted from the dependence of the intrinsic delay on the collector spacer thickness.

4.2 Reduction in transit time with decrease in spacer thickness

The negative differential conductance used in the THz oscillation of RTDs degrades with increasing frequency because of the intrinsic delay time of electrons, which consists of the dwell time in the resonance region and the transit time across the collector depletion region. Therefore, a further increase in oscillation frequency requires a reduction in the intrinsic delay time. The dwell time, which is one of the factors in the intrinsic delay, can be reduced by thin quantum wells in Chapter 3.

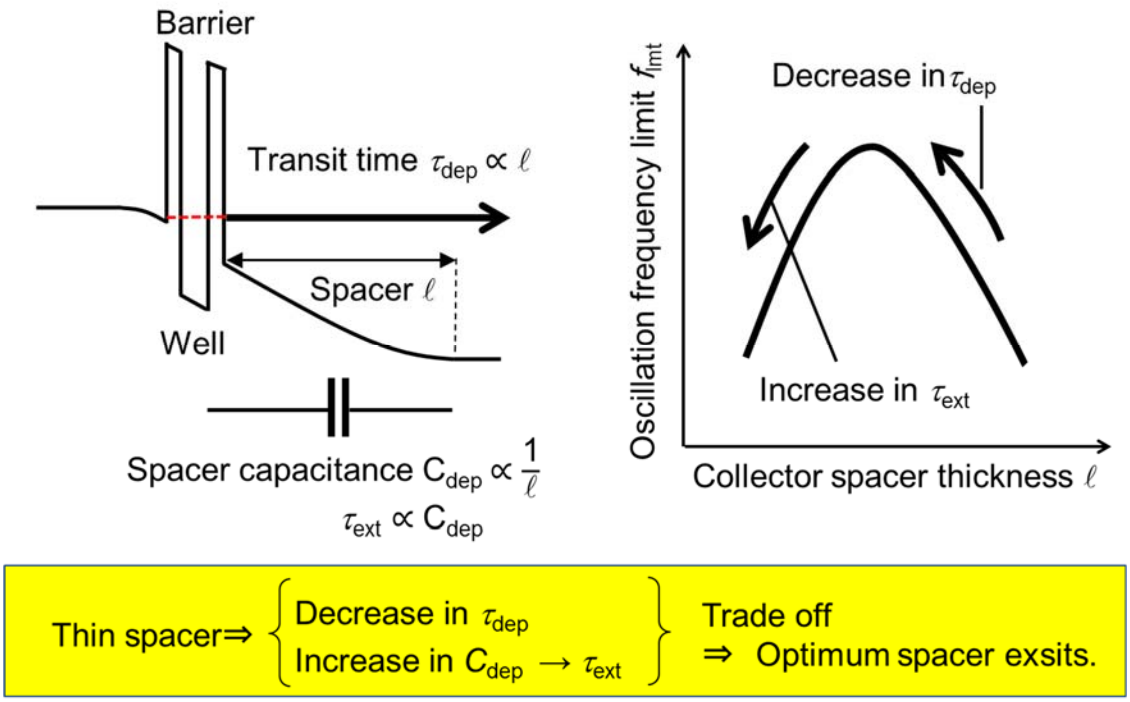

Fig. 4.1 Trade off of the transit time and spacer capacitance.

The other factor, the transit time in the collector depletion region, can be reduced by thinning the collector spacer thickness. However, an optimum spacer thickness exists because the capacitance of the depletion layer increases simultaneously, as shown in Fig. 4.1. Although the spacer thickness dependence of the oscillation frequency in RTDs has been studied at low frequencies (300–400 GHz) [4.1], the effect of the transit time was limited, and the optimum thickness was not a problem. The transit time is important in high-frequency oscillation after decrease in dwell time. In this chapter, I experimentally and theoretically investigated the spacer thickness dependence of oscillation frequency. I also extracted the electron velocity in the collector depletion region and the dwell time from the experimental results.

The electron velocity in a high electric field (~100 kV/cm) over a short distance (~10 nm) has not been reported. The theoretical oscillation frequency limits as a function of the collector layer width for several electron velocities in the collector depletion region are shown in Fig 4.2. Increasing the electron velocity increases the oscillation frequency limit because of the decrease in the transit delay time. The optimum spacer thickness increases with the electron velocity because the decrease in the velocity allows an increase in the collector spacer thickness and decrease in the capacitance of RTD.

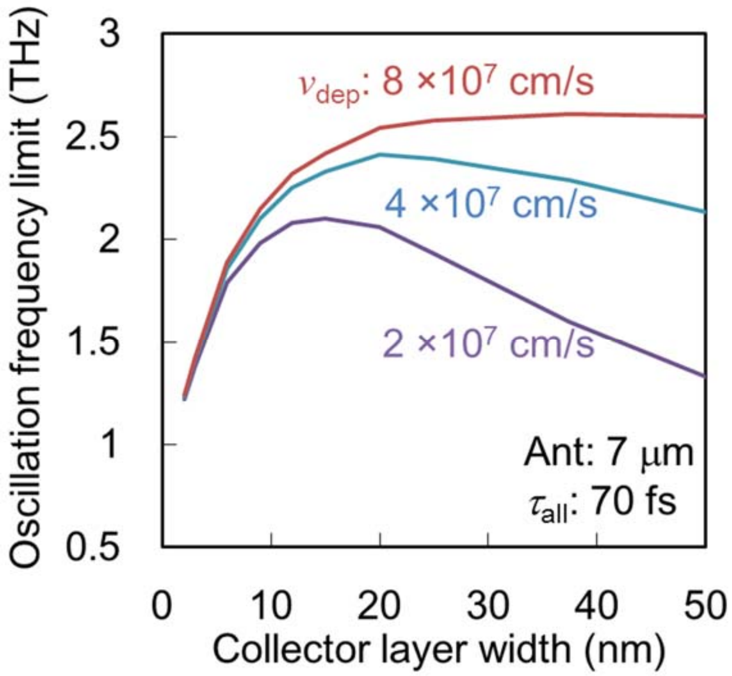

Fig. 4.2 Theoretical calculation of oscillation frequency vs. collector layer width for several electron velocities in collector depletion region.

4.3 *I*-*V* and oscillation characteristics

I prepared three RTD with spacer thickness of 25, 12 and 6 nm, as shown in Fig. 4.3. The barrier and well thickness in this experiment are designed in 1 and 3 nm, respectively. Step emitter height for reduction in bias voltage is 100 meV with $In_{0.53}Ga_{0.37}Al_{0.1}As$. The current-voltage characteristics of these RTDs are shown in Fig. 4.4. The voltage width ΔV of the NDC is larger for thicker spacers because the voltage drop across the spacer is larger. The current density width ΔJ of the NDC of the RTD with 25-nm-thick spacer is smaller than the two other RTDs. This is because the well thickness of the RTD with 25-nm-thick spacer is thicker by one monolayer than those of the others, which was confirmed by careful observation with a transmission electron microscope. The increase in the well thickness reduces the full width at half maximum of the energy spectrum of the tunneling transmission coefficient, reducing ΔJ. The peak current density was a little bit smaller for thicker spacers; the reason for this is not clear at present.

.

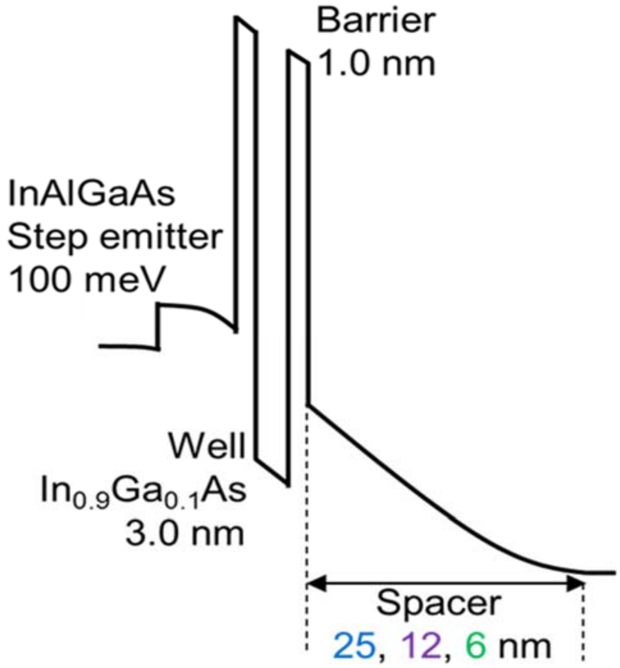

Fig. 4.3 Band diagram of the fabricated RTDs with spacer thickness of 25, 12, 6 n.m

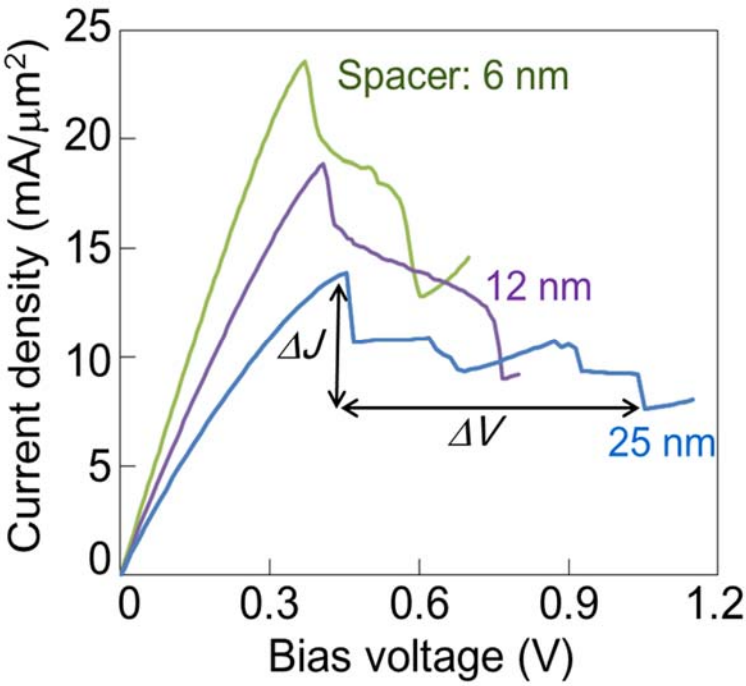

Fig. 4.4 Measured current-voltage characteristics of RTDs with different spacer thicknesses.

Fig. 4.5 shows the fundamental oscillation frequency measured at room temperature as a function of mesa area of the RTD for three samples with different collector spacer thicknesses. The oscillation frequency increased with the decrease in mesa area because of the decrease in capacitance of the RTD. For the same mesa area, the oscillation frequency is higher for samples with thicker spacers because the depletion-layer capacitance C_{dep} is smaller. The absolute value of NDC (G_{RTD}) decreases with the increase in oscillation frequency because of the intrinsic delay time and the decrease in mesa area. Because of this effect, there exists the highest limit to the oscillation frequency, above which the oscillation cannot be obtained because the G_{RTD} is insufficient to compensate for the radiation loss. The highest oscillation frequencies obtained in this experiment were 1.1, 1.42, and 1.29 THz for samples with spacer thicknesses of 25, 12, and 6 nm, respectively. Oscillation was not observed for mesa areas smaller than those for the highest frequencies. The oscillation frequency of the sample with a 12-nm-thick spacer was the highest. The highest frequencies for the other two spacer thicknesses were lower because of the increase in capacitance for the 6-nm-thick spacer and the increase in transit time for the 25-nm-thick spacer. The oscillation spectrum at the highest frequency (1.42 THz) for the 12-nm-thick spacer is shown in the inset of Fig. 4.5. The output power was ~1 μW, and the mesa area was 0.2 μm^2.

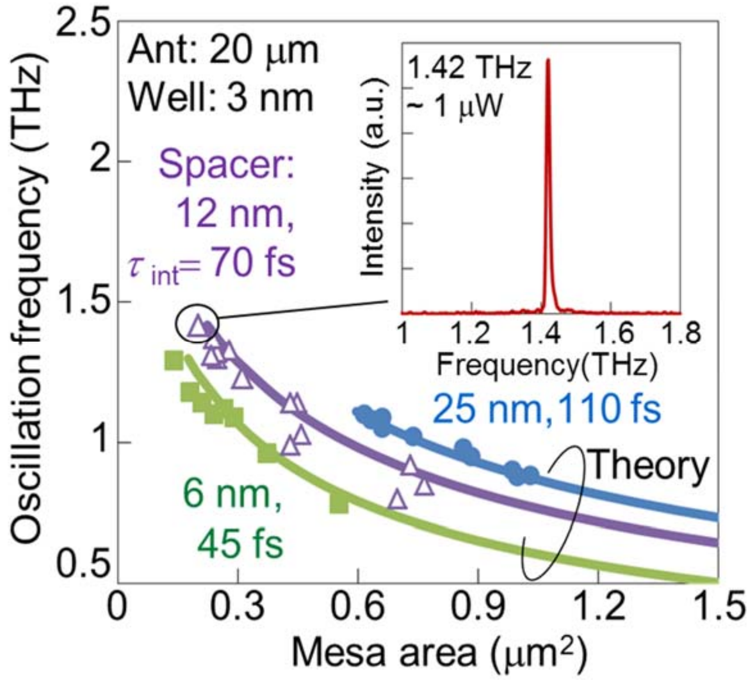

Fig. 4.5 Dependence of oscillation frequency on RTD mesa area for different spacer thicknesses. The inset is the measured spectrum of fundamental oscillation at 1.42 THz of the RTD with 12-nm thick spacer.

I estimated the intrinsic delay time τ_{int} and the capacitance by fitting the theoretical calculation to the experimental results. Details of the estimation method of τ_{int} are described in Chapter 2 and Ref. 4.2. The parasitic elements such as series resistance were taken into account in this analysis. However, C_{dep} per unit mesa area was treated as a fitting parameter here because the oscillation frequency strongly depends on C_{dep} per unit mesa area. In this process, the effect of τ_{ext} is implicitly included as those of the parasitic elements, and only τ_{int} is extracted. The fitting curves are shown in Fig. 4.4. The estimated τ_{int} times were 110, 70, and 45 fs for RTDs with 6-, 12-, and 25-nm-thick spacers, respectively. The estimated τ_{all} were 150, 110, and 120 fs for RTDs with 6-, 12-, and 25-nm-thick spacers, respectively. Fig. 4.6 shows the estimated and highest limit to the oscillation frequency as a function of spacer thickness. Since the dependence of τ_{int} on the collector spacer thickness is almost linear, as shown in Fig. 4.6, the dwell time τ_{dwell} was obtained from the intercept with an error of roughly $\pm$10 fs. From this result, the electron velocity in the spacer layer and the dwell time in the resonance region were estimated with the gradient and intercept as ~2×10^7 cm/s and 30 fs, respectively. This velocity is similar for those reported in, HBTs, HEMTs and UTC-PDs [4.3-5]. This is equivalently expressed as a large error bar for the 3-nm-thick well and 25-nm-thick spacer in Fig. 4.6, taking into consideration the difference in τ_{dwell} speculated from the difference in the well thickness, although it has little effect on the discussion in this chapter. The extension of the depletion region to the n^+-collector layer next to the spacer is negligibly small because of heavy doping (5×10^{19} cm^{-3}). In contrast to the highest limit to oscillation frequency has a maximum at a spacer thickness of 12 nm, as discussed above. τ_{dwell} was comparable to τ_{dep} for the 12-nm-spacer RTD.

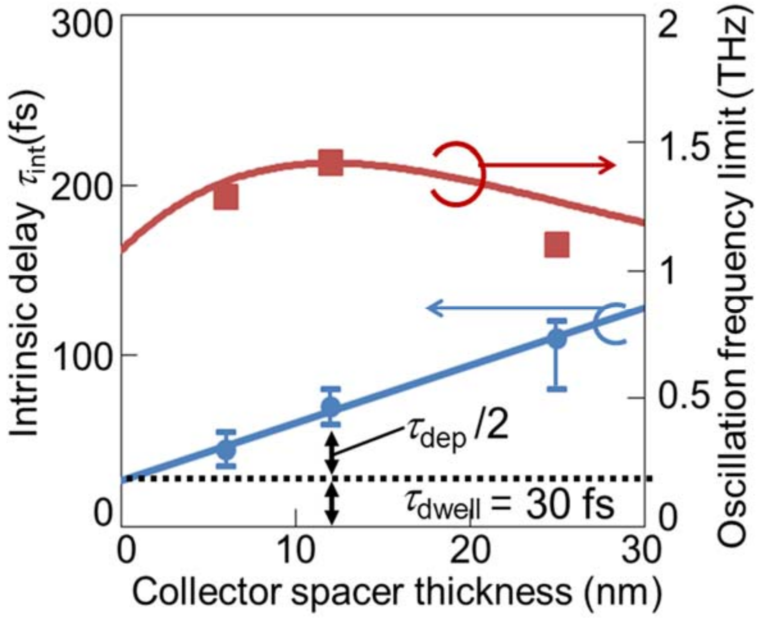

Fig. 4.6 Intrinsic delay time and the highest limit to oscillation frequency extracted by fitting between measurement and theory in Fig. 4.4 as a function of collector spacer thickness.

Fig. 4.7 shows the output power as a function of oscillation frequency for three RTDs with different collector thicknesses. The theoretical curves calculated with the analysis in Chapter 2 were also plotted. Because G_{RTD} decreases with increasing oscillation frequency, the output power abruptly falls off near the highest limit of the oscillation frequency. The output power of the sample with the 12-nm-thick spacer was about ~10 μW, and ~1 μW at the highest frequency of 1.42 THz.

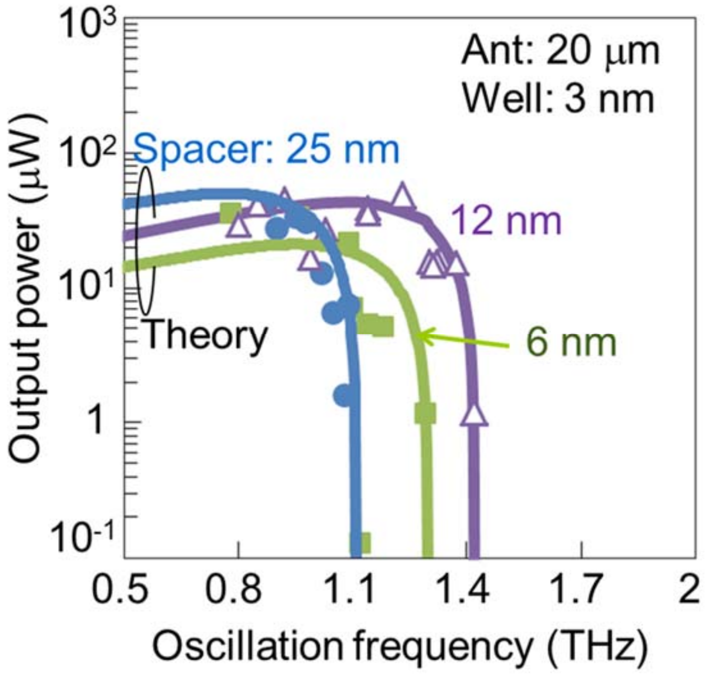

Fig. 4.7 Experimental and theoretical output power as a function of oscillation frequency for different spacer thicknesses.

4.4 Conclusion

This chapter investigated the dependence of the oscillation characteristics on the collector spacer thickness for terahertz oscillators using RTDs with planar slot antennas. Although the transit time in the collector depletion region decreases with decreasing collector spacer thickness, the capacitance increases. Thus, an optimum spacer thickness exists. The highest oscillation frequency of 1.42 THz was obtained at an optimum spacer thickness of 12 nm, with an output power of ~1 μW. From the dependence of intrinsic delay on the spacer thickness, the dwell and transit times are extracted and the effect for high frequency is almost same. A further increase in oscillation frequency is expected with decreasing the well thickness and improving the antenna structure.

Chapter 5 Structure for higher frequency and estimation of oscillation characteristics

5.1 Introduction

This chapter discusses structural changes to increase the frequency, along with the estimation of the oscillation characteristics. First, the reduction in the total delay by combining a thin well and optimum spacer, and a reduction in the series resistance, are discussed. Antenna length optimization and improvement to reduce the antenna loss are then discussed. Next, the estimation of the higher frequency provided by these improvements is discussed. Finally, this chapter reports, as preliminary work, the experimental achievement of fundamental oscillation up to 1.86 THz with reductions in the intrinsic delay, antenna length, and antenna loss, along with the removal of the InGaAs under the bridge.

5.2 Reduction in total delay

5.2.1 Integration of thin well and optimum spacer

Chapters 3 and 4 showed how a reduction in the dwell time with a reduction in the well thickness and reductions in the transit time and extrinsic delay with the optimization of the spacer thickness were achieved. This chapter discusses how the reductions in the intrinsic and extrinsic delays were simultaneously applied, as shown in Fig 5.1. The structure dependences of these factors were obtained in terms of the oscillation frequencies measured for RTD oscillators with different quantum well and collector spacer thicknesses.

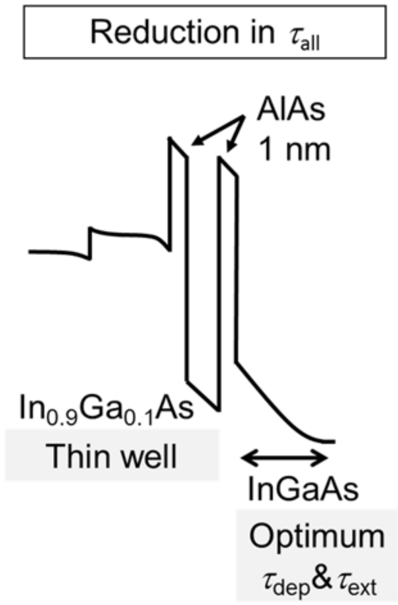

Fig. 5.1 Reduction in total delay with thin well and optimum spacer.

The intrinsic delay time was extracted from the experimental results for the intrinsic delay in Chapters 3 and 4 by a comparison with the results of a theoretical analysis using the equivalent circuit shown in Fig. 2.9. Based on the results of Chapter 4, the spacer thickness was almost optimized (~12 nm), which showed a good balance between the transit and extrinsic delay. The dwell time of the RTD with the 2.5-nm-thick well was estimated to be ~5 fs, as shown in Fig 5.2, using the results reported in the last part of this chapter. By combining the reduced well thickness and optimum spacer, a τ_{int} value of 35 fs was achieved. The RTD with the 2.5-nm-thick well and 12-nm spacer had an extrinsic delay time of 80 fs. Thus, a reduction in the extrinsic delay time is needed to increase the oscillation frequency from the viewpoint of improving the RTD layer structure.

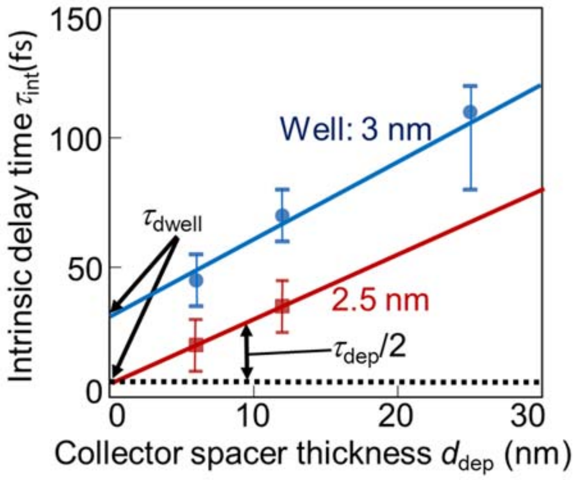

Fig. 5.2 Intrinsic delay time as function of collector spacer thickness for different well and spacer thicknesses in this research.

5.2.2 Reduction in series resistance of RTD

Reducing the series resistance is important because a decrease in the intrinsic delay causes an increase in the relative effect of the extrinsic delay. With comprehensive improvements in the dwell time, transit time, and extrinsic time, a τ_{int} value of 35 fs and τ_{ext} value of 80 fs were obtained with a 2.5-nm well and 12-nm spacer. To further increase the oscillation frequency limit, it was important to decrease the extrinsic delay time. To increase the oscillation frequency, in addition to decreasing the intrinsic delay, it was important to decrease the extrinsic delay, as mentioned at Chapter 2. The extrinsic delay time τ_{ext} is approximately expressed as $\tau_{ext} = (\pi/2)C_{RTD}\sqrt{R_s/G_{RTD}(0)}$, as mentioned in Chapter 2. To reduce the extrinsic delay, decreasing the series resistance could only provide an improvement because G_{RTD} was determined by the barrier and well thicknesses, and C_{RTD} was determined by the collector spacer layer thickness.

The series resistance R_s was the sum of the bulk and spread resistances. The bulk resistance was calculated as the sum of those for the doped InGaAs and InAlGaAs layers in the RTD mesa. The spread resistance of the InGaAs underlayer was approximated as $1/(\pi\sigma d_{\mathrm{InGaAs}})\ln(a/a_{\mathrm{mesa}})$ [5.1], where σ is the conductivity; and d_{InGaAs}, a, and a_{m} are the lengths indicated in Fig. 2.6. This resistance was approximately calculated to be that of a material with conductivity σ between two coaxial half-cylindrical electrodes with inner and outer radiuses a_{mesa} and a, respectively, and length d_{InGaAs}. In the above formula, d_{InGaAs} must be replaced with the skin depth δ if $\delta < d_{\mathrm{InGaAs}}$. The frequency dependence of σ was included as $\sigma(\omega) = \sigma(0)/[1+(\omega\tau_{\mathrm{rel}})^2]$, where $\tau_{\mathrm{rel}} = \mu\, m^* /e$ with μ, m^*, and e being the mobility, effective mass, and electron charge, respectively. The values of m^* and μ were estimated by the extrapolation of the heavily doped data in Refs. 5.2 and 5.3.

I estimated the extrinsic delay time τ_{ext} using Eq. (6) in Chapter 2. For an RTD with a 2.5-nm-thick well and 12-nm-thick spacer, which is discussed in the last part of this chapter, the calculated τ_{ext} was 80 fs. This value is more than double the value of τ_{int} (35 fs, as shown in the last part of this chapter) for this sample, implying that the reduction in R_{s} is essential for higher-frequency oscillation. R_{s} is composed of the bulk resistance of the mesa (n- and n^+- InAlGaAs step emitter layers, n^+-InGaAs collector layer, and n^+-contact layer) and the spread resistance of the n^+-InGaAs underlayer, as shown in Fig. 2.6. Although all of these layers are included in the calculation of R_{s}, the n-InAlGaAs layer is dominant. Therefore, a small d_1 in Fig. 2.6 is effective in reducing R_{s}. A large d_{InGaAs} for the underlayer in Fig. 2.6 is also effective if d_{InGaAs} is smaller than the skin depth. Fig. 5.4 shows the calculation for the dependence of the oscillation frequency limit f_{lmt} and τ_{ext} on the series resistance R_{s} for an RTD with a 2.5-nm-thick well, 12-nm-thick spacer, and 9-μm-long antenna, which is an almost optimized antenna structure for high frequency, as discussed later. The details of the antenna length optimization are discussed in Ref. 5.4 and this chapter below. A structure with improved d_1 and d_{InGaAs} is realistic using the present fabrication process. τ_{ext} can be reduced from ~80 to ~60 fs, and τ_{int} from ~90 to ~70 fs, by reducing d_1 from 20 to 10 nm and by increasing d_{InGaAs} from 400 to 600 nm, which is nearly equal to the skin depth at 2 THz. The series resistance depends on the mesa area. Thus, the values are compared at the oscillation frequency limit.

The RTD layer structure was optimized based on my knowledge of this structure. Although changing the material system such as InAs or InSb using a smaller effective mass may be attractive to enhance the oscillation frequency, I do not believe that this is effective for an application involving integration, such as with an HEMT amplifier, on a single wafer.

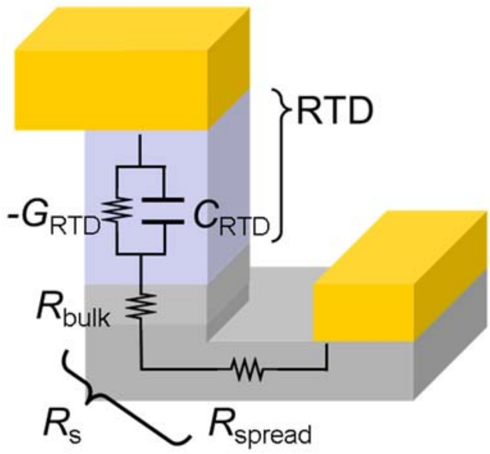

Fig. 5.3 Schematic structure of series resistance.

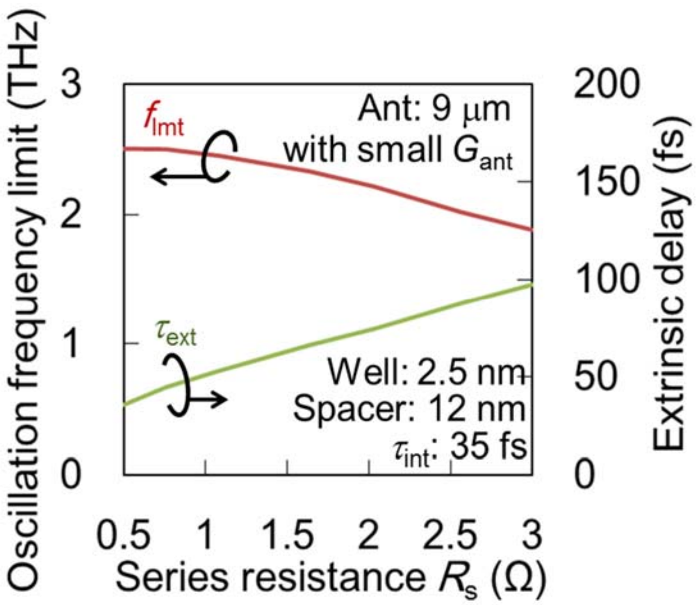

Fig. 5.4 Increase in oscillation frequency with reduction in extrinsic delay τ_{ext} and series resistance R_s at oscillation frequency limit.

5.3 Optimization of antenna structure

5.3.1 History of antenna structure improvement

There are three structures involved in the fabrication of a slot antenna: the first, air-gap, and air-bridge structures, as shown in Figs 5.5–7. The first structure was established in 2010 by our group. The process was a preliminary procedure. Therefore, it is complicated and difficult to use for the stable fabrication of devices. The gap between the top electrode and lower electrode near the RTD mesa was fabricated using tilted evaporation. Additionally, some of the characteristics were not good. The surface contact was not unstable because the top contact was evaporated after titanium was evaporated as an RIE mask and removed by buffered HF. This structure was used in [1.152, 155-158, 160].

To improve these defects, I changed the fabrication process from the first structure to the air-gap structure. In the air gap structure, the contact metal is first evaporated, with wafer cleaning by H_2O:HCL = 1:5 @ 4℃. Thus, the stability of the contact resistance increases. This main point of fabrication is the narrowest choke point of the air-bridge part. It was fabricated with a very narrow (~300 nm) shape, as shown in Fig 5.6(a), and isotropical wet etching was used to remove the InGaAs under this narrow part.

However, the antenna capacitance decreased with the air gap structure because of an increase in the distance between the bridge and the lower electrode. In addition to making it easier to fabricate, the thin part of the air gap causes an increase in the antenna inductance due to the narrow metal part, and the remaining portion of InGaAs inside the antenna causes an increase in the antenna conduction loss because of the reduction in the surface area under the bridge. The air-gap structure was used in [1.16-163, 166]

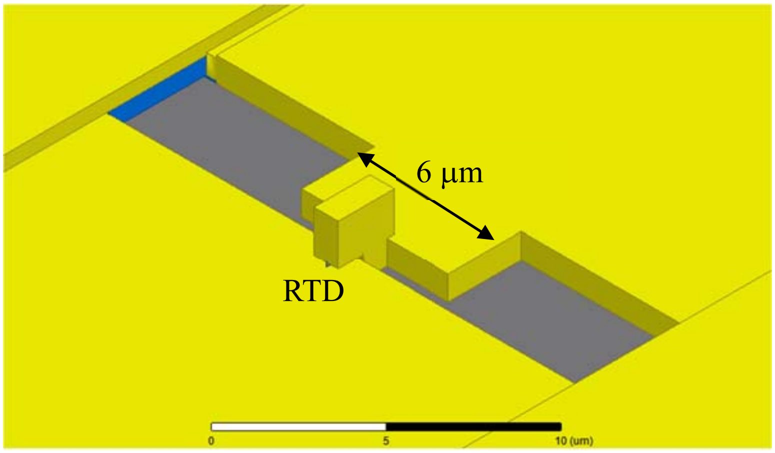

(a) Bird's eye view

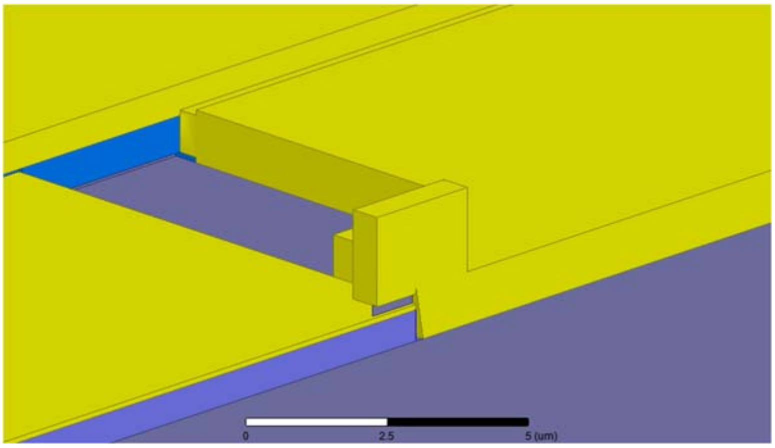

(b) Cross-sectional view near RTD mesa

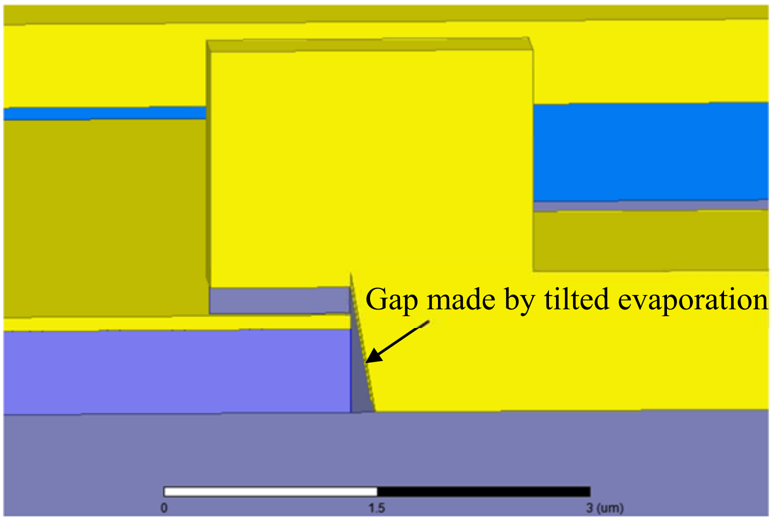

(c) Enlarged view near RTD mesa

Fig 5.5 Schematic diagrams of first structure.

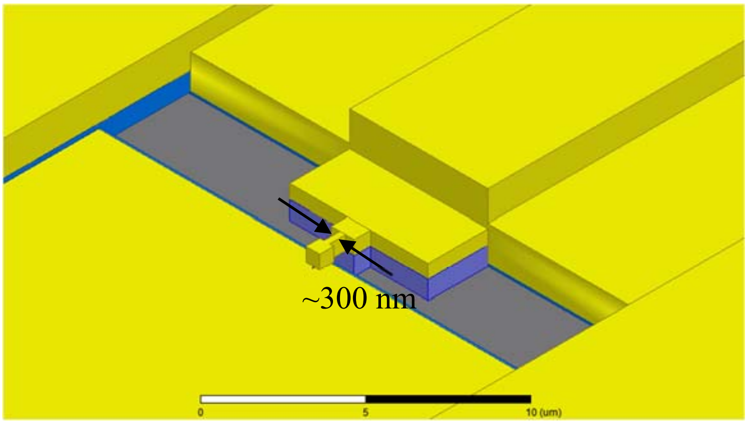

(a) Bird's eye view

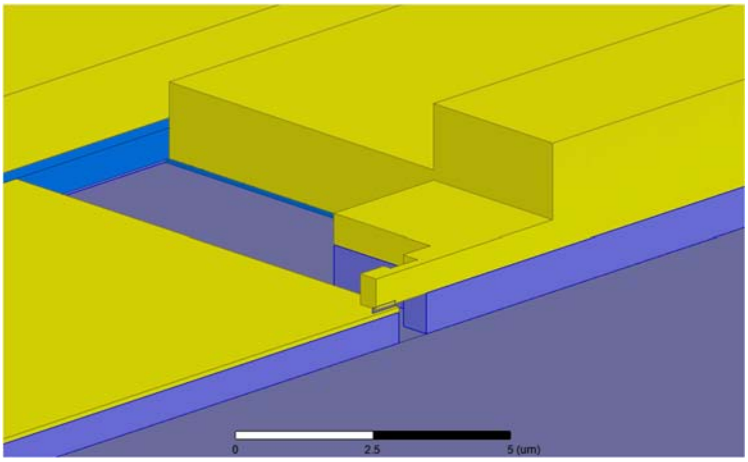

(b) Cross-sectional view near RTD mesa

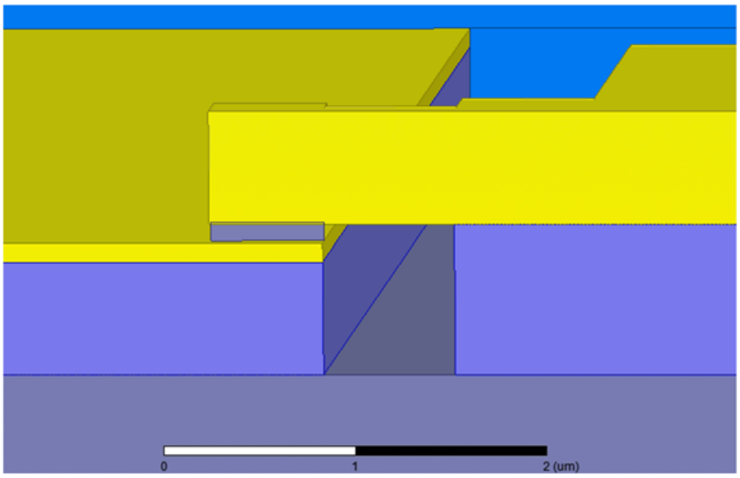

(c) Enlarged view near RTD mesa

Fig. 5.6 Schematic diagrams of air-gap structure.

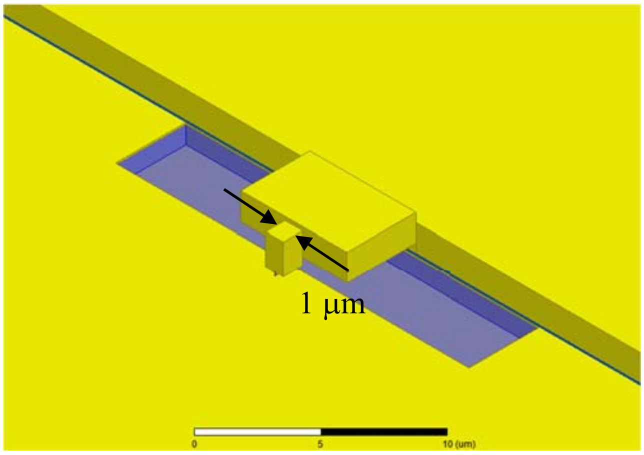

(a) Bird’s eye view

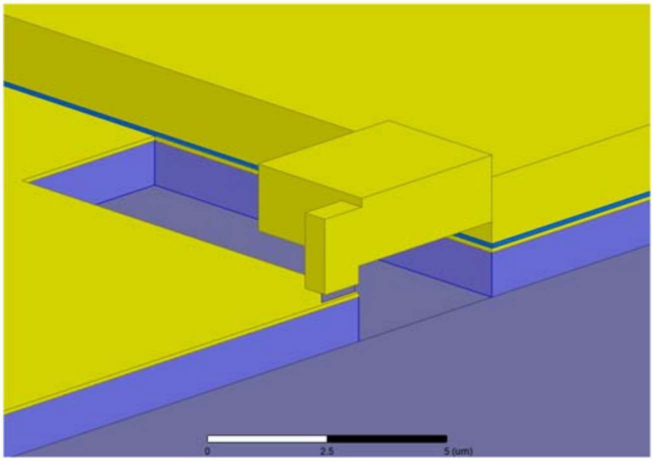

(b) Cross-sectional view near RTD mesa

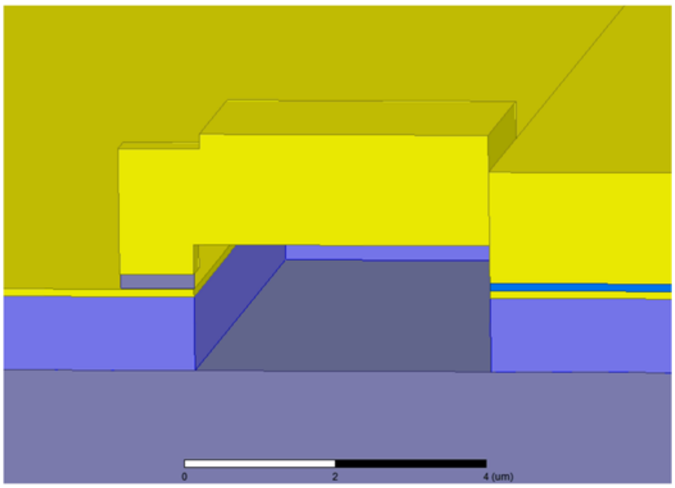

(c) Enlarged view near RTD mesa

Fig 5.7 Schematic diagrams of air-bridge structure.

In order to improve the antenna parameters, the air bridge structure was applied, along with the newest fabrication process. The details of this fabrication process were shown in Chapter 2. In this process, reductions in the antenna resistance and inductance were possible by increasing the surface area and improving the bridge length and width.

The characteristics of these three structures are summarized in Table 5.1. All of the antenna structures are discussed in this thesis, but only the air bridge structure is used for estimating the oscillation characteristics in this chapter. In addition, a further improvement in the air bridge structure will be shown in this chapter.

Table 5.1 Comparison of antenna structures.

Structure	First	Air gap	Air bridge
Fabrication	□	○	○
Antenna loss	○	□	○

5.3.2 Optimization of antenna length

Although there is an upper limit for increasing the oscillation frequency by decreasing the total delay, reducing the antenna length is the next approach for increasing the oscillation frequency. In our research group, Maekawa and I fabricated an RTD oscillator integrated with a slot antenna with the air-gap structure.

The oscillation of this device occurs if the NDC of the RTD compensates for the loss of the antenna, as discussed in Chapter 2. The oscillation frequency is determined by the capacitance and inductance of the equivalent circuit of the oscillator, including the RTD and antenna, as shown in Fig 2.9 and Fig. 2.11. By reducing the mesa area of the RTD, the oscillation frequency increases as a result of the decrease in the capacitance of the RTD. Because the NDC decreases with the decreasing mesa area, this method for increasing the frequency is limited to a certain value of the mesa area at which the NDC cannot overcome the loss of the antenna. The upper limit of the oscillation frequency determined from this condition can be extended by decreasing the antenna length, because of the decreases in the capacitance and inductance of the antenna.

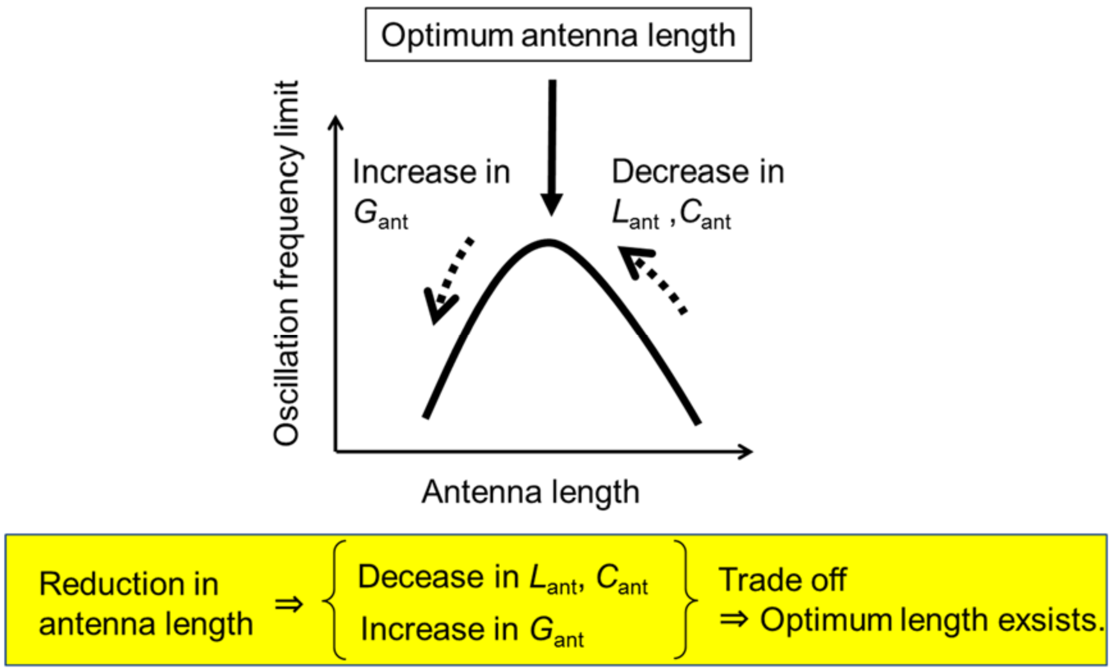

Fig. 5.8 Antenna length optimization.

However, the antenna loss increases with decreasing antenna length through the increase in the oscillation frequency, resulting in a decrease in the upper limit of the oscillation frequency. From this trade-off relation, as shown in Fig 5.8, there exists an optimum antenna length with respect to the upper limit of the oscillation frequency. The dependence of the upper limit of the oscillation frequency on the antenna length was examined using RTD oscillators with different antenna lengths. The RTD was composed of InGaAs/AlAs double barriers on an InP substrate, with the same layer structure as that in Section 4, except for the collector spacer thickness. The step emitter structure and deep quantum well were employed to reduce the bias voltage. The thicknesses of the quantum well and barriers were 3 and 1 nm, respectively, and that of the collector spacer was 12 nm.

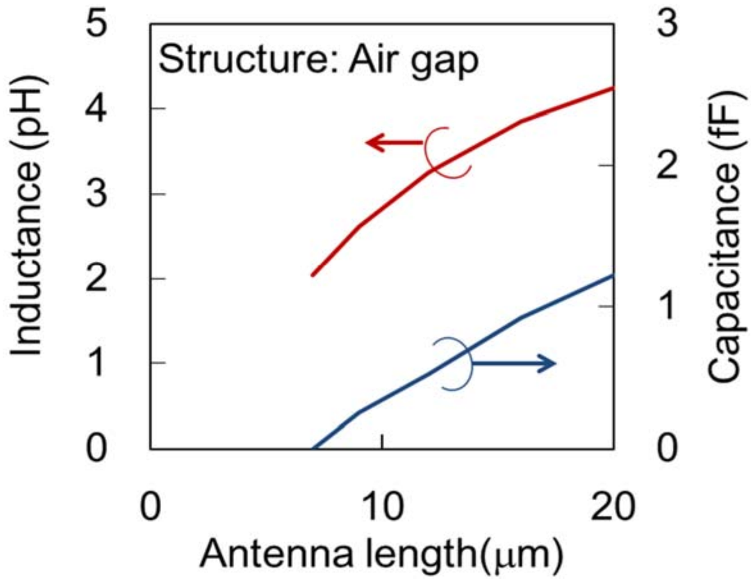

Fig. 5.9 Antenna inductance and capacitance vs. antenna length.

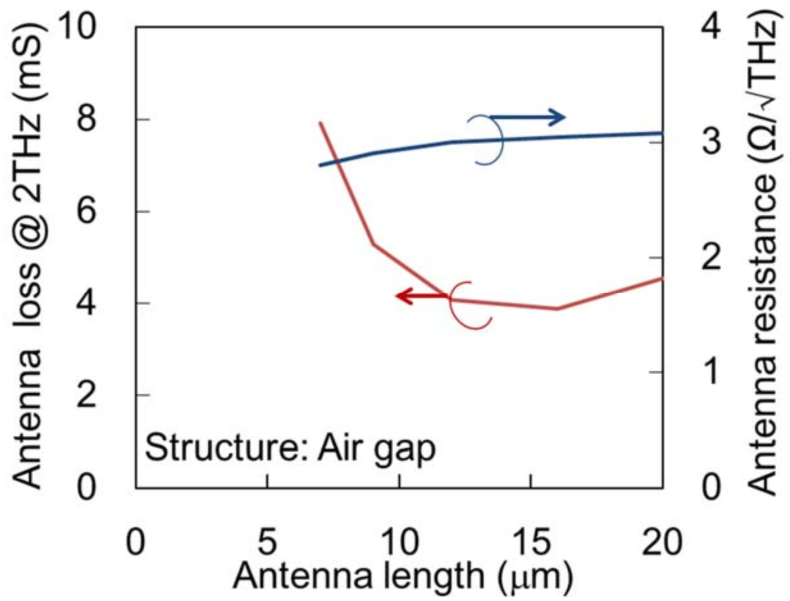

Fig. 5.10 Antenna admittance at frequency of 2 THz vs. antenna length.

The antenna inductance, capacitance, loss, and resistance of Air-gap structure as functions of the antenna length are shown in Figs. 5.9 and 5.10, which were obtained by fitting the admittance calculated by HFSS and the parameters of the circuit model shown in Fig 2.11. The antenna inductance and capacitance are almost proportional to the antenna length. The antenna inductance increases with the slot antenna area, and the capacitance increases with an increase in the part between the upper and lower electrodes, which face each other.

Fig. 5.11 shows the fundamental oscillation frequencies measured at room temperature against the mesa area of the RTD for different antenna lengths. The oscillation frequency increased with decreasing mesa area, as previously mentioned. For the same mesa area, the oscillation frequency was higher for shorter antennas because of the small capacitance and inductance. Theoretical curves are also shown in Fig. 5.11, which were calculated using the method and parameters for the RTD discussed in this thesis. The upper ends of the theoretical curves correspond to the upper limit of the oscillation frequency. Reasonable agreement between the theory and experiment was obtained. The highest oscillation frequencies obtained in the experimental results shown in Fig. 5.11 were 1.42, 1.55, 1.53, and 1.40 THz for antenna lengths of 20, 16, 12, and 9 μm, respectively [5.4]. The output power of the highest oscillation frequency (1.55 THz) for a 16-μm-long antenna was 0.4 μW, which was close to the upper limit of the oscillation frequency, as seen in Fig. 5.11. On the other hand, that for a 12-μm-long antenna (1.53 THz) was 5 μW, which showed some room before reaching the upper limit of the oscillation frequency.

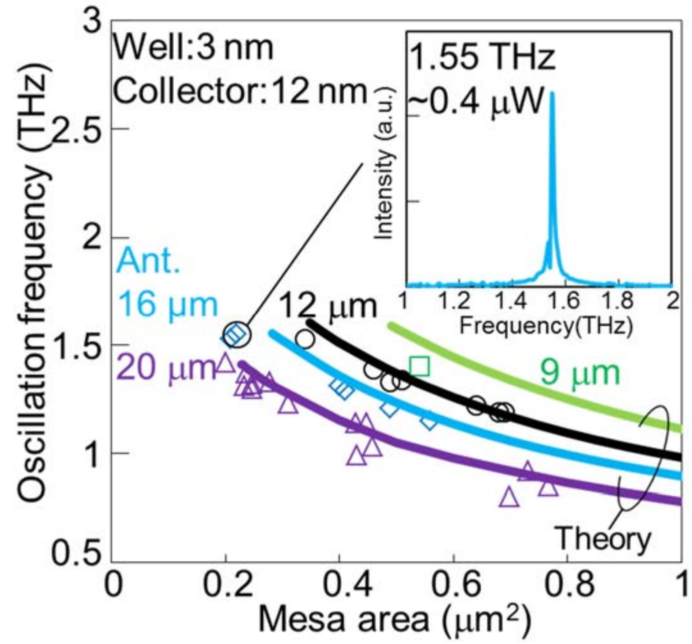

Fig. 5.11 Antenna inductance and capacitance versus antenna length.

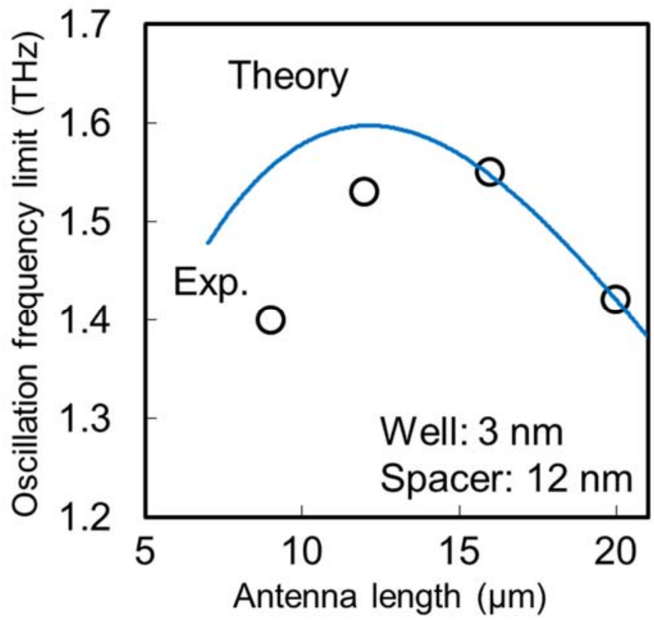

Fig. 5.12 Antenna inductance and capacitance versus antenna length.

The dependence of the upper limit of the oscillation frequency on the antenna length was obtained from the theoretical curves in Figs. 5.11 and 5.12. As discussed above, there is an optimum antenna length for the upper limit of the oscillation frequency. The highest oscillation frequencies obtained in the experiment are also plotted in Fig. 5.12. Although they are not exactly equal to the upper limit, as shown above, a similar dependence on the antenna length was obtained.

5.3.3 Reduction in antenna conduction loss

Decreasing the antenna loss is important to increase the oscillation frequency. The antenna loss consists of radiation, conduction, and leakage losses. The main part of the antenna loss is conduction loss in a short antenna. A reduction in the antenna resistance is needed to further increase the oscillation frequency limit. The antenna loss Re(Y_a) for a short antenna (less than ~20 μm), as shown in Fig 2.11, was approximated because the radiation conductance was about one tenth that of Re(Y_a):

$$\mathrm{Re}(Y_a) \approx R_{cond}\sqrt{f}/(R_{cond}^2 f + (2\pi f L_{ant})^2), \qquad (7)$$

where f is the frequency. In order to decrease in the antenna admittance calculated by Eq. (7), a reduction in R_{cond} was important, as shown in Fig. 5.13. f_{max} is the maximum oscillation frequency, as calculated by the following equation: $G_{RTD}\cos 2\pi f_{max} = 0$.

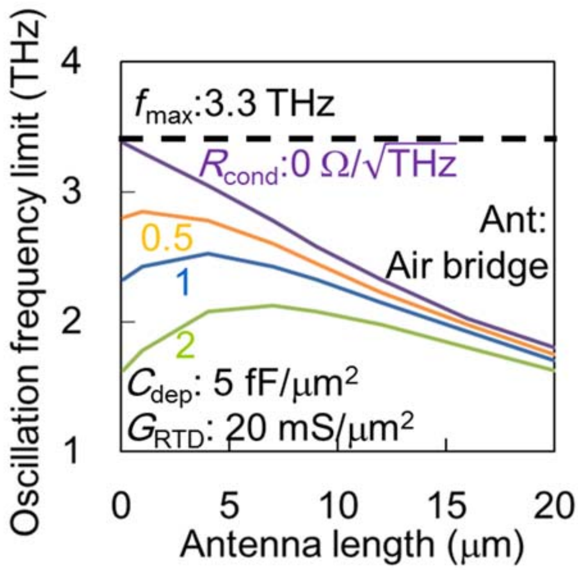

Fig. 5.13 Oscillation frequency limit versus antenna length with reduction in antenna resistance calculated with usual air bridge structure.

Increasing the surface area of the air bridge and thickness of the lower electrode are effective ways to decrease the conduction loss, because terahertz waves propagate only on metal surfaces (~50 nm at 2 THz) because of the skin effect. Fig. 5.14 shows the device structures and surface current simulation results by HFSS for the air-gap and air-bridge structures. Because of the improvement in fabrication process using the air-bridge structure, which used a 3-layer resist technique, as explained in Chapter 2, the InGaAs under the air bridge was not formed. Thus, the conduction loss decreased with an increase in the surface area of the air bridge [5.5]. The antenna length of the air-gap structure was limited to ~7 μm because the air-bridge width of wide part was fixed at 6 μm in this thesis to prevent interference between the slot antenna and air bridge. There was no limitation on the air-bridge shape for the air-bridge structure because of the improvement in the fabrication process, in which the air bridge was completely isolated from the lower electrode antenna.

Fig. 5.15 shows the dependence of the antenna loss on the antenna length. Decreasing the antenna length increased the loss, as shown by Eq. (7). A long antenna has a large oscillation conductance. Thus, a tendency for the antenna loss to increase with the antenna length also exists. Fig. 5.16 shows the dependence of the antenna resistance on the antenna length. An increase in the bridge surface causes a decrease in the antenna loss in a comparison of the air-gap and air-bridge structures. The antenna resistance increases with the antenna length. The slopes of the tendencies for these two structures changed because the thickness of the gold around the slot changed.

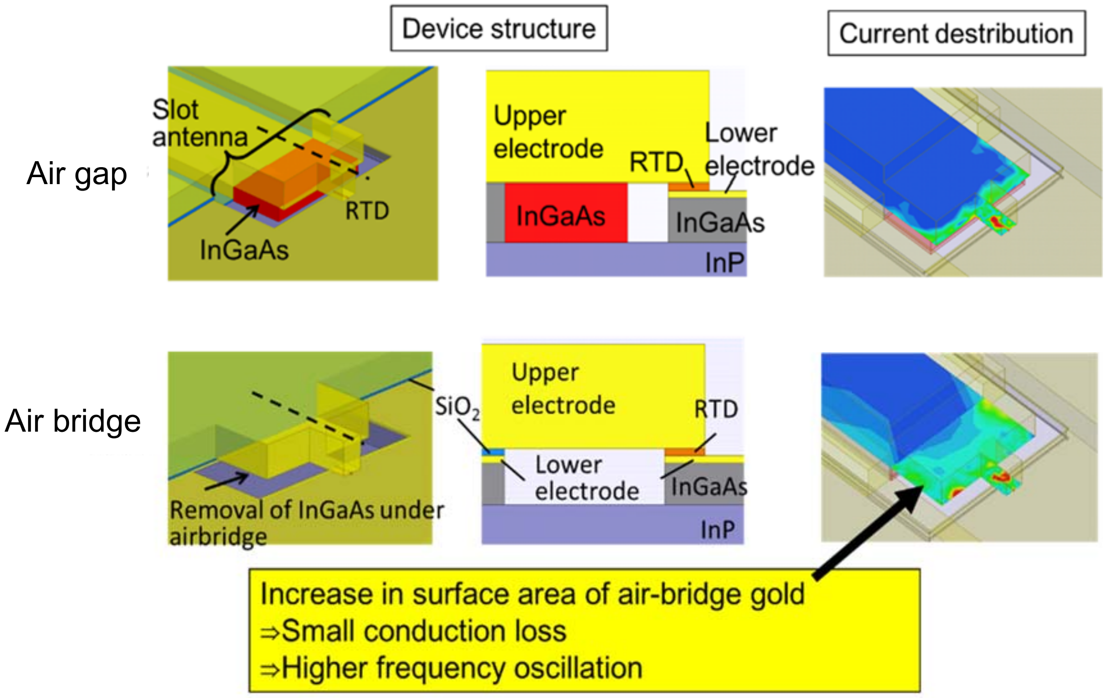

Fig. 5.14 Reduction in antenna loss with reduction in InGaAs under air bridge.

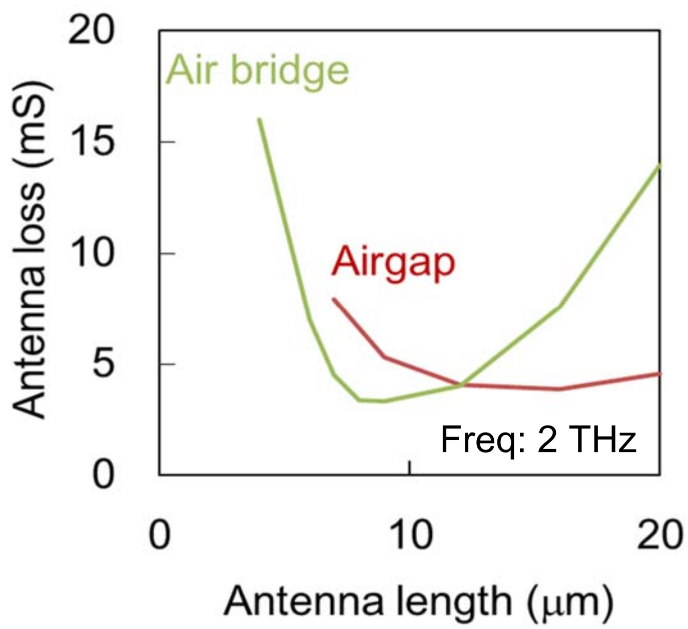

Fig. 5.15 Antenna loss versus antenna length for air-gap and air-bridge structures.

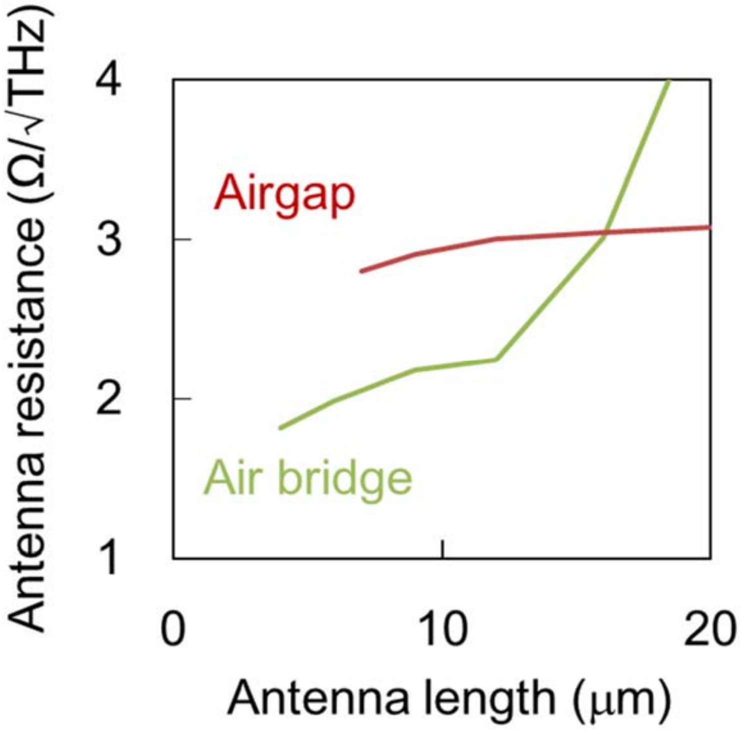

Fig. 5.16 Antenna resistance versus antenna length for air-gap and air-bridge structures.

Increasing the lower-electrode thickness is an effective way to further decrease the antenna resistance, and it is easy to fabricate after finishing the fabrication of the device. Although this additional lower-electrode structure was mainly proposed by Maekawa in our group, I calculated the antenna parameters to estimate the oscillation frequency limit in this thesis.

The fabrication includes the following steps: covering the structure with a ~50-nm-thick layer of SiO_2 using PCVD for passivation between the additional lower electrode and MIM structure, removing the SiO_2 on the lower electrode and contact pad, and evaporating Cr/Au = 10/~2000 nm. The additional lower-electrode thickness was determined by the point where the antenna improvement was almost saturated, as well as the easiness of the fabrication process. A 2-μm-thick metal layer was easy for our group to fabricate during a single evaporation. Furthermore, an increase in the thickness is possible by increasing the evaporation times of the metals. The device structure after evaporating the additional material for the lower electrode is shown in Fig. 5.17. The gap between the RTD mesa and thicker lower electrode is 1 μm out of consideration for the leakage between the upper and lower electrodes and the easiness of the lift-off process.

The calculated antenna loss, resistance, inductance, and capacitance are shown in Figs. 5.18 and 5.19. The antenna inductance increases with an increase in the lower electrode thickness, because of the increase in the surface area along the slot, which is similar to increasing the diameter of a wire. Thus, the antenna loss increases, but the antenna resistance decreases because of the increase in the metal thickness. An increase in the oscillation frequency limit was possible with the simultaneous increase in the lower electrode thickness and optimization of the antenna length.

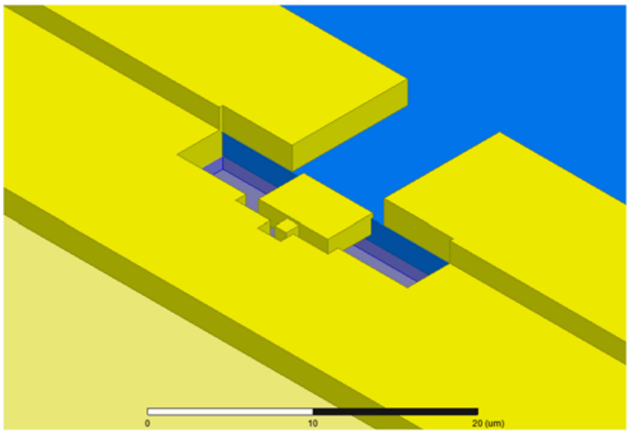

(a) Bird's eye view of additional lower electrode thickness

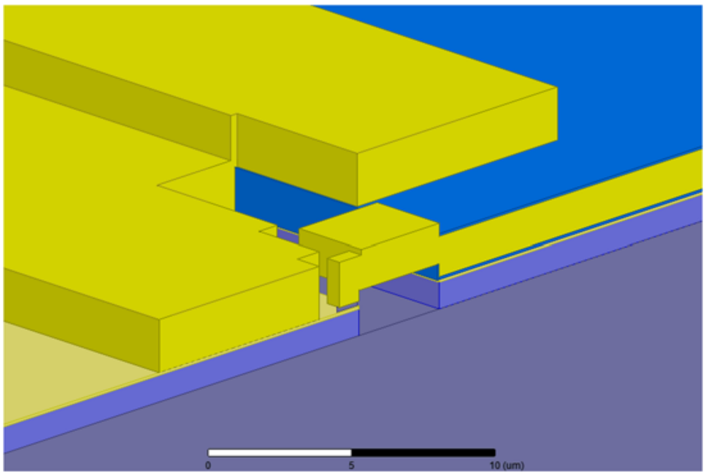

(b) Cross-sectional view

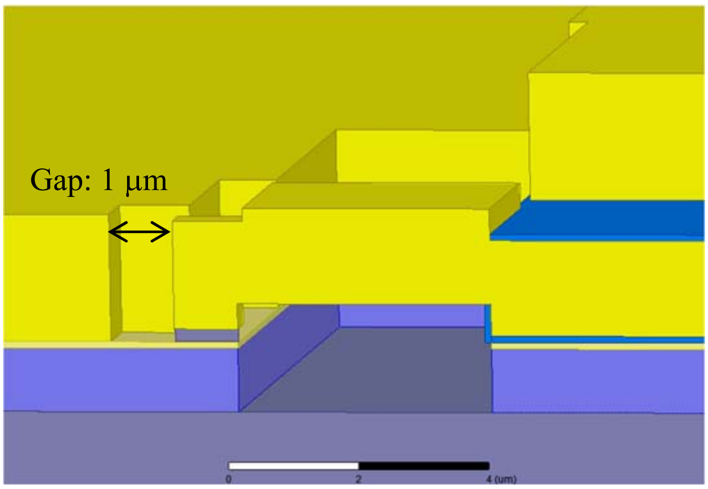

(c) Enlarged view

Fig 5.17 Schematic antenna structures with thicker lower electrode structure.

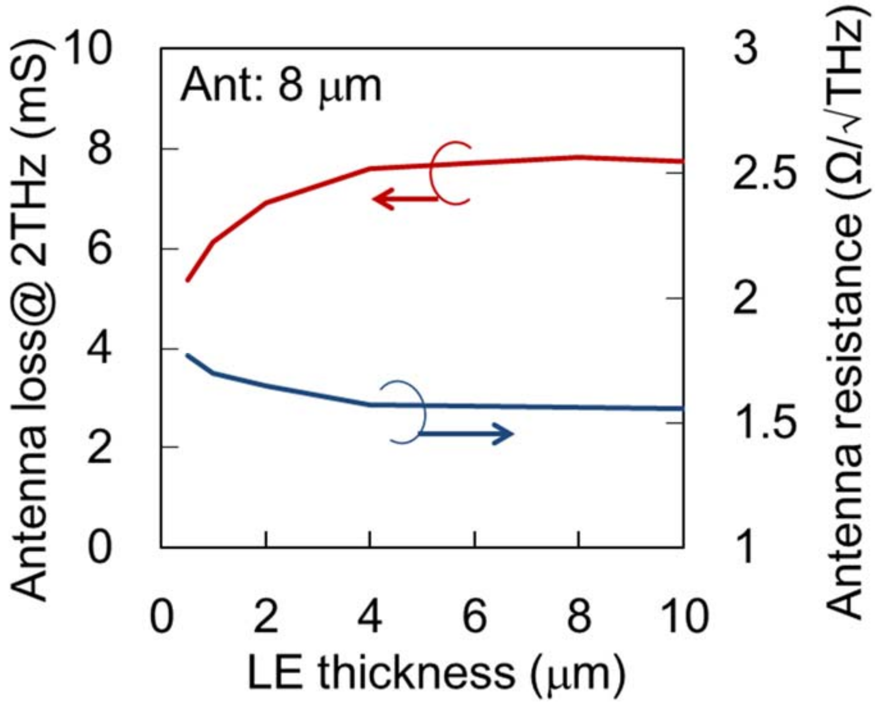

Fig. 5.18 Antenna loss and resistance versus lower electrode thickness.

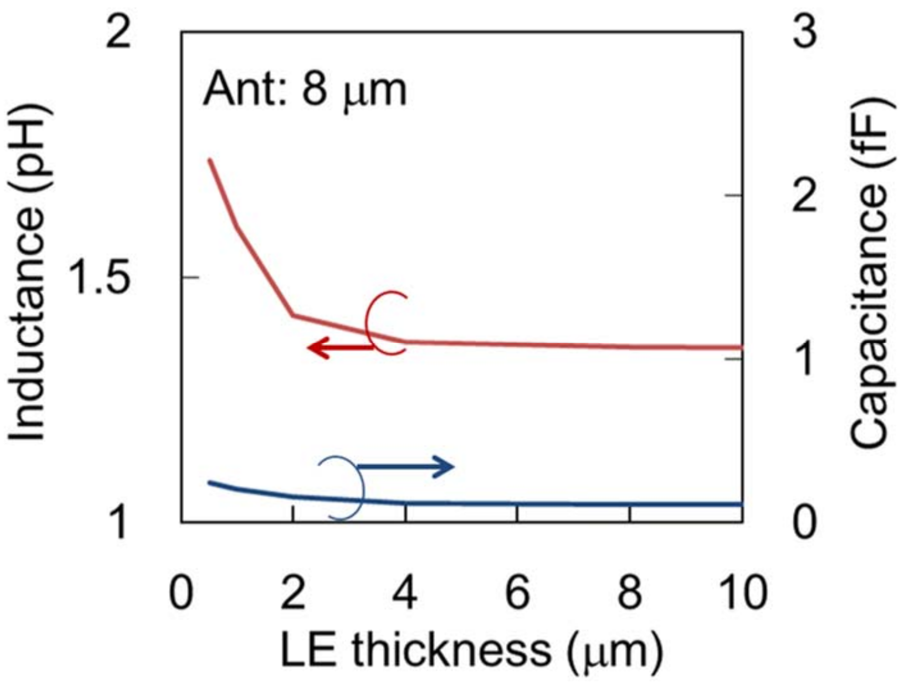

Fig. 5.19 Antenna inductance and capacitance versus lower electrode thickness.

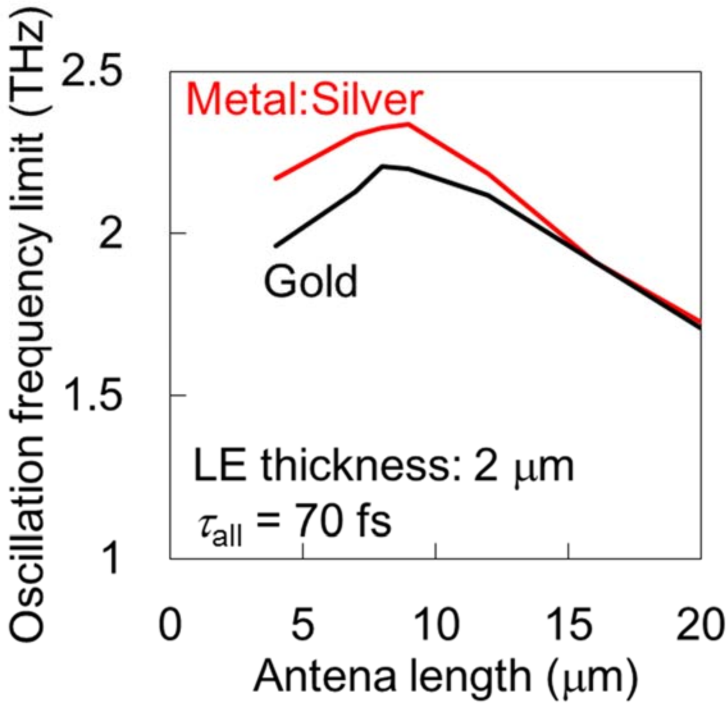

Fig. 5.20 Oscillation frequency limit versus antenna length with 2-μm lower electrode and silver as metal.

The upper limit of the oscillation frequency could be increased by decreasing the antenna resistance. Exchanging the gold for silver was also an effective way to further decrease the antenna resistance, because the conductivity of silver is ~1.4-times greater than that of gold. The upper red curve in Fig. 5.20 is the theoretical upper limit of the oscillation frequency expected for an RTD oscillator with a silver antenna. The antenna resistance was decreased with a silver antenna, and the degradation of NDC at high frequency was compensated. In this calculation, the total delay was assumed to be 70 fs using an RTD with a 2.5-nm well, 12-nm spacer, and reduction in the series resistance. A lower electrode thickness of 2 μm was used to decrease the antenna resistance and inductance. Based on the upper curve in Fig. 5.20, an oscillation frequency upper limit of >2 THz is expected at the optimum antenna length (~9 μm).

5.4 Estimation of higher frequency and experimental result of 1.86 THz

Fig. 5.21 shows the theoretical output power as a function of the oscillation frequency expected from the above-mentioned structure improvement. The dashed curves show the results for the previous RTD (R_s = 4 Ω at f_{lmt} and τ = 90 fs) and the improved RTD (3 Ω at f_{lmt} and 70 fs). Using a slot antenna with a length of 12 μm without InGaAs under air bridge, the highest limit of oscillation frequency f_{lmt} discussed in Chapter 2 was obtained as the frequency at which the output power fell to zero. An oscillation frequency of over 2 THz is theoretically possible by reducing τ_{all} and improving the antenna structure. The experimental result mentioned below is also shown.

The calculation result using the previously mentioned improved RTD and the offset-fed slot antenna [5.6] with silver as the metal and a lower-electrode thickness of 2 μm is also shown by the solid curve in Fig. 5.21, demonstrating the improved output power. The offset, antenna length, and RTD mesa area were adjusted to maximize the output power at each frequency. Output power values of ~500 μW at approximately 1 THz and >1 mW at 0.5 THz are expected as a result of this improvement. For instance, the theoretical efficiency at 1 THz from DC to RF calculated by the theoretical maximum power per consumption power at the center of NDR is about 5%, neglecting the power consumption of the resistance used to suppress parasitic oscillation (if the optimized resistance is considered, the value becomes 1/2). To further increase the output power, the optimization of the antenna width was reported for impedance matching between an RTD and an antenna [5.7], along with the array configuration [5.6].

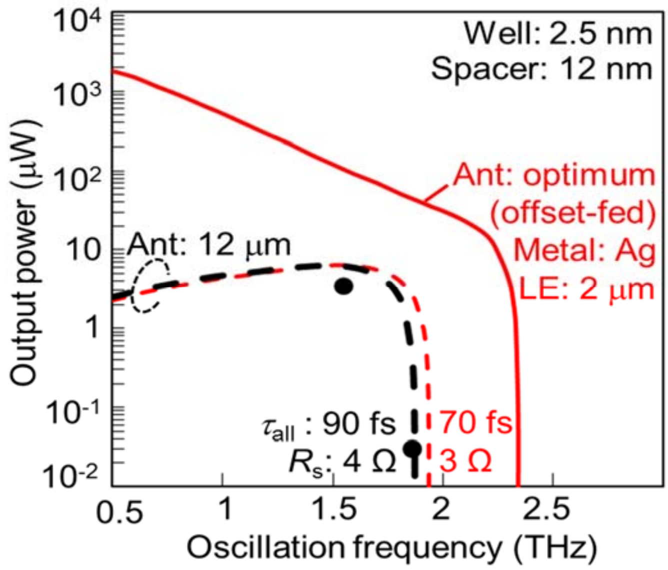

Fig. 5.21 Theoretical output power as function of oscillation frequency for RTDs with resistances of 4 and 3 Ω at f_{lmt}, and 12-μm antenna without InGaAs under air bridge shown by dotted black and red curves. The red solid curve shows the estimation for the optimum antenna offset-fed for each oscillation frequency, with silver and a lower electrode thickness of 2 μm.

Actually, as preliminary work for the above discussion, by integrating the thin well (2.5 nm) and optimum spacer (12 nm) and improving the antenna (the 12-μm long slot antenna without InGaAs under an air bridge), a 1.86-THz oscillation was achieved, as shown in Fig. 5.22, with the oscillation spectrum shown in Fig 5.23. The intrinsic delay was 35 fs, and the delay time was 90 fs. The reduction in the antenna loss was about 30% based on the theoretical calculation in HFSS. Increasing the antenna thickness and changing the metal from gold to silver are the next steps to obtain oscillation at a frequency greater than 2 THz.

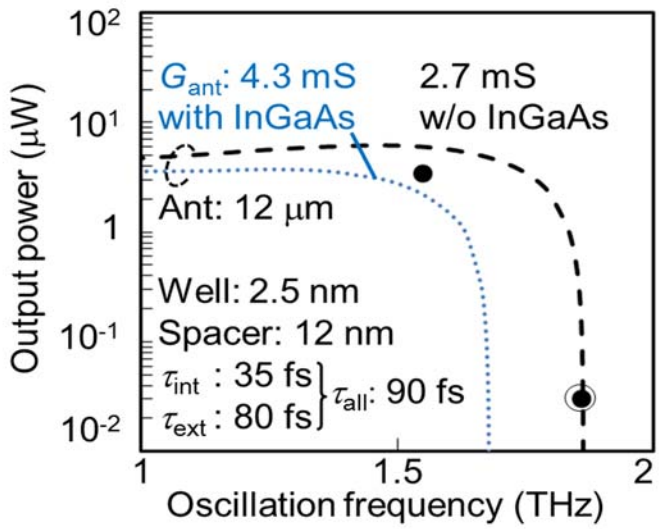

Fig 5.22 Theoretical curves with and without InGaAs under air bridge. Black dots show the experimental results with the air-bridge structure.

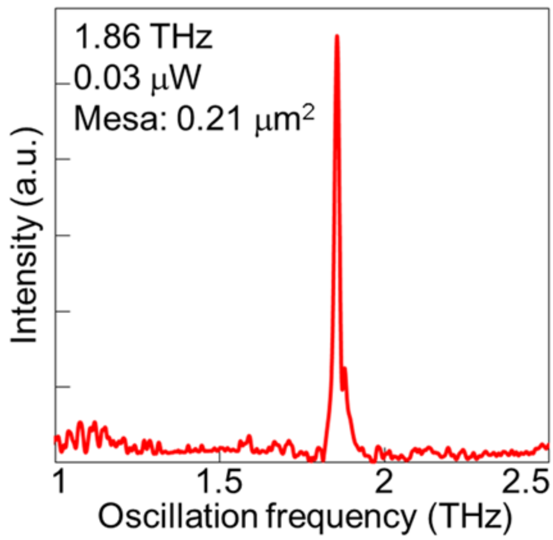

Fig 5.23 Measured spectrum of fundamental oscillation at 1.86 THz.

5.5 Conclusion

This chapter discussed the increase in the oscillation frequency provided by decreasing the intrinsic and extrinsic delay times of RTD terahertz oscillators, as well as the antenna length and loss. The intrinsic delay time is composed of the dwell time in the resonant tunneling region and the electron transit time in the collector depletion region. This chapter discussed the results of combining a thin well, optimum spacer, reduction in series resistance, optimum antenna length, and reduction in antenna loss by removing InGaAs under air bridge, increasing the antenna metal thickness, and changing the material from gold to silver. It was shown theoretically that an oscillation frequency of over 2 THz is possible upon the reduction in the total delay time to 70 fs as a result of the bulk and spread resistances of the RTDs and the antenna structure improvement.

As preliminary research, an oscillation frequency of 1.86 THz was obtained in an experiment using well and spacer thicknesses of 2.5 and 12 nm, respectively, without InGaAs under an air bridge.

Chapter 6
Conclusion

Chapter 1 discussed the background and purpose of this study. The terahertz (THz) range is between approximately 100 GHz and 10 THz, or the top edge of the millimeter wave range and the bottom edge of the optical wave range. It has been an almost unexplored frequency range because of the lack of compact sources. Recent technological innovations in nanotechnology and photonics are now enabling terahertz research and applications, including those in the fields of ultrahigh-speed wireless communication, imaging, and spectroscopy. I studied ways to achieve a compact terahertz source for use in terahertz applications through the development of an RTD oscillator, which is one of the candidates for a compact light source. The first chapter discussed the unique features of the terahertz frequency range, along with some applications. Next, terahertz source candidates with those characteristics were described. The details and advantages of RTD oscillators were shown and compared with those of other sources. Finally, the purpose and outline of this thesis were provided.

Chapter 2 discussed the device structure, fabrication process, theoretical analysis of an RTD-terahertz oscillator with a planar slot antenna, and approaches for high frequency. Reductions in the total delay time, antenna length, and antenna loss were proposed to increase the oscillation frequency. The total delay time was shown to consist of intrinsic and extrinsic delays. The intrinsic delay includes the dwell time through the double barrier and transit time across the depletion layer. The extrinsic time is caused by parasitic elements such as the capacitance and series resistance of the RTDs.

To obtaining an oscillation at a frequency greater than 2 THz, a total delay of 70 fs, antenna length of 9 μm, and antenna loss of less than 8 mS are needed.

Chapter 3 discussed the mechanism to reduce the dwell time by reducing the barrier and well thickness, which would also include a reduction in the bias voltage with a deep well and step emitter structure. The dwell time through the double RTD barrier will be reduced by a thin barrier and well. A thin barrier caused an increase in the full width of the half maximum (FWHM) of the tunneling transmission coefficient, which was inversely proportional to the dwell time. An increase in the resonance level in a quantum well with a reduction in the well thickness also caused an increase in the FWHM of the tunneling transmission coefficient. The increase in the bias voltage due to the thin well was suppressed with an appropriate InGaAlAs step-emitter height and In-rich deep well. A decrease in the dwell time and increase in the oscillation frequency limit with a decrease in the well thickness without an increase in the bias voltage were experimentally achieved, as shown by a comparison of two RTDs with different well thicknesses of 3 and 2.5 nm and step emitter heights of 100 and 150 meV. The oscillation frequency increased from 1.29 to 1.47 with a decrease in the total delay from 120 to 100 fs.

In Chapter 4, I investigated the dependence of the oscillation characteristics on the collector spacer thickness for terahertz RTD oscillators. Although the transit time in the collector depletion region decreased with a decrease in the collector spacer thickness, the capacitance and extrinsic delay increased. Thus, an optimum spacer thickness exists. The highest oscillation frequency increase, from 1.1 to 1.42 THz, was obtained by decreasing the RTD spacer thickness from 25 to 12 nm, with a 12-nm spacer found to be the optimum size. The total delay decreased from 150 fs to 110 fs with spacer thicknesses of 25 to 12 nm, respectively. The dwell time (30 fs) and transit time (80 fs) were extracted from the dependence of the intrinsic delay time on the collector spacer thickness.

In Chapter 5, to increase the oscillation frequency, I proposed combining the reduction in the total delay time with a thin barrier and well, as discussed in Chapter 3, along with the optimum spacer and good values for the transit time and extrinsic delay, as discussed in Chapter 4. To further increase the oscillation frequency, I proposed a decrease in the extrinsic delay time with a decrease in the series resistance caused by the bulk and spread resistances of the RTDs, the optimization of the antenna length, a decrease in the antenna loss by removing the InGaAs under the air bridge, an increase in the antenna electrode thickness, and a change in the metal from gold to silver. The theoretical calculation of the oscillation characteristics with these comprehensive improvements was reported. It was shown theoretically that an oscillation frequency of over 2 THz and an output power of >1 mW at 0.5 THz are possible by combining a thin well and optimum spacer, reducing the extrinsic delay time, using an optimum antenna length, and reducing the antenna loss by improving the antenna structure. The oscillation frequency achieved in the experiment was 1.86 THz for well and spacer thicknesses of 2.5 and 12 nm, respectively, with an antenna length of 12 μm without the InGaAs under the air bridge. In this structure, the total delay time was 90 fs, which consisted of the extrinsic delay time (80 fs) estimated from the parasitic elements and the intrinsic delay time (35 fs).

Future prospects and the preliminary works are summarized in Fig 6.1. A fundamental oscillation frequency of >2 THz with an output power of >1 μW is achievable. Therefore, some spectroscopic applications are expected, including inspections for forbidden materials such as drugs and explosives. A value of >1 mW is expected under the 0.5-THz range, which will also make imaging applications possible. In the ultra-high speed wireless communication field, a transmission capability of greater than 1 Tbps will be possible, with frequency division duplex ~50 Gbps/ch with improvement of modulation signal circuit in the RTD in the near field at a frequency range below 2 THz or short range communication under 1 THz.

In this research, RTD terahertz oscillators are expected to be used as compact sources for many terahertz applications.

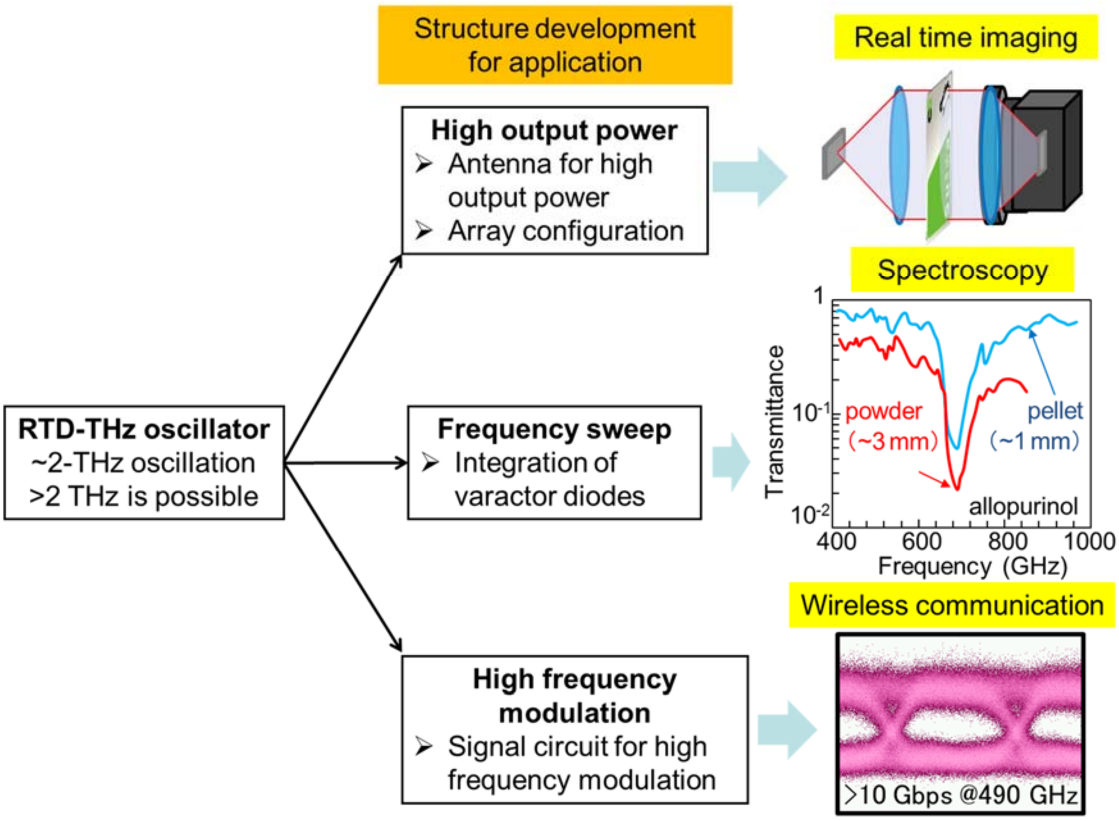

Fig. 6.1 Future prospects of RTD-THz oscillators.

Acknowledgements

I would like to thank Professor Masahiro Asada. I have been honored to conduct the difficult but fulfilling research for my doctoral course in the Asada laboratory under his competent direction.

I am also grateful to Professors Fumio Koyama and Hiroyuki Uenohara at the Tokyo Institute of Technology, Professor Takashi Uchida at the National Defense Academy, and Associate Professors Masahiro Watanabe and Tomoyuki Miyamoto at the Tokyo Institute of Technology for their keen examinations and helpful comments in this doctoral research. In particular, I would like to again thank Professor Uchida for the invitation to a research field that has changed my life.

I appreciate the assistance provided by Professors Shigehisa Arai and Yasuyuki Miyamoto, Associate Professor Nobuhiko Nishiyama, and Assistant Professors Toru Kanazawa and Tomohiro Amemiya at the Tokyo Institute of Technology. I have been honored to be associated with their influential and friendly research group.

I am most grateful to Associate Professor Safumi Suzuki. When I had research problems, especially tough experiments, Safumi always discussed them and helped me. My research life mainly consists of his accurate leading and his friendly support. And congratulations on your wedding and best of luck in married life!

I am thankful to Dr. Michael Feiginov, Dr. Withawat Withayachumnankul, Dr. Atsushi Teranishi, and Masato Shiraishi, Kaoru Shizuno, Hirotaka Shibayama, Kaname Ishigaki, Kaoru Maruyama, Junnoshin Sezaki, Shinji Kaburaki, Kengo Okada, Yu Miyajima, Riku Sogabe, Hiroki Mizumoto, Takuro Nukariya, Yu Ikeda, Kyo Mizoguchi, Takeru Maekawa, Seiichiro Kitagawa, Naoto Oshima, Kota Ogino, Tomohiro Fukuma, Daisuke Horikawa, Kazuhide Hashimoto, Ong Raphael, Satoshi Shibuya, Shintaro Fukuma, and Isobe Yuki at the Asada and Suzuki laboratories. I would especially like to thank Takeru Maekawa for the discussion of the antenna structure improvement in this thesis. The uncountable difficult but joyful memories, events, and dramas that I experienced in the Asada and Suzuki laboratories are my supreme treasures in my life.

I would like to express my gratitude to all of the members of the Arai-Nishiyama, Miyamoto, Watanabe, and Suzuki laboratories. I will long remember the difficult but enjoyable experiments in Cho-Ele. I would like to again thank those members who shared the EB machine time and assisted me with various problems such as a water leak.

I am thankful to Shigeo Tamura of the technical staff for the continuous maintenance of various pieces of equipment at Cho-Ele. I thank Takeshi Yamaguchi and Shintaro Kawada of the nanotechnology platform for the valuable advice on the fabrication process. I was helped by Secretary Takada, Kasukawa, Yashima, and Suzuki during my laboratory work, who contributed cheerful exchanges and tasty sweets.

I am also grateful to Dr. Inoue, Dr. Hachinohe, Dr. Kubo, Dr. Kudo, and Dr. Hasegawa for supporting and encouraging me to accomplish this difficult but interesting mission.

I wish to thank my family and friends for their unchanged kindness when I went back to my home town.

Lastly, I would like to say thank you to my wife, Mie, for supporting my challenge without complaints. I would also like to say thank you to my daughter, Mei, who helped me with her delightful smile every morning.

References

Chapter 1

[1.1] P. H. Siegel, "Terahertz Technology," *IEEE Microwave Theory and Technique*, vol. 50, pp. 910-928, 2002.

[1.2] M. Tonouchi, "Cutting-edge terahertz technology," *Nat. Photonics*, vol. 1, pp. 97-105, 2007.

[1.3] T. Nagatsuma, "Teraherthz thechnologies: present and future," *IEICE Electron. Express*, Vol.8, no. 14, 1127-1142, 2011.

[1.4] T. Robin, C. Bouye, and J. Cochard, "Terahertz applications: trends and challenges," *Proc. of SPIE*, vol. 8985, 898512, 2014.

[1.5] T. Hochrein, "Markets, Availability, Notice, and Technical Performance of Terahertz Systems: Historic Development, Present, and Trend," *J. Infrared Milli. Terahz. Waves*, vol. 36, 235-254, 2015.

[1.6] T. S. Hartwick, D. T. Hodges, D. H. Barker, and F. B. Foote, ”Far infrared imagery," *Appl. Opt.*, vol. 15, no. 8, 1919, 1976.

[1.7] M. V. Exter and D. Grischkowsky, "Carrier dynamics of electrons and holes in moderately doped silicon," *Phys. Review B*, vol. 41, no. 17, 12140-12149, 1990.

[1.8] B. B. Hu and M. C. Nuss, "Imaging with terahertz wave," *Opt. Lett.*, vol. 20, no. 16, 1716, 1995.

[1.9] A. G. Markelz, A. Roitberg, E. J. Heilweil, "Pulsed terahertz spectroscopy of DNA, bovine serum albumin and collagen between 0.1 and 2.0 THz," *Chem. Phys. Lett.*, vol. 320, 42-48, 2000.

[1.10] M. Hangyo, T. Nagashima, and S. Nashima, "Spectroscopy by pulsed terahertz radiation," *Meas. Sci. Technol*. 13, pp.1727–1738, 2002.

[1.11] B. Ferguson and X. C. Zhang, "Materials for terahertz science and technology," *Nature materials*, vol. 1, 26, 2002.

[1.12] M. C. Beard, G. M. Turner, and C. A. Schmuttenmaer, "Terahertz Spectroscopy," *J. Phys. Chem. B*, vol. 106, 7146-7159, 2002.

[1.13] M. Nagel, P. H. Bolivar, M. Brucherseifer, and H. Kurz, “Integrated THz technology for label-free genetic diagnostics,” *Appl. Phys. Lett*., vol. 80, pp. 154–156, 2002.

[1.14] R. M. Woodward, B. E. Cole, V. P. Wallace, R. J. Pye, D.D Arnone, E. H. Linfield and M. Pepper, “Terahertz pulse imaging in reflection geometry of human skin cancer and skin tissue,” *Phys. Med. Biol*., vol. 47, pp. 3853–3863, 2002.

[1.15] D. Clery, “Terahertz on a Chip,” *Science*, vol. 297, 763, 2002.

[1.16] R. M. Woodward, V. P. Wallace, R. J. Pye, B. E. Cole, D.D Arnone, E. H. Linfield and M. Pepper, “Terahertz Pulse Imaging of ex vivo Basal Cell Carcinoma,” *J. Investigative Dermatology*, vol. 120, no. 1, 2003.

[1.17] C. J. Strachan, T. Rades, D. A. Newnham, K. C. Gordon, M. Pepper, and P. F. Taday, “Using terahertz pulsed spectroscopy to study crystallinity of pharmaceutical materials,” *Chem. Phys. Lett.*, vol. 390, 20-24, 2004.

[1.18] A. Dobroiu, M. Yamashita, Y. N. Oshima, Y. Morita, C. Otani, and K. Kawase, “Terahertz imaging system based on a backward-wave oscillator,” *Appl. Opt.*, vol. 43, no. 30, 5637, 2004.

[1.19] K. Kawase, “Terahertz Imaging,” *Optics & Photonics News*, vol. 35, 2004.

[1.20] D. Zimdars and J.S. White, “Terahertz reflection imaging for package and personnel inspection,” *Proc. of SPIE*, vol. 5411, 78, 2004.

[1.21] K. Yamamoto, M. Yamaguchi, F. Miyamaru, M. Tani, M. Hangyo, T. Ikeda, A. Matsushita, K. Koide, M. Tatsuno, and Y. Minami, “Noninvasive Inspection of C-4 Exploration in Mails by Terahertz Time-Domain Spectroscopy,” *Jpn. J. Appl. Phys*., vol. 43, no. 3B, pp. L414-L417, 2004.

[1.22] M. Yamashita, K. Kawase, C. Otani, T. Kiwa and M. Tonouchi, “Imaging of large-scale integrated circuits using laser terahertz emission microscopy,” *Opt. Express*, vol. 13, pp. 115–120, 2005.

[1.23] K. Kawase, Y. Ogawa, H. Minamide, and H. Ito, “Terahertz parametric sources and imaging applications,” *Semicond. Sci. Technol*., vol. 20, pp. S258-S265, 2005.

[1.24] J. F. Federici, B. Schulkin, F. Huang, D. Gary, R. Barat, F. Oliveira, and D. Zimdars, “THz imaging and sensing for security applications - explosives, weapons and drugs,” *Semicond. Sci. Technol*., vol. 20, pp. S266-S280, 2005.

[1.25] B. Fischer, M. Hoffmann, H. Helm, G. Modjesch, and P. H. Jepsen, “Chemical recognition in terahertz time-domain spectroscopy and imaging,” *Semicond. Sci. Technol.*, vol. 20, S246-S253, 2005.

[1.26] A. Dobroiu, C. Otani and K. Kawase, “Terahertz-wave sources and imaging applications,” *Meas. Sci. Technol.*, vol. 17, R161-174, 2006.

[1.27] H. B. Liu and Y. Chen, “Detection and identification of explosive RDX by THz diffuse reflection spectroscopy,” *Opt. Express*, vol. 14, no. 1, 415, 2006.

[1.28] A. W. M. Lee, Q. Qin, S. Kumar, B. S. Williams, Q. Hu, and J. L. Reno, “Real-time terahertz imaging over a standoff distance (> 25 meters),” *Appl. Phys. Lett.*, vol. 89, 141125, 2006.

[1.29] W. L. Chan, J. Deibel and D. M. Mittleman, “Imaging with terahertz radiation,” *Rep. Prog. Phys.*, vol. 70, pp. 1325–1379, 2007.

[1.30] H. B Liu, H. Zhong, N. Karpowicz, Y. Chen, and X. C. Zhang, “Terahertz Spectroscopy and Imaging for Defense and Security Applications,” *Proc. IEEE*, vol. 95, issue. 8, 1514, 2007.

[1.31] B. C. Baker, T. Lo, W. R. Tribe, B. E. Cole, M. R. Hogbin, and M. C. Kemp, “Detection of Concealed Explosives at a Distance Using Terahertz Technology,” *Proc. IEEE*, vol. 95, issue. 8, 1559, 2007.

[1.32] D. M. Sheen, D. L. McMakin, and T. E. Hall, “Speckle in active millimeter-wave and terahertz imaging and spectroscopy,” *Proc. of SPIE*, vol. 6548, 654809, 2007.

[1.33] D. F. Plusquellic, K. Siegrist, E. J. Heilweil, and O. Esenturk, “Application of Terahertz Spectroscopy in Biosystems,” *Chem. Phys. Chem.*, vol. 8 2412-2431, 2007.

[1.34] J. A. Zeitler, P. F. Taday, D. A. Newnham, M. Pepper, K. C. Gordon and T. Rades, “Terahertz pulsed spectroscopy and imaging in the pharmaceutical setting – a review,” *J. Pharmacy and Pharmacology*, vol. 69, 209-223, 2007.

[1.35] H. Yoneyama, M. Yamashita, S. Kasai, K. Kawase, H. Ito, and T. Ouchi, “Membrane device for holding biomolecule samples for terahertz spectroscopy,” *Opt. Communication.*, vol. 281, 1909-1913, 2008.

[1.36] H. Yoneyama, M. Yamashita, S. Kasai, K. Kawase, R. Ueno, H. Ito, and T. Ouchi, “Terahertz spectroscopy of native-conformation and thermally denatured bovine serum albumin (BSA)," *Phys. Med. Biol.*, vol. 53, 3543-3549, 2008.

[1.37] A. G. Davies, A. D. Burnett, W. Fan, E. H. Linfield, and J. E. Cunningham, "Terahertz spectroscopy of explosives and drugs," *Materials today*, vol. 11, no. 3, 18, 2009.

[1.38] N. Shimizu, H. J. Song, Y. Kado, T. Furuta, A. Wakatsuki, and Y. Muramoto, "Gas Detection Using Terahertz Waves," *NTT Technical Review*, vol. 7, no. 3, 2009.

[1.39] H. Hoshina, Y. S. Sasaki, A. Hayashi, C. Otani, and K. Kawase, "Noninvasive Mail Inspection System with Terahertz Radiation," *Appl. Spectroscopy*, vol. 63, no. 1, 81, 2009.

[1.40] C. Jansen, S. Wietzke, O. Peters, M. Scheller, N. Vieweg, M. Salhi, N. Krumbholz, C. Jordens, T. Hochrein, and M. Koch, "Terahertz imaging: application and perspective," *Appl. Opt.*, vol. 49, no. 19, E48, 2010.

[1.41] F. Friederich, W. V. Spiegel, M. Bauer, F. Meng, M. D. Thomson, S. Boppel, A. Lisauskas, B. Hils, V. Krozer, A. Keil, T. Loffler, R. Henneberger, A. K Huhm, G. Spickermann, P. H. Boivar, and H. G. Roskos, "THz Active Imaging Systems With Real-Time Capabilities," *IEEE Trans. Terahertz Science and Technol.*, vol. 1, no. 1, 183, 2011.

[1.42] M. C. Kemp, "Explosive Detection by Terahertz Spectroscopy-A Bridge Too Far?," *IEEE Trans. Terahertz Science and Technol.*, vol. 1, no. 1, 282, 2011.

[1.43] Y. C. Shen, "Terahertz pulsed spectroscopy and imaging for pharmaceutical applications: A review," *Int. J. Pharmaceutics*, vol. 417, 48-60, 2011.

[1.44] N. Palka, "THz Reflection Spectroscopy of Explosives Measured by Time Domain Spectroscopy," *ACTA Physica Polonica A*, vol. 120, no. 4, 713, 2011.

[1.45] C. Otani, in *New terahertz industry*, supervised M. Tonouchi (CMC publishing) pp. 149-155, in Japanease, 2011.

[1.46] P. Tewari, C. P. Kealey, D. B. Bennett, N. Bajwa, K. S. Barnett, R. S. Singh, M. O. Culjat, A. Stojadinovic, W. S. Grundfest, and Z. D. Taylor, "In vivo terahertz imaging of rat skin burns," *J. Biomedical Opt.*, vol. 17 No. 4, 040503, 2012.

[1.47] A. I. McIntosh, B. Yang, S. M. Goldup, M. Watkinson, and R. S. Donnan, "Terahertz spectroscopy: a powerful new tool for the chemical sciences?," *Chem. Soc. Rev.*, vol. 41, 2072-2082, 2012.

[1.48] J. S. Caygill, F. Davis, S. P. J. Higson, "Current trends in explosive detection techniques," *Talanta*, vol. 88, 14-29, 2012.

[1.49] G. J. Kim, J. I. Kim, S. G. Jeon, J. Kim, K. K. Park, C. H. Oh, “Enhanced Continuous-Wave Terahertz Imaging with a Horn Antenna for Food Inspection,” *J. Infrared Milli. Terahz. Waves*, vol. 33, 657-664, 2012.

[1.50] H. Sherry, J. Grzyb, Y. Zhao, R. A. Hadi, A. Cathelin, A. Kaiser, and U. Pfeiffer, “A 1kPixel CMOS Camera Chip for 25 fps Real-Time Terahertz Imaging Applications,” *Int. Solid-State Circuits Conf.*, 15.1, San Francisco, USA, 2012. .

[1.51] W. Zouaghi, M. D. Thomson, K. Rabia, R. Hahn, V. Blank, and H. G. Roskos, “Broadband terahertz spectroscopy: principles, fundamental research and potential for industrial applications,” *Eur. J. Phys.*, vol. 34, S179-S199, 2013.

[1.52] T. Ouchi, K. Kajiki, T. Koizumi, T. Itsuji, Y. Koyama, R. Sekiguchi, O. Kubota, and K. Kawase, “Terahertz Imaging System for Medical Applications and Related High Efficiency Terahertz Devices,” *J. Infrared Milli. Terahz. Waves*, vol. 35, 118-130, 2014.

[1.53] B. Clough and X. C. Zhang, “Toward remote sensing with broadband terahertz waves,” *Front. Optoelectron.*, vol. 7, no. 2, 199-219, 2014.

[1.54] A. Lisaukas, M. Bauer, S. Boppel, M. Mundt, B. Khamaisi, E. Socher, R. Venkevicius, L. Minkevicius, I. Kasalynas, D. Seliuta, G. Valusis, V. Krozer, and H. G. Roskos, “Exploration of Terahertz Imaging with Sillicon MOSFETs,” *J. Infrared Milli. Terahz. Waves*, vol. 35, issue 1, pp 63-80, 2014.

[1.55] U. R. Pfeiffer. Y. Zhao, J. Grzyb, R. A. Hadi, N. Sarmah. W. Forster, H. Rucker, and B. Heinemann, “A 0.53 THz Reconfigurable Source Array with up to 1mW Radiated Power for Terahertz Imaging Applications in 0.13μm SiGe BiCMOS,” *Int. Solid-State Circuits Conf.*, 14.5, San Francisco, USA, 2014.

[1.56] J. P. Guillet, B. Recur, L. Frederique, B. Bounsquet, L. Canioni, I. M. Honninger, P. Desbarats, and P. Mounaix, “Review of Terahertz Tomography Techniques” *J. Infrared Milli. Terahz. Waves*, vol. 35, issue 1, pp 382-411, 2014.

[1.57] A. Yamaguchi, “Development of Terahertz Imaging System” *PIONEER R&D*, pp. 1-7, 2014, in Japanese.

[1.58] S. Fan, R. Q. T. Notake, K. Nawata, T. Matsukawa, Y. Takida, and H. Minamide, “Real-time terahertz wave imaging by nonlinear optical frequency up-conversion in a 4-dimethylamino-N’-methl-4’-stilbazolium tosylate crystal,” *Appl. Phys. Lett.*, vol. 104,

101106, 2014.

[1.59] K. Ohata, K. Maruhashi, M. Ito, S. Kishimoto, K. Ikuina, T. Hashiguchi, K. Ikeda, and N. Takahashi : "1.25 Gbps wireless Gigabit ethernet link at 60 GHz-band," *Radio Frequency Integrated Circuits (RFIC) Symposium*, TU4D-6, pp. 509-512, 2003.

[1.60] A. Hirata, T. Kosugi, H. Takahashi, R. Yamaguchi, F. Nakajima, T. Furuta, H. Ito, H. Sugahara, Y. Sato, T. Nagatsuma, "120-GHz-band millimeter-wave photonic wireless link for 10-Gb/s data transmission," *IEEE Trans. Microwave Theory Technol*. vol. 54, pp. 1937–1944, 2006.

[1.61] L. Atzori, A. Iera, G. Morabito, "The Internet Of Things: A survey," *Computer Networks* Vol. 54, 2787-2805, 2010.

[1.62] J. Federici and L Moeller, "Review of terahertz and subterahertz wireless communications," *J. Appl. Phys.*, vol. 107, 111101, 2010.

[1.63] H.-J. Song and T. Nagatsuma, "Present and Future of Terahertz Communications," *IEEE Trans. On Terahertz Science and Technol.*, vol. 1, no. 1, 256, 2011.

[1.64] I. Kallfass, J. Antes, T. Schneider, F. Kurz, D. L.-Diaz, S. Diebold, H. Massler, A. Leuther, and A. Tessmann, "All Active MMIC-Based Wireless Communication at 220 GHz," *IEEE Trans. On Terahertz Science and Technol.*, vol. 1, no. 2, 477, 2011.

[1.65] T. K. Ostmann and T. Nagatsuma, "A Review on Terahertz Communication Research," *J. Infrared Milli. Terahz. Waves*, vol. 32, pp 143-171, 2011.

[1.66] H.-J. Song, K. Ajito, Y. Muramoto, A. Wakatsuki, T. Nagatsuma and N. Kukutsu, "24 Gbit/s data transmission in 300 GHz band for future terahertz communications," *Electronics Letters*, vol. 48 No. 15, 2012.

[1.67] S. Koening, D. L. Diaz, J. Antes, F. Boes, R. Henneberger, A. Leuther, A. Tessman, R. Schmogrow, D. Hillerkuss, R. Palmer, T. Zwick, C. Koos, W. Freude, O. Ambacher, J. Leuthold, and I. Kakkfass, "Wireless sub-THz communication system with high data rate," *Nature Photon.*, 275, 2013.

[1.68] T. Nagatsuma, S. Horiguchi, Y. Minamikata, Y. Yoshimizu, S. Hisatake, S. Kuwano, N. Yoshimoto, J. Terada, and H. Takahashi, "Terahertz wireless communications based on photonics technologies," *Opt. Express*, vol. 21, no. 20, 23736, 2013.

[1.69] I. F. Akyildiz, J. M. Jornet, and C. Han, "Terahertz band: Next frontier for wireless communications," *Physical Communication*, vol. 12, 16-32, 2014.

[1.70] M. S. Tobin, "A review of Optically Pumped NMMW Lasers," *Proc. IEEE*, vol. 73, issue 1, 61, 1985.

[1.71] G. P. Williams, "FAR-IR/THz radiation from the Jefferson Laboratory, energy recovered linac, free electron laser," *Rev. Sci. Instrum.*, vol. 73, no. 3, 2002.

[1.72] T. Idehara, H Tsutiya, O. Watanabe, La. Angusu, and S. Mitsudo,"The first experiment of a THz gyrotron with a pulse magnet," *J. Infrared Milli. Waves*, vol. 27, issue 3, pp. 319-331, 2006.

[1.73] V. Bratman, M. Glyavin, T. Idehara, Y. Kalynov, A. Luchinin, V. Manuilov, S. Mitsudo, I. Ogawa, T. Saito, Y. Tatematsu, and V. Zapevalov "Review of Subterahertz and Terahertz Gyrodevices at IAP RAS and FIR FU," *IEEE Trans. Plasma Science*, vol. 37 No. 1, 36, 2009.

[1.74] T. Saito, S. Ogasawara, N. Yamada, S. Ikeuchi, Y. Tatematsu, R. Ikeda, I. Ogawa, and V. N. Manuilov, "New Power Records of Sub-Terahertz Gyrotron with Second-Harmonic Oscillation," *Plasma and Fusion Research*, vol. 7, 1206003, 2012.

[1.75] K. Suizu, K. Miyamoto, T. Yamashita, and H. Ito, "High-power terahertz-wave generation using DAST crystal and detection using mid-infrared powermeter," *Opt. Lett.*, vol. 32, no. 19, 2885, 2007.

[1.76] S. Hayashi, K. Nawata, H. Sakai, T. Taira, H. Minamide, and K. Kawase, "High-power, single-longitudinal-mode terahertz-wave generation pumped by a microchip Nd:YAG laser," *Opt. Express*, vol. 20, no. 3, 2881, 2012.

[1.77] K. Takeya, K. Suizu, H. Sai, T. Ouchi, and K. Kawase, "Wide Spectrum Terahertz-Wave Generation From Nonlinear Waveguide," *IEEE J. Sel. Topi. Quant. Electron.*, vol. 19, no. 1, 8500212, 2013.

[1.78] S. Hayashi, K. Nawata, T. Taira, J. Shikata, K. Kawase, and H. Minamide, "Ultrabright continuously tunable terahertz-wave generation at room temperature," *Scientific Report*, vol. 4, 5045, 2014.

[1.79] T. Ishibashi, T. Furuta, H. Fushimi, S. Kodama, H. Ito, T. Nagatsuma, N. Shimizu, and Y. Miyamoto, "InP/InGaAs Uni-Traveling-Carrier Photodiodes," *IEICE Trans. Electron.*, vol. E83-C, no. 6, 2000.

[1.80] H. Ito, F. Nakajima, T. Furuta, and T. Ishibashi, “Continuous THz-wave generation using antenna-integrated uni-traveling-carrier photodiodes,” *Semicon. Sci. Technol.*, vol. 20, S191-S198, 2005.

[1.81] H.-J. Song, K.-H. Oh, N. Shimizu, N. Kukutsu, and Y. Kado, “Generation of frequency-modulated sub-terahertz signal using microwave photonic technique,” *Opt. Express*, vol. 18, no. 15, 15936, 2010.

[1.82] H. Ito, T. Yshimitsu, H. Yamamoto , and T. Ishibashi, “Broadband photonic terahertz-wave emitter integrating uni-traveling-carrier photodiode and self-compementary planar antenna,” *Opt. Engineering*, vol. 53, no. 3, 031209, 2014.

[1.83] D. H. Auston, K. P. Chung, and P. R. Smith, "Picosecond photoconducting Hertzian dipoles," *Appl. Phys. Lett.*, vol.45, no. 3, 1984.

[1.84] A. Bonvalet, M. Joffre, J. Martin, and A. Migus, “Generation of ultrabroadband femtosecond pulses in the mid-infrared by optical rectification of 15 fs light pulses at 100 MHz repetition rate,” *Appl. Phys. Lett.*, vol. 67, no. 20, 13, 1995.

[1.85] M. Tani, S. Matusura, K. Sakai, and S. Nakashima, “Emission characteristics of photoconductive antennas based on low-temperature-grown GaAs and semi-insulating GaAs,” *Appl. Opt.*, vol. 36, no. 30, 7853, 1997.

[1.86] A. Dreyhaupt, S. Winnerl, T. Dekorsy, and M. Helm, “High-intensity terahertz radiation from a microstructured large-area photoconductor,” *Appl. Phys. Lett.*, vol. 86, 121114, 2005.

[1.87] H. Tanoto, J. H. Teng, Q. Y. Wu, M. Sun, Z. N. Chen, S. A. Maier, B. Wang, C.C. Chum, G. Y. Si, A. J. Danner and S. J. Chua, “Greatly enhanced continuous-wave terahertz emission by nano-electrodes in a photoconductive photomixier,” *Nature Photon.*, vol. 6, 121, 2012.

[1.88] H. Eisele, “State of the art and future of electronic sources at terahertz frequencies,” *Electron. Lett.*, vol. 46, issue 26, S8-S11, 2010.

[1.89] A. Maestrini, J. S. Ward, J. J. Gill, C. Lee, B. Thomas, R. H. Lin, G. Chattopadhyay, and I. Mehdi, “A Frequency –Multiplied Source With More Than 1 mW of Power Across the 840-900-GHz band,” *IEEE Trans. Micron. Theory and Techniques*, vol. 58, no. 7, 2010.

[1.90] J. L. Hesler and T. Crowe, “High-power solid-state terahertz sources,” *SPIE Newsroom*, DOI: 10.1117/2.1201507.005859.

[1.91] S. Komiyama, "Far-Infrared Emission from Population-Inverted Hot-Carrier System in p-Ge," *Phys. Rev. Lett.*, vol. 48, pp.271-pp.274, 1982.

[1.92] *R. F.* Kazarinov and *R. A. Suris*, “Possibility of the amplification of electromagnetic waves in a semiconductor with a superlattice,” *Fiz*. *Tekh*. *Poluprovodn*., vol. 5, pp. *797*–800, *1971*.

[1.93] J. Faist, F. Capasso, D. L. Sivco, C. Sirtori, A. L. Hutchinson, and A. Y. Cho, "Quantum Cascade Laser," *Science*, vol. 264, pp.553-556, 1994.

[1.94] C. Walther, M. Fischer, G. Scalari, R. Terazzi, N. Hoyler, and J. Faist, “Quantum cascade lasers operating from 1.2 to 1.6 THz,” *Appl. Phys. Lett.*, vol. 91, pp. 131122, 2007.

[1.95] B.S. Williams, "Terahertz quantum-cascade lasers," *Nature Photonics*, vol. 1, p. 517-525. 2007.

[1.96] S. Fathololoumi, E. Dupont, C.W.I. Chan, Z.R. Wasilewski, S.R. Laframboise, D. Ban, A. Matyas, C. Jirauschek, Q. Hu, and H.C. Liu, “Terahertz quantum cascade lasers operating up to ~ 200 K with optimized oscillator strength and improved injection tunneling,” *Opt. Express*, vol. 20, no. 4, p. 3866, 2012.

[1.97] M. Razeghi, Q. Y. Lu, N. Bandyopadhyay, and S. Slivken, “Recent development of high power, widely tunable THz quantum cascade laser sources based on difference-frequency generation,”*Proc. of SPIE*, vol. 9585, 958502-1, 2015.

[1.98] L. Ozyuzer, A. E. Koshelev, C. Kurter, N. Gopalsami, Q. Li, M. Tachiki, K. Kadowaki, T. Yamamoto, H. Minami, H. Yamaguchi, T. Tachiki, K. E. Gray, W.-K. Kwok, U. Welp, “Emission of Coherent THz Radiation from Superconductors,” *Science*, vol. 318, 23, 2007.

[1.99] T. Kashiwagi, K. Sakamoto, H. Kubo, Y. Shibano, T. Enomoto, T. Kitamura, K. Asanuma, T. Yasui, C. Watanabe, K. Nakade, Y. Sawai, T. Katsuragawa, M. Tsujimoto, R. Yoshizaki T. Yamamoto, H. Minami, R. A. Klemm, and K. Kadowaki, “A high-T_c intrinsic Josephson junction emitter tunable from 0.5 to 2.4 terahertz,” *Appl. Phys. Lett.*, vol. 107, 082601, 2015.

[1.100] W. T. Read, "A Proposed High-Frequency, Negative-Resistance Diode," *Bell Syst. Tech. J.*, vol. 37, pp. 401- 446, 1958.

[1.101] J. Nishizawa and Y. Watanabe, "High Frequency Properties of the Avalanching Negative

Resistance diode," *Sci. Rep. Res. Inst. Tohoku. Univ. B-(Comm)*, vol. 10, no. 2, pp.91-108, Sendai, Japan, 1958.

[1.102] M. Ino, T. Ishibashi, and M. Ohmori, "C. W. Oscillation with p^+-p-n^+ Silicon IMPATT Diodes in 200GHz and 300GHz Bands," *Electron. Lett.,* vol. 12, no. 6, pp.148-149, 1976.

[1.103] T. Ishibashi, M. Ino, T. Makimura and M. Ohmori, "Liquid-Nitrogen-Cooled Submillimeter-wave Silicon IMPATT Diodes," *Electron. Lett.*, vol. 13, no. 10, pp.299- 300, 1977.

[1.104] H. Eisele, A. Rydberg, G. I. Haddad, “Recent advances in the performance of InP Gunn Devices and GaAs TUNNETT diodes for the 100-300-GHz Frequency range and above,” *IEEE Trans. Microwave Theory and Techniques*, vol. 48, no. 4, 2000.

[1.105] J. Nishizawa, T. Kurabayashi, P. Plotka, and H. Makabe, “Development of TUNNETT Diode as Terahertz Device and Its Applications,” *Annual Device Research Conf.*, V.A-3, Pennsylvania, USA, 2006.

[1.106] J. B. Gunn, "Microwave oscillations of current in III-V semiconductors," *Solid State Cummun*., vol. 1, pp. 88-91, 1963. .

[1.107] H. Eisele and R. Kamoua, "Submillimeter-wave InP Gunn devices," *Electron. Lett*., vol. 52, no. 10, pp. 2371 - 2378, 2004.

[1.108] Eisele, “480 GHz oscillator with an InP Gunn device” *Electron. Lett*., vol. 46, no. 6, p. 422, 2010.

[1.109] W. Knap, J. Lusakowski, T. parently, S. Bollaert, A. Cappy, V. V. Popov, M. S. Shur, “Terahertz emission by plasma waves in 60 nm gate high electron mobility transistors,” *Appl. Phys. Lett.*, vol. 84, no. 13, 2331 ,2004.

[1.110] N. Sekine and K. Hirakawa, “Dispersive Terahertz Gain of a Nonclassical Oscillator: Bloch Oscillation in Semiconductor Superlattices,” *Phys. Review Lett.*, vol. 94, no. 5, 057408, 2005.

[1.111] T. Otsuji, S.B. Tombet, A. Satou, M. Ryzhii, and V. Ryzhii, “Terahertz-Wave Generation Using Graphene: Toward New Types of Terahertz Lasers,” *IEEE J. Sel. Topics Quantum Electronics*, vol. 19, no. 1, 8400209, 2013.

[1.112] H. Kroemer, “Theory of a Wide-Gap Emitter for Transistors,” *Proc. IRE,* vol. 45, pp.1535, 1957.

[1.113] T. Ishibashi and Y. Yamauchi, “A Possible Near-Ballistic Collection in an AlGaAs/GaAs HBT with a Modified Collector Structure,” *IEEE Trans. Electron Devices*, vol. 35, no. 4, 1988.

[1.114] A. Fujihara, Y. Ikenaga, H. takahashi, M. Kawanaka and S. Tanaka, “High-Speed InP/InGaAs DHBT with Ballistic Collector Launcher Structure,” *Int. Electorn. Device Meeting*, 35.3.1, Washington, USA, 2001.

[1.115] M. Feng and W. Snodgrass, “InP Pseudormorphic Heterojunction Bipolar Transistor (PHBT) with f_t > 750GHz,” *Int. Conf. Indium Phosphide and Related Materials*, WeA3-1, Matsue, Japan, 2007. .

[1.116] M. Urteaga, R. Pierson, P. Rowell, V. Jain, E. Lobisser, and M.J.W. Rodwe1l, “130 nm InP DHBTs with f_t >0.52THz and f_{max} >1.1THz,” *Device Research Conference*, pp. 281-282, Santa Barbara, USA, 2011.

[1.117] S. Munkyo, M. Urteaga, J. Hacker, A. Young, Z. Griffith, V. Jain, R. Pierson, P. Rowell, A. Skalare, A. Peralta, R. Lin, D. Pukala, and M. Rodwell, “InP HBT IC Technology for Terahertz Frequencies: Fundamental Oscillators Up to 0.57 THz,” *IEEE Journal of Solid-State Circuits*, vol. 46, no. 10, pp. 2203-2214, 2011.

[1.118] T. Mimura, S. Hiyamizu, T. Fuji, and K. Nanbu, “A New Field-Effect Transistor with Selectevely Doped GaAs/n-$Al_xGa_{1-x}As$ Heterojunctions,” *Jpn. J. Appl. Phys.*, vol. 19, no. 5, pp. L225-L227, 1980.

[1.119] V. Radisic X. B. Mei, W. R. Deal, W. Yoshida, P. H. Liu, J. Uyeda, M. Barsky, L. Samoska, A. Fung, T. Gairer, and R. Lai, “Demonstration of Sub-Millimeter Wave Fundamental Oscillation Using 35-nm InP HEMT Technology,” *IEEE Microwave and Wireless Componets Lett.*, vol. 17, no. 3, 223, 2007.

[1.120] V. Radisic, L. Samoska, W. R. Deal, X.B. Mei, W. Yoshida, P.H. Liu, J. Uyeda, A. Fung, T. Gaier, and R. Lai, “A 330-GHz MMIC oscillator module,” *2008 IEEE MTT-S International Microwave Symposium Digest*, pp. 395-398, Atlanta, USA, 2008.

[1.121] X. B. Mei, V. Radisic, W. Deal, W. Yoshida, J. Lee, L. Dang, P. H. Liu, W. Liu, M. Lange, J. Zhou, J. Uyeda, K. Leong, and R. Lai, “Sub-50nm InGaAs/InAlAs/InP HEMT for sub-millimeter wave power amplifier applications,” *2010 22nd Int. Conf. on Indium Phosphide and Related Materials (IPRM)*, ThB2-2, Kanagawa, Japan, 2010.

[1.122] W. R. Deal, K. Leong, V. Radisic, S. Sarkozy, B. Gorospe, J. Lee, P. H. Liu, W. Yoshida, J. Zhou, M. Lange, R. Lai, and X. B. Mei, “Low Noise Amplification at 0.67 THz Using 30 nm InP HEMTs,” *Microwave and Wireless Components Letters*, vol. 21, no. 7, 2011.

[1.123] X. Mei, W. Yoshida, M. Lange, J. Lee, Z. Zhou, P.-H. Kiu, K. Leong, A. Zamora, J. Padilla, S. Sarkozy, R. Lai, and W. R. Deal, “First demonstration of Amplification at 1 THz Using 25-nm High Electron Mobility Transistor Process,” *IEEE Electron Device Lett.*, vol. 36, no. 4, 2011.

[1.124] A. Leuther, S. Koch, A. Tessmann, I. Kallfass, T. Merkle, H. Assler, R. Loesch, M. Schlechtweg, S. Saito, O. Ambacher, “20 nm Metamorphic HEMT with 660 GHz f_t,” *Int. Conf. Indium Phosphide and Related Materials*, Tu-4.2.2, Berlin, Germany, 2011.

[1.125] L. A. Samoska, “An Overview of Solid-State Integrated Circuit Amplifiers in the Submillimeter-Wave and THz Regime,” *IEEE Trans. THz Sci. Technol.*, vol. 1, no. 1, 9, 2011.

[1.126] W. Deal, X. B. Mei, K. M. K. H. Leong, V. Radisic, S. Sarkozy, R. Lai, “THz Monolithic Integrated Circuits Using InP High Electron Mobility Transistors,” *IEEE Trans. THz Sci. Technol.*, vol. 1, no. 1, 25, 2011.

[1.127] X. Mei, W. Yoshida, M. Lange, J. Lee, J. Zhou, P.-H. Kiu, K. Leong, A. Zamora, J. Padilla, S. Sarkozy, R. Lai, and W. R. Deal, “First demonstration of Amplification at 1 THz Using 25-nm InP High Electron Mobility Transistor Process,” *IEEE Electron Device Letters*, vol. 36, no. 4, pp. 327-329, 2015.

[1.128] R. L. Johnston, B. C. De Loach, Jr., and B. G. Cohen, "A Silicon Diode Microwave Oscillator," *Bell Syst. Tech. J.*, vol.44, pp. 369- 372, 1965.

[1.129] E. Seok, C. Cao, D. Shim, D. J. Arenas, D. B. Tanner, C.-M. Hung, and K.K. O, “A 410 GHz CMOS Push-Push Oscillator with an On-Chip Patch Antenna,” *Int. Solid-State Circuits Conf.*, 26. 1, San Francisco, USA, 2008.

[1.130] Omeed Momeni, and E. Afshari, “High Power Terahertz and Millimeter-Wave Oscillator Design: A Systematic Approach” *IEEE J. solid-state circuits*, vol. 46, no. 3, pp. 583-597 2011.

[1.131] K. Sengupta and A. Hajimiri, “A 0.28 THz Power-Generation and Beam-Steering Array in CMOS Based on Distributed Active Radiators,” *IEEE J. Solid-State Circuits*, vol. 47, no.

12, 2012.

[1.132] W. Steyaert and Patrick Reynaert, “A 0.54 THz Signal Generation in 40 nm Bulk CMOS With 22 GHz Tuning Rage and Integrated Planar Antenna,” *IEEE J. Solid-State Circuits*, vol. 49, no. 7, 1617, 2014.

[1.133] U. R. Pfeiffer, Y. Zhao, J. Grzyb, R. A. Hadi, N. Sarmah, W. Forster, H. Rucker, and B. Heinemann, “A 0.53 THz Reconfigurable Source Array with up to 1mW Radiated Power for Terahertz Imaging Application in 0.13 μm SiGe BiCMOS,” *Int. Solid-State Circuits Conf.*, 14.5, San Francisco, USA, 2014.

[1.134] R. Tsu and L. Esaki, "Tunneling in a finite superlattice," *Appl. Phys. Lett.*, vol. 22, 1973.

[1.135] L. L. Chang, L. Esaki, and R. Tsu, "Resonant tunneling in semiconductor double barriers," *Appl. Phys. Lett.*, vol. 24, 1974. .

[1.136] T. C. L. G. Sollner, W. D. Goodhue, P. E. Tannenwald, C. D. Parker, and D. D. Peck, "Resonant tunneling through quantum wells at frequencies up to 2.5 THz," *Appl. Phys. Lett.*, vol. 43, no. 6, 1983.

[1.137] T. C. L. G. Sollner, P. E. Tannenwald, D. D. Peck, and W. D. Goodhue, "Quantum well oscillators," *Appl. Phys. Lett*., vol. 45, no. 12, 1984.

[1.138] T. J. Shewchuk, J. M. Gering, P. C. Chapin, P. D. Coleman, W. Kopp, C. K. Peng, and H. Morkoc, "Stable and unstable current-voltage measurements of a resonant tunneling heterostructure oscillator," *Appl. Phys. Lett.*, vol. 47, no. 9, 1985.

[1.139] T. J. Shewchuk, P. C. Chapin, P. D. Coleman, W. Kopp, R. Fischer, and H. Morkoc, "Resonant tunneling oscillations in a GaAs-$Al_xGa_{1-x}As$ heterostructure at room temperature," *Appl. Phys. Lett.*, vol. 46, no. 5, 1985.

[1.140] M. Tsuchiya, H. Sakaki, and J. Yoshino, "Room Temperature Observation of Differential Negative Resistance in an AlAs/GaAs/AlAs Resonant tunneling Diode," *Jpn. J. Appl. Phys.*, vol. 24, no. 6, pp. L466-L468, 1985.

[1.141] E. R. Brown, T. C. L. G. Sollner, W. D. Goodhue, and C. D. Parker, "Millimeter-band oscillations based on resonant tunneling in a double-barrier diode at room temperature," *Appl. Phys. Lett.*, vol. 50, no. 2, 1987.

[1.142] J. F. Whitaker, G. A. Mourou, T. C. L. G. Sollner, and W. D. Goodhue, "Picosecond switching time measurement of a resonant tunneling diode," *Appl. Phys. Lett.*, Vol. 53, no.

5, 1988.

[1.143] E. R. Brown, W. D. Goodhue, and T. C. L. G. Sollner, "Fundamental oscillations up to 200 GHz in resonant tunneling diodes and new estimates of their maximum oscillation frequency from stationary-state tunneling theory," *J. Appl. Phys.*, vol. 64, No.3, 1988.

[1.144] A. Takeuchi, T. Inata, S. Muto, and E. Miyauchi, "Picosecond Characterization of InGaAs/InAlAs Resonant Tunneling Barrier Diode by Electro-Optic Sampling," *Jpn. J. Appl. Phys.*, vol. 28, no. 5, pp. L750- L753, 1989.

[1.145] E. R. Brown, T. C. L. G. Sollner, C. D. Parker, W. D. Goodhue, and C. L. Chen, "Oscillations up to 420GHz in GaAs/AlAs resonant tunneling diodes," *Appl. Phys. Lett.,* vol. 55, no. 17, 1989.

[1.146] J. R. Söderström, E. R. Brown, C. D. Parker, L. J. Mahoney, J. Y. Yao, T. G. Andersson, and T. C. McGill, "Growth and characterization of high current density, high-speed InAs/AlSb resonant tunneling diodes," *Appl. Phys. Lett.*, vol. 58, no. 3, pp.275- 277, 1991.

[1.147] E. R. Brown, J. R. Söderström, C. D. Parker, L. J. Mahoney, K. M. Molvar, and T. C. McGill, "Oscillations up to 712GHz in InAs/AlSb resonant-tunneling diodes," *Appl. Phys. Lett.*, vol. 58, no. 20, pp.2291- 2293, 1991.

[1.148] N. Shimizu, T. Nagatsuma, M. Shinagawa, and T. Waho, "Picosecond-Switching Time of $In_{0.53}Ga_{0.47}As$/AlAs Resonant-Tunneling Diodes Measured by Electro-Optic Sampling Technique," *IEEE Electron Device Lett.*, vol. 16, no. 6, pp.262- 264, 1995.

[1.149] N. Shimizu, T. Nagatsuma, M. Shinagawa, T. Waho, M. Shinagawa, M. Yaita, and M. Yamamoto, "$In_{0.53}Ga_{0.47}As$/AlAs resonant tunneling diodes with switching time of 1.5ps," *Electron Lett.* vol. 31, no. 19, pp.1695- 1697, 1995.

[1.150] M. Reddy, S. C. Martin, A. C. Molnar, R. E. Muller, R. P. Smith, P. H. Siegel, M. J. Mondry, M. J. W. Rodwell, H. Kroemer, and S. J. Allen, Jr., "Monolithic Schottky-Collector Resonant Tunnel Diode Oscillator Arrays to 650GHz," *IEEE Electron Device Lett.,* vol. 18, no. 5, pp.218- 221, 1997.

[1.151] N. Orihashi, S. Suzuki, and M. Asada, “One THz Harmonic Oscillation of Resonant Tunneling Diode,” *Appl. Phys. Lett.*, vol. 87, p. 233501, 2005.

[1.152] N. Orihashi, S. Hattori, S. Suzuki and M. Asada, “Voltage-controlled sub-terahertz oscillation of resonant tunnelling diode integrated with slot antenna,” *Electron. Lett.,* vol.

41, no. 15, pp. 872-874, 2005.

[1.153] S. Suzuki, M.Asada, A. Teranishi, H. Sugiyama, and H. Yokoyama, “Fundamental oscillation of resonant tunneling diodes above 1 THz at room temperature,” *Appl. Phys. Lett.*, vol. 97, 242102, 2010.

[1.154] R. Sekiguchi, Y. Koyama, and T. Ouch, “Subterahertz oscillations from triple-barrier resonant tunneling diodes with integrated patch antennas,” *Appl. Phys. Lett.*, vol. 96, 062115, 2010.

[1.155] M. Feiginov, C. Sydlo, O. Cojocari, and P. Meissner, “Resonant-tunneling-diode oscillators operating at frequencies above 1.1 THz,” *Appl. Phys. Lett.*, vol. 99, 233506, 2011.

[1.156] M. Shiraishi, H. Shibayama, ,K. Ishigaki, S. Suzuki, M. Asada, H. Sugiyama, H. Yokoyama, “High output power (~400 μW) oscillators at around 550 GHz using large area RTD and optimized antenna structure,” *23rd International Conference on Indium Phosphide and Related Materials*, P29, Berlin, Germany, 2011.

[1.157] M. Shiraishi, S. Suzuki, and M. Asada, “High-Power Operation of Terahertz Oscillators with Resonant Tunneling Diodes Using Offset-Fed Slot Antennas and Array Configuration,” *Selected Topics in Quantum Electronics, IEEE*, vol. 19, issue 1, 2012.

[1.158] K. Ishigaki, M. Shiraishi, S. Suzuki, M. Asada, N. Nishiyama, and S. Arai, “Direct intensity modulation and wireless data transmission characteristics of terahertz-oscillatinog resonant tunneling diodes,” *Electron. Lett.*, vol. 48, no. 10, pp. 582-583, 2012.

[1.159] H. Kanaya, H. Shibayama, R. Sogabe, S. Suzuki , and M. Asada, “Fundamental Oscillation up to 1.31 THz in Resonant Tunneling Diodes with Thin Well and Barriers,” *Appl. Phys. Express*, vol. 5, 124101, 2012.

[1.160] Y. Koyama, R. Sekiguchi, and T. Ouchi, “1.4 THz oscillations from RTD oscillators with integrated patch antennas,” *Appl. Phys. Express*, vol. 6, 064102, 2013.

[1.161] S. Suzuki, M. Shiraishi, H. Shibayama, and M. Asada, “High-Power Operation of Terahertz Oscillators with Resonant Tunneling Diodes Using Offset-Fed Antennas and Array Configuration” *IEEE J. Sel. Top. Quantum Electron.*, vol. 19, 8500108, 2013.

[1.162] H. Kanaya, R. Sogabe, S. Suzuki, and M. Asada, ” Fundamental Oscillation up to 1.42 THz in Resonant Tunneling Diodes by Optimized Collector Spacer Thickness,” *J. Infrared Millimeter. Terahertz Waves*, vol. 35, 425, 2014.

[1.163] M. Feiginov, H. Kanaya, S. Suzuki, and M. Asada, ”Operation of resonant-tunneling diodes with strong back infection from the collector at frequencies up to 1.46 THz” *Appl. Phys. Lett.*, 104, 243509, 2014 .

[1.164] T. Maekawa, H. Kanaya, S. Suzuki, and M. Asada, “Frequency increase in terahertz oscillation of resonant tunneling diode up to 1.55 THz by reduced slot-antenna length,” *Electronics Lett.*, vol. 50, issue 17, pp.1214-1216, 2014.

[1.165] Y. Ikeda, S. Kitagawa, K. Okada, S. Suzuki, and M. Asada, ”Direct intensity modulation of resonant-tunneling-diode terahertz oscillator up to ~30 GHz,” *IEICE Electron. Express*, 12, 20141161, 2015.

[1.166] S. Kitagawa, S. Suzuki, and M. Asada, “Wide-range varactor-tunned terahertz oscillator using resonant tunneling diode,” *J. Infrared Millimeter. Terahertz Waves*, vol. 35, 445, 2014.

[1.167] H. Kanaya, T. Maekawa, S. Suzuki, and M. Asada, ” Structure dependence of oscillation characteristics of resonant-tunneling-diode terahertz oscillators associated with intrinsic and extrinsic delay times” *Jpn. J. Appl. Phys.*, vol. 54, 094103, 2015.

[1.168] K. Kasagi, S. Suzuki, and M. Asada, “Array Configuration Using Resonant-Tunneling-Diode Terahertz Oscillator Integrated Patch Antenna,” *Int. Conf. Infrared, Millimeter, and Terahertz Wave*, TS-41, Hong Kong, China, 2015.

Chapter 2

[2.1] N. Orihashi, S. Suzuki, and M. Asada, “One THz Harmonic Oscillation of Resonant Tunneling Diodes,” *Appl. Phys. Lett.*, vol. 87, p. 233501, 2005.

[2.2] D. B. Rutledge, D. P. Neikirk, and D. P. Kasilingam, “Integrated-circuit antennas,” *Infrared and Millimeter Waves*, ed. by K. J. Button, chap. 1, vol. 10, Academic, Orland, 1983.

[2.3] Y. Ikeda, S. Kitagawa, K. Okada, S. Suzuki, and M. Asada, ”Direct intensity modulation of resonant-tunneling-diode terahertz oscillator up to ~30 GHz,” *IEICE Electron. Express*, vol. 12, 20141161 (2015).

[2.4] H. Sugiyama, H. Matsuzaki, Y. Oda, H. Yokoyama, T. Enoki and T. Kobayashi, “Metal-Organic Vapor-Phase Epitaxy Growth of InP-Based Resonant Tunneling Diodes with a Strained $In_{0.8}Ga_{0.2}As$ Well and AlAs Barriers,” *Jpn. J. Appl. Phys.*, vol. 44, pp. 7314-7318, 2005.

[2.5] M. Asada, S. Suzuki, and N. Kishimoto, “Resonant Tunneling Diodes for Sub-Terahertz and Terahertz Oscillators,” *Jpn. J. Appl. Phys.*, vol. 47, pp. 4375-4384, 2008.

[2.6] M. Asada, S. Suzuki, in *Handbook of Terahertz Technology*, ed. H. J. Son and T. Nagatsuma (Pan Stanford Publishing, Singapore), pp. 151-185, 2015.

[2.7] M. Tsuchiya and H. Sakaki, “Dependence of resonant tunneling current on well widths in AlAs/GaAs/AlAs double barrier diodes structure,” *Appl. Phys. Lett.*, vol. 49, 88, 1986.

[2.8] H. Kanaya, H. Shibayama, R. Sogabe, S. Suzuki, and M. Asada, “Fundamental Oscillation up to 1.31 THz in Resonant Tunneling Diodes with Thin Well and Barriers,” *Appl. Phys. Express*, vol. 5, 124101, 2012.

[2.9] M. Tsuchiya and H Sakaki, “Precise Control of Resonant Tunneling Current in AlAs/GaAs/AlAs Double Barrier Diodes with Atomically-Controlled Barrier Widths,” *Jpn. J. Appl. Phys.*, vol. 25, no. 3, L185-L187, 1986.

[2.10] S. Suzuki, M. Asada, A. Teranishi, H. Sugiyama, and H. Yokoyama, “Fundamental oscillation of resonant tunneling diodes above 1 THz at room temperature,” *Appl. Phys. Lett.*, vol. 97, p. 242102(1-3), 2010.

[2.11] H. Kanaya, R. Sogabe, S. Suzuki, and M. Asada,” Fundamental Oscillation up to 1.42 THz in Resonant Tunneling Diodes by Optimized Collector Spacer Thickness,” *J. Infrared Millimeter. Terahertz Waves,* vol. 35, 425 (2014).

[2.12] E. R. Brown, W. D. Goodhue, and T. C. L. G. Sollner: "Fundamental oscillations up to 200GHz in resonant tunneling diodes and new estimates of their maximum oscillation frequency from stationary-state tunneling theory," *J. Appl. Phys.,* vol. 64, no. 3, 1519 1988.

[2.13] T. P. Pearsall, R. Bisaro, P. Merenda, G. Laurencin, R. Ansel, J. C. Portal, C. Houlbert, and M. Quillec, “The characterization of $Ga_{0.47}In_{0.53}As$ grown lattice-matched on InP substrates,” *Inst. Phys. Conf. Ser.*, vol. 45, 94 ,1979.

[2.14] T. P. Pearsall and J. P. Hirtz, “The carrier mobilities in $Ga_{0.47}In_{0.53}As$ grown by organo-metallic CVD and liquid-phase epitaxy,” *J. Cryst. Growth,* vol. 54, 127, 1981.

[2.15] E. R. Brown, T. C. L. G. Sollner, C. D. Parker, W. D. Goodhue, and C. L. Chen, "Oscillations up to 420GHz in GaAs/AlAs resonant tunneling diodes," *Appl. Phys. Lett.*, vol. 55, no. 17, 1989.

[2.16] M. Reddy, S. C. Martin, A. C. Molnar, R. E. Muller, R. P. Smith, P. H. Siegel, M. J. Mondry, M. J. W. Rodwell, H. Kroemer, and S. J. Allen, Jr., "Monolithic Schottky-Collector Resonant Tunnel Diode Oscillator Arrays to 650 GHz," *IEEE Electron Device Lett.*, vol. 18, no. 5, pp. 218- 221, 1997.

[2.17] R. Sekiguchi, Y. Koyama, and T. Ouch, “Subterahertz oscillations from triple-barrier resonant tunneling diodes with integrated patch antennas,” *Appl. Phys. Lett.*, vol. 96, 062115, 2010.

Chapter 3

[3.1] M. Tsuchiya and H. Sasaki, "Dependence of resonant tunneling current on well widths in AlAs/GaAs/AlAs double barrier diodes structures," *Appl. Phys. Lett.*, vol. 49, 88, 1986.

[3.2] M. Tsuchiya and H Sakaki, "Precise Control of Resonant Tunneling Current in AlAs/GaAs/AlAs Double Barrier Diodes with Atomically-Controlled Barrier Widths," *Jpn. J. Appl. Phys.*, vol. 25, no. 3, L185-L187, 1986.

[3.3] H. Mizuta and T. Tanoue, *The Physics and Applications of Resonant Tunneling Diodes,* Cambridge University Press, 1995.

[3.4] S. Suzuki, M. Asada, A. Teranishi, H. Sugiyama, and H. Yokoyama, "Fundamental oscillation of resonant tunneling diodes above 1 THz at room temperature," *Appl. Phys. Lett.*, vol. 97, 242102, 2010.

[3.5] H. Kanaya, H. Shibayama, R. Sogabe, S. Suzuki, and M. Asada, "Fundamental Oscillation up to 1.31 THz in Resonant Tunneling Diodes with Thin Well and Barriers," *Appl. Phys. Express*, vol. 5, 124101, 2012.

[3.6] A. Teranishi: Dr. Thesis, Graduate School of Interdisciplinary Science and Engineering, Tokyo Institute of Technology, Tokyo, Japan, 2012 [in Japanese].

[3.7] N. Kotera, H. arimoto, N. Miura, K. Shibata, Y. Ueki, K. Tanaka, H. Nakamura, T. Mishima, K. Aiki, M. Washima, "Electron effective mass and nonparabolicity in InGaAs/InAlAs quantum wells lattice-matched to InP," *Physica. E,* vol. 11, pp. 219-223, 2001.

[3.8] Y. A. Goldberg and N. M. Schmidt: *in handbook Series on Semiconductor Parameters*, ed. M. Levinshtein, S. Rumyantsev, and M Shur, World Scientific Publishing, Singapore, 1996.

[3.9] A. Teranishi, S. Suzuki, K. Shizuno, M. Asada, H. Sugiyama, and H. Yokoyama, "Estimation of Transit Time in Terahertz Oscillating Resonant Tunneling Diodes with Graded Emitter and Thin Barriers," *IEICE Trans. Electron.*, vol. E95-C, 2012.

Chapter 4

[4.1] N. Kishimoto, S. Suzuki, A. Teranishi, and M. Asada, “Frequency Increase in Resonant Tunneling Oscillators in Sub-THz and THz range Using Thick Spacer Layers,” *Appl. Phys. Express*, vol. 1, 042003, 2008.

[4.2] A. Teranishi, S. Suzuki, K. Shizuno, M. Asada, H. Sugiyama, and H. Yokoyama, “Estimation of Transit Time in Terahertz Oscillating Resonant Tunneling Diodes with Graded Emitter and Thin Barriers,” *IEICE Trans. on Electronics,* vol. E95-C, no.3 pp. 401-407, 2012.

[4.3] M. Feng and W. Snodgrass, ”InP Pseudormorphic Heterojunction Bipolar Transistor (PHBT) with f_t >750 GHz,” *19th Int. Conf. Indium Phosphide and Related Materials*, p. 399, 2007.

[4.4] J. A. del Alamo, “Nanometre-scale electronics with Ⅲ-Ⅴ compound semiconductors,” *Nature,* vol. 479, 317, 2011.

[4.5] H. Ito, T. Furuta, and T. Ishibashi,”InP/InGaAs uni-travelling-carrier photodiode with 310 GHz bandwidth,” *Electron. Lett.*, vol. 36, 1809, 2000.

.

Chapter 5

[5.1] E. R. Brown, W. D. Goodhue, and T. C. L. G. Sollner, “Fundamental oscillations up to 200 GHz in resonant tunneling diodes and new estimate of their maximum oscillation frequency from stationary-state tunneling theory,” *J. Appl. Phys.*, vol. 64, 1519, 1988.

[5.2] T. P. Pearsall, R. Bisaro, P. Merenda, G. Laurencin, R. Ansel, J. C. Portal, C. Houlbert, and M. Quillec, “The characterization of $Ga_{0.47}In_{0.53}As$ grown lattice-matched on InP substrates,” *Inst. Phys. Conf. Ser.*, vol. 45, 94, 1979.

[5.3] T. P. Pearsall and J. P. Hirtz, “The carrier mobilities in $Ga_{0.47}In_{0.53}As$ grown by organo-metallic CVD and liquid-phase epitaxy,” *J. Cryst. Growth*, vol. 54, 127, 1981.

[5.4] T. Maekawa, H. Kanaya, S. Suzuki, and M. Asada, “Frequency increase in terahertz oscillation of resonant tunneling diode up to 1.55 THz by reduced slot-antenna length,” *Electronics Lett.*, vol. 50, issue 17, pp.1214-1216, 2014.

[5.5] T. Maekawa, H. Kanaya, S. Suzuki, and M. Asada, “1.92 THz Oscillator using Resonant Tunneling Diode Integrated with Slot Antenna with Reduced Conduction Loss,” *Joint Symp. MTSA and TeraNano*, P1-7, Okinawa, Japan, July, 2015.

[5.6] S. Suzuki, M. Shiraishi, H. Shibayama, and M. Asada, “High-Power Operation of Terahertz Oscillators with Resonant Tunneling Diodes Using Offset-Fed Antennas and Array Configuration” *IEEE J. Sel. Top. Quantum Electron.*, vol. 19, 8500108, 2013.

[5.7] H. Shibayama, M. Shiraishi, S. Suzuki, and M. Asada, “Dependence of Output Power on Slot Antenna Width in Terahertz Oscillating Resonant Tunneling Diodes,” *J. Infrared. Milli. Terahz Waves*, vol. 33, pp. 475- 478, 2012.

Appendix: Fabrication process and measurement system

Fabrication process

0 Preparing substrate

0.1 Wafer cutting

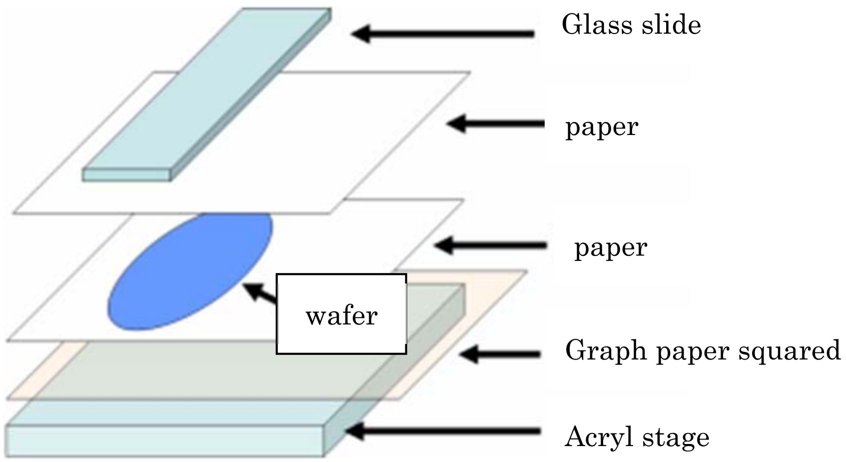

Fig. A.1 Cutting wafer

Cut the wafer with a surgical knife as shown in Fig A.1

0.2 Wafer cleaning

a Cleaning by Deionized (DI) water (>18 MΩ) , 8 times flashing in a beaker

b 5-min ultrasonic cleaning (power 40%)

Repeat a→b 2sets

Memo: For removing water-soluble materials and particles by ultra sonic cleaning

If the ultra sonic power is over 50%, the wafer may be broken and if

there is insufficient water in the bass of ultra sonic machine, add DI water.

Cleaning by acetone and methyl

For removing organic matter by using organic solvent

Methyl cleaning 3 times

Acetone cleaning 3 times

Acetone boiling 2 times (Temp. 130 ℃, 5 min)

Memo: Cooling by the acetone before pick up a beaker to prevent explosive boil

Methyl cleaning 2 times

Brow dry by N_2 Gun

Memo: If the surface is smoked because of air moisture, repeat methyl cleaning.

1 Fabrication of Upper electrodes (UE), alignment marks, and TLM patterns

1.1 Resist coating

Bottom layer resist: PMGI SF6

Caution: Use the resist within expiration date, Blow your wafer for remove dust

Spin coating: 1st 1000 rpm 3sec, 2nd 3000 rpm 60sec (thickness ~300 nm)

Pre-baking: Hotplate 250℃ 5 min

Top layer resist: ZEP 520

Spin coating: 1st 1000 rpm 3sec, 2nd 2000 rpm 60 sec (~500 nm)

Pre-baking: hotplate 180℃ 5 min

Memo: Before coating resist, blow your wafer by blower to get particles off

1.2 Electron-beam (EB) lithography

Model: JEOL JBX6300

Exposure value: 75 $\mu C/cm^2$ @ 50 kV EB, or 130 $\mu C/cm^2$ @ 100 kV EB

Memo: Check the most recent condition

Exposure condition: Current 3000 pA (shot rank, 128)

Field size (125,125)

1.3 Development

Top layer development

Xylene, 3.5 min, with stirring

Rinse, Isopropyl alcohol (IPA), 15 sec, with stirring

Bottom layer development

MFCD-26, 30 sec (or more), without stirring

Rinse, IPA, 15 sec (2 set with 2 beakers), without stirring

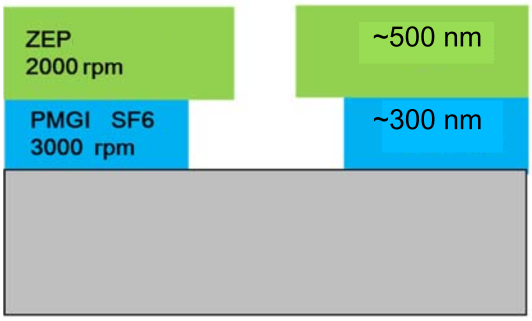

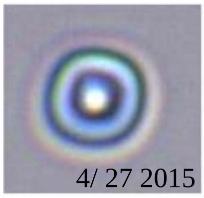

Fig. A.2 Schematic structure and picture near RTD mesa of resist after bottom resist development

1.4 Surface cleaning

O_2 Ashing for removing resist

Flow meter value: 50 sccm

Power: 50 W

Time: 1 min

Memo: If the plasma color is purple, check the O_2 flow and seal of O ring

Wet cleaning for good contact resistance

Cleaning liquid: HCL:H_2O = 1:5 (<4℃ and after cooling by ice over 30 min)

Time: 2 min without stirring

Blow dry with N_2 (without DI rinse)

Set the wafer in electron-beam evaporator as soon as possible

1.5 Evaporation of metals for UEs, marks, TLM

Evaporator: Electron-beam evaporator (4 kV)

Degree of vacuum: $<5 \times 10^{-7}$ torr

Metal thickness (nm): Ti/Pd/Au = 20/20/200 (5 min interval)

Rate: Ti & Pd: 0.7~1.5 Å/sec, Au: 4~7 Å/sec

Memo: Haas liners are W for Ti, or Ta for Pd and Au

Liftoff: ZDMAC, 130 ℃, ~10 min

Cleaning: Boiling by acetone for 5 min and Methyl cleaning ×3

2 RTD mesa fabrication

2.1 Wet etching

Check the metal height and *I*-*V* characteristics of TLM pattern before etching

Etchant: H_2SO_4:H_2O_2:H_2O=1:1:40 (<4℃and after cooling over 30 min)

Rate: ~1 nm/sec

Time: usually >100 sec (Divide the etching time for preventing over etching)

Rinse: DI water, 15 sec, 2 sets

Check the etching height by contact-type thickness meter each etching

I-*V* check (Dummy RTD and TLM)

2.2 RTD mesa area check

Observation of RTD mesa from the side by scanning electron microscope SEM

Model: S-4500 (Hitachi High Tech)

3 Fabrication of lower electrode

3.1 Spin coating

Bottom resist: PMGI SF6

1st 1000 rpm 1sec, 2nd 2000 rpm 60sec (~300 nm)

Pre-baking : Hot plate 250℃ 5 min

Top layer resist: ZEP-520A

1st 1000 rpm 3sec, 2nd 2000 rpm 60 sec (~500 nm)

Pre-baking: Hot plate 180℃ 5 min

3.2 EB lithography of lower electrode

Exposure value：80 μC/cm2

Fieldsize(125,125), Subfield size(125,125)

Current 3000 pA (near antenna), area exposure, shot rank 128

15 nA(ohter parts), area exposure, shot rank 128

3.3 Development of lower electrode

Top layer: Xcylene: 3 min 30 sec with stirring

Rinse: IPA 15 sec with stirring

Bottom layer: MFCD-26 30+x sec

Rinse: DI 15 sec w/o stirring (2 sets), O_2 asshing: 50 sccm, 50 W, 1 min

3.4 Evaporation of lower electrode

Metal: Ti/Pd/Au/Ti = 20/20/50/5 nm

Memo: 5-nm Ti for adhension with SiO_2

Lift off until take metals off at 150℃by ZDMAC

Cleaning by acetone boiling and methanol

Blow dry with N_2

3.5 *I-V* measurement

After checking the IV date, you can use EXCEL macro to arrange the data. Name devices such as a1 ~ a12 to work the macro.

4 Device isolation

4.1 SiO_2 deposition for the mask of reactive ion etching

Model: PD-100ST (Samco)

Temperature: 145 ℃

Power 30 W,

Pressure: 15 Pa

Gas: TEOS:O_2 = 2 : 60 sccm

Time: 3 min 30 sec (Thickness: ~50 nm)

4.2 Spin coating

Resist: ZEP 520A 1st 1000 rpm 3sec, 2nd 2000 rpm (~500 nm)

Prebaking: Hotplate 180℃ 5 min

4.3 EB lithography

Exposure value: 75 $\mu C/cm^2$ @ 50 kV EB, or 130 $\mu C/cm^2$ @ 100 kV EB

Exposure condition:

Current: 15 nA (Area exposure, shot rank 128)

4.4 Development of device isolation pattern

Developer: Xylene, 3 min with stirring

Rinse: IPA 15 sec with stirring

Blow by dry N_2

Check the pattern by microscope and height of resist

4.5 Patterning of SiO_2 mask

Reactive Ion Etching of SiO_2 for device isolation mask by ZEP resist

Model: RIE-10NR (Samco)

Gas: CF_4, 30 sccm, 0.1 Pa, 60 W, ~9 min

Liftoff

Boiling in ZDMAC at 130 degrees Celsius for removing ZEP resist

Acetone-boiling cleaning and 3-times methyl alcohol cleaning

4.6 Device isolation by RIE

Dry etching by RIE

Model: RIE-10NR (Samco)

Etching recipe

Check the Table.1 (Recipe of dry etching for InGaAs)

1 set for checking etching rate (Etching rate ~100 nm/ set)

Dry etching by RIE, 2~3 times, for device isolation with etching conduction layer

Memo: Check the leak current between a device and the next.

Surface cleaning (If the surface of InP has leak path)

Etchant: HCl

Time: ~1 sec

Rinse: DI 15 sec (stirring)

Acetone boiling & methyl cleaning

Table. A. 1. Dry etching recipe

No.	1	2	3	4	5	6	7
O2	30sccm		30sccm		30sccm		30sccm
CH4		10sccm		10sccm		10sccm	
H2		40sccm		40sccm		40sccm	
Pressure	10Pa	3Pa	10Pa	3Pa	10Pa	3Pa	10Pa
Power	50W	300W	50W	300W	50W	300W	50W
Time	1min	2min	2min	2min	2min	2min	10min

5 Deposition of passivation layer (SiO_2 ~50 nm)

Model: PD-100ST (Samco)

Temperature: 145 ℃

Power 30 W,

Pressure: 15 Pa

Gas: TEOS:O_2 = 2 : 60 sccm

Time: 3 min 30 sec (Thickness: ~50 nm)

6 Fabrication of contact hole

6.1 Spin coating

1^{st} Resist: PMMA A8 100%

1^{st} 1000 rpm 1 sec, 2^{nd} 1500 rpm 60 sec (~ 1 μm)

Pre-baking: hotplate 180 degrees

Time: 60 sec

2^{nd} Resist: PMMA A8 100%

1^{st} 1000 rpm 1 sec, 2^{nd} 1500 rpm 60 sec (~ 1 μm)

Pre-baking: hotplate 180 degrees

Time: 90 sec

Memo: thick resist for preventing RIE damage of SiO_2

5.2 EB lithography of contact hole

Exposure value：550 μC/cm^2 @50-kV EB, 900 μC/cm^2 @ 100-kV EB

Current: Mesa part 3000 pA,

Others 15 nA for reduction in exposure time

Development MIBK:IPA=1: 3　90 sec (Stirring)

Rinse: IPA 15sec（stirring）

Blow dry with N_2

5.3 Dry etching by RIE

Dry etching of SiO_2 masked by PMMA A8

Model: RIE-10NR (Samco)

Gas: CF_4 30 sccm,

Pressure: 0.1 Pa

Power : 60 W

Time: 9 min or more

Memo: The etching rate above is SiO_2 : PMMA = 1:5

Check wafer by microscope and contact hole by IV measurement

Cleaning by 5 min acetone boiling and 2 times methanol

6 Formation of air bridge with MIM

6.1 Spin coating

Bottom resist: PMMA A8

1st 1000 rpm 1sec, 2nd 2000 rpm 60sec (~700 nm)

Pre-baking : Hot plate 180℃ 3 min

1st Middle layer:PMGI-SF9

1st 1000 rpm 1sec, 2nd 2000 rpm 60sec (~700 nm)

Pre-baking: Hot plate 180℃ 5 min

2nd Middle layer:PMGI-SF9

1st 1000 rpm 1sec, 2nd 2000 rpm 60sec (~700 nm)

Pre-baking: Hot plate 180℃ 5 min

Top layer: ZEP:Anisole=2:1 (thin resist for preventing resist crack)

1st 1000 rpm 1sec, 2nd 3000 rpm 60sec (~350 nm)

Pre-baking: Hot plate 180℃ 5 min

6.2 EB lithography of top layer

Exposure value: 75 μC/cm^2 @ 50 kV EB, or 110 μC/cm^2 @ 100 kV EB

Memo: Check the most recent condition

Exposure condition: Current 3000 pA (shot rank, 128)

Top layer development

Xylene, 3.5 min, with stirring

Rinse: IPA 15 sec with stirring

Middle layer development

MFCD-26, 15sec, without stirring

Rinse: IPA 15 sec 2set without stirring

If it is insufficient add the development

Check the resist height

6.3 EB lithography of bottom layer

Exposure value: 500 μC/cm^2 @ 50 kV EB, or 750 μC/cm^2 @ 100 kV EB

Memo: Check the most recent condition

Exposure condition: Current 3000 pA (shot rank, 128)

Bottom layer development

MIBK:IPA=1:3, 90 sec, with stirring

Rinse: IPA 15 sec with stirring

O_2 asshing: 50 sccm, 50 W, 1 min

6.4 Evaporation of MIM+bridge metals

Metal: Cr/Au =10 nm/1500 nm (250 nm x 6 sets)

Lift off

Remover: ZDMAC@130℃

Cleaning by boiling acetone and RT methanol

Blow dry with N_2

Check the height of MIM

Check the *I-V* between upper electrode and MIM

Memo: If you check the *I-V* characteristics of RTD for oscillator, don't connect a RTD and an InGaAs resistance.

Completion of fabricating

Measurement system

Measurement system of frequency and output power is shown in Figs. A.3 and A.4. Fourier transform infrared spectrometer (FARIS-1, JASCO) is used to measure oscillation frequency. Bolometer (HDL-5, Infrared Laboratories) and power meter (PM5 & PM3, VDI-Erickson) is used for obtaining output power. Oscillators on an InP wafer are set on high resistivity Si hemispherical lens. Almost all of the output power (~98%) is radiated into substrate because of high permittivity (Relative permittivity $\varepsilon_r = 12.1$) as mentioned in Chapter 2. InP and Si has almost same refractive index but there is large difference of refractive index between Si lens and air which causes the Fresnel loss, thus transmission rate is calculated as about 70 %. The off-axis parabolic mirror which focal length of 5.1 cm and the diameter of 7.6 cm collects about 36%. The value is estimated by the optical system and a radiation pattern calculated with a model of simple slot antenna in HFSS. The off-axis parabolic mirror changed the output radiation into parallel beam because of the FTIR requirement. In output power measurement, the parallel beam is focused into a detector with Tsurupica lens (the diameter and focal point are 10 cm). Rock-in technique is used for reduction in noise with pulse generator. Reached output power is $0.98 \times 0.7 \times 0.36 = 0.25$ with neglecting the attenuation of atmosphere and lens.

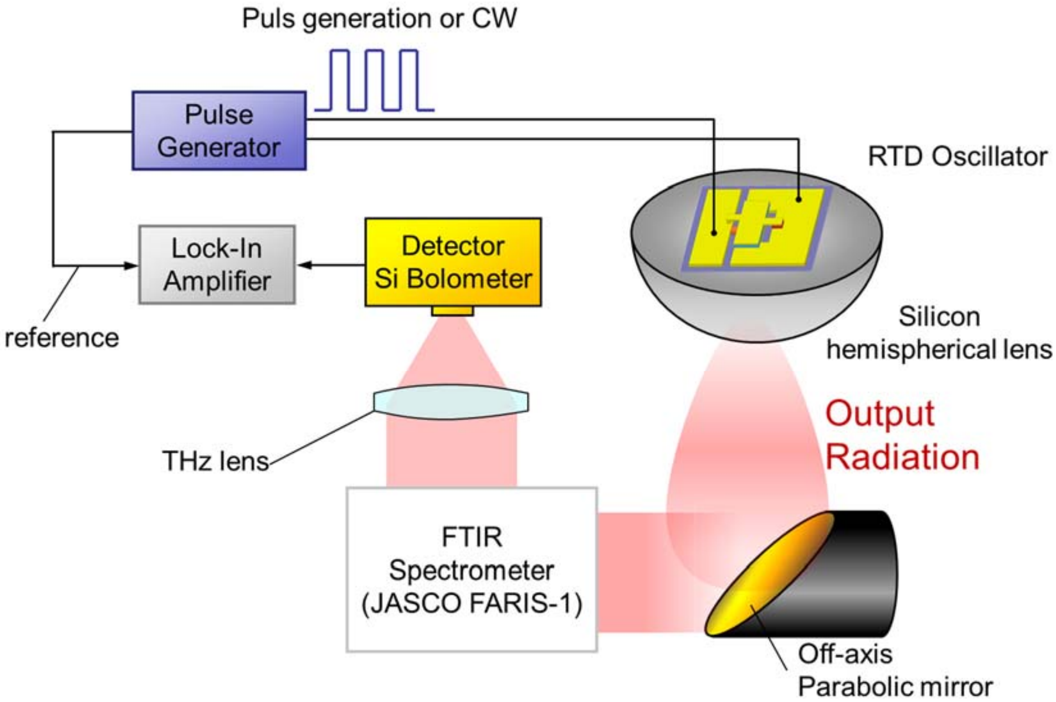

(a) Frequency measurement

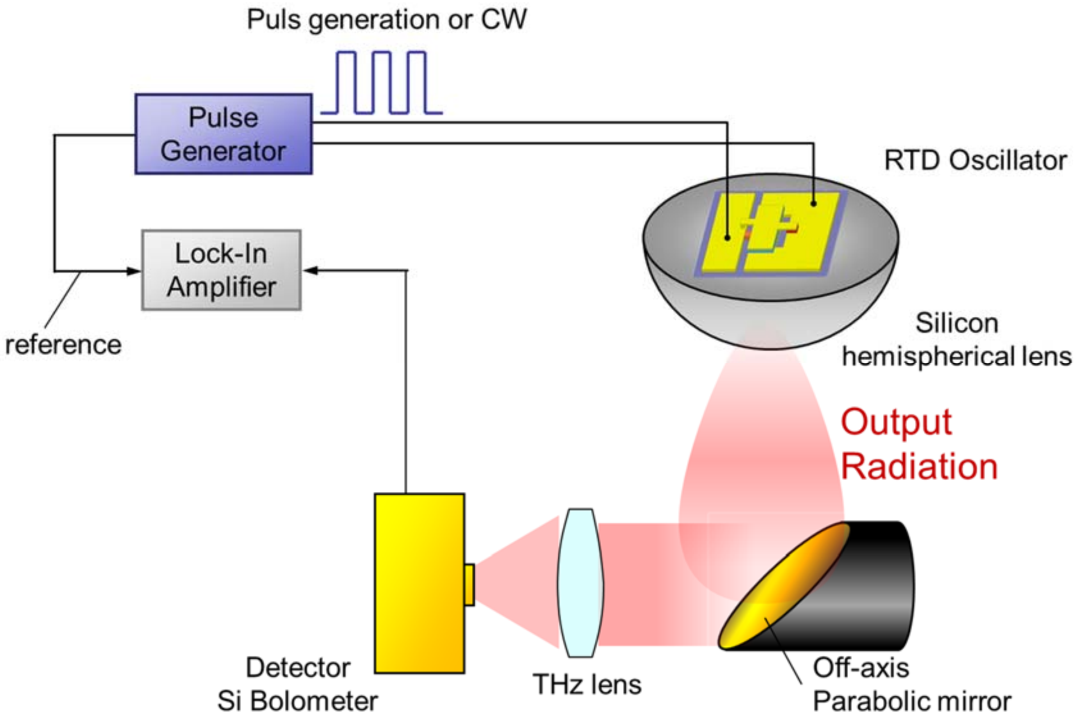

(b) Power measurement

Fig A.3 Schematic diagram of measurement system for oscillation frequency and output power.

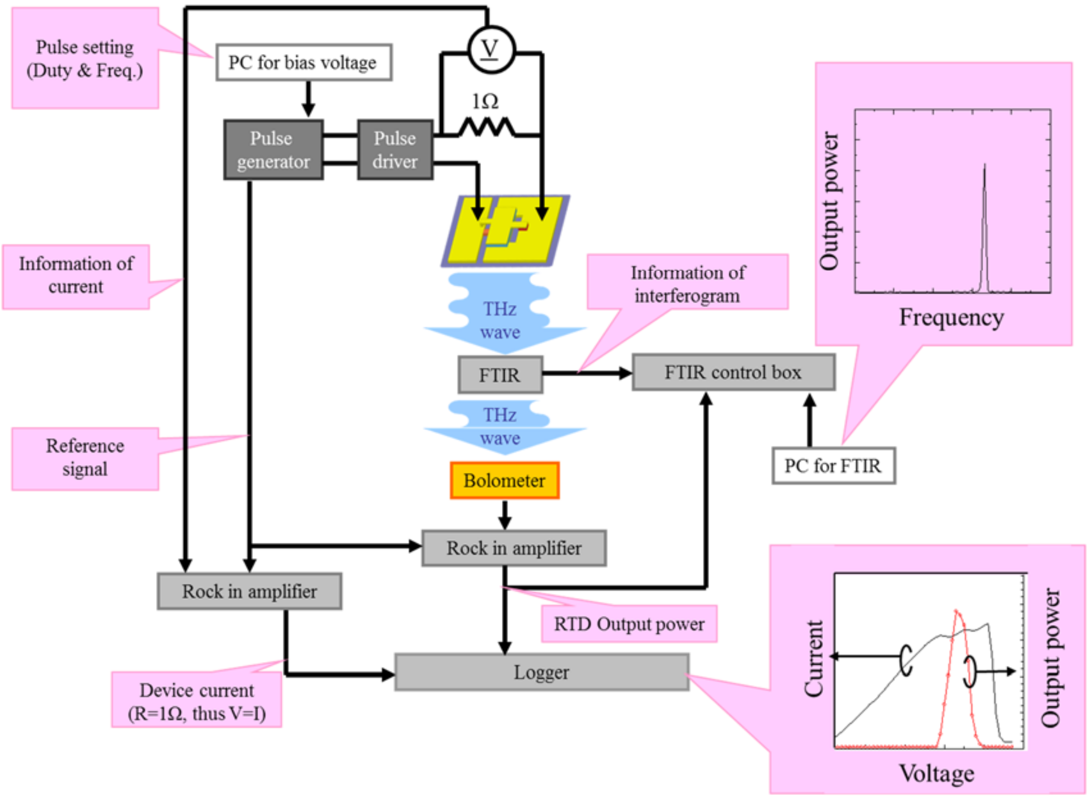

Fig A.4 Precise measurement system of oscillation frequency.

Publication list

Journal Paper

(1) H. Kanaya, H. Shibayama, R. Sogabe, S. Suzuki, M. Asada, “Fundamental Oscillation up to 1.31 THz in Resonant Tunneling Diodes with Thin Well and Barriers,” *Appl. Phys. Express*, Vol. 5, No. 12, 124101, 2012.

(2) H. Kanaya, S. Suzuki, M. Asada, “Terahertz oscillation of resonant tunneling diodes with deep and thin quantum wells,” *Electron. Express*, Vol.10, No.18, pp. 1-7, 2013.

(3) M. Asada, H. Kanaya, and S. Suzuki, “Terahertz Emission from Resonant Tunneling Diodes without Satisfying Oscillation Condition,” *Jpn. J. Appl. Phys.*, Vol. 52, 100210, 2012.

(4) H. Kanaya, S. Suzuki, M. Asada, “Fundamental Oscillation up to 1.42THz in Resonant Tunneling Diodes by Optimizing Collector Spacer Thickness,” *J. Infrared, Millimeter, and Terahertz Waves,* Vol.35, Issue 5, pp. 425-431, 2014.

(5) M. Feiginov, H. Kanaya, S. Suzuki, M. Asada, “Operation of resonant-tunneling diodes with strong back injection from the collector at frequencies up to 1.46 THz,” *Appl. Phys. Lett.*, Vol. 104, Issue 24, 243509, 2014.

(6) T. Maekawa, H. Kanaya, S. Suzuki, M. Asada, “Frequency increase in terahertz oscillation of resonant tunneling diode up to 1.55 THz by reduced slot-antenna length,” *Electron. Lett.*, Vol. 50, No. 17, 1214-1216, 2014.

(7) H. Kanaya, T. Maekawa, S. Suzuki, M. Asada, "Structure Dependence of Oscillation Characteristics of Resonant-Tunneling-Diode Terahertz Oscillators Associated with Intrinsic and Extrinsic Delay Times,” *Jpn. J. Appl. Phys.*, Vol. 54, 094103, 2015.

International conference

(1) H. Kanaya, H. Shibayama, K. Shizuno S. Suzuki, M. Asada, “Increase in Output Power Using Thin-Well Resonant Tunneling Diodes,” *EOS Topical Meeting on Terahertz Science & Technology (EOS-TST 2012)*, 5299, Prague, Czech Republic, 2012.

(2) H. Kanaya, H. Shibayama, S. Suzuki, M. Asada, “Fundamental Oscillation up to 1.31 THz in Thin-Well Resonant Tunneling Diodes,” *Int. Conf. Indium Phosphide and Related Materials (IPRM 2012)*, Tu-1E.5, Santa Barbara, USA, 2012.

(3) H. Kanaya, S. Suzuki, M. Asada, “Frequency increase in terahertz oscillating resonant tunneling diodes with keeping bias voltage by deep- and thin-well structure,” *Int. symp. Frontiers in THz Tech. (FTT 2012)*, Pos 1.14, Nara, Japan, 2012.

(4) H. Kanaya, R. Sogabe, T. Maekawa, S. Suzuki, and M. Asada, “Frequency increase in resonant-tunneling-diode terahertz oscillators using optimum collector spacer,” *Int. Conf. on Indium Phosphide and Related Materials (IPRM 2014)*, Mo-C1-1, Montpellier, France, 2014.

(5) H. Kanaya, T. Maekawa, S. Suzuki, M. Asada, “Dependence of dwell time on well thickness in terahertz oscillating resonant tunneling diodes,” *5th International Symposium on Terahertz Nanoscience (TeraNano 5)*, Martinique, France, 2014.

(6)T. Maekawa, H. Kanaya, R. Sogabe, S. Suzuki, and M. Asada, “Oscillation of Resonant Tunneling Diode up to 1.55 THz by Optimized Slot Antenna Length” *4th EOS Topical Meeting on Terahertz Science & Technology (EOS-TST 2014)* , Italy , 2014.

(6) H. Kanaya, T. Maekawa, S. Suzuki, and M. Asada, “Structure dependence of oscillation characteristics in resonant-tunneling-diode terahertz oscillators and fundamental oscillation up to 1.86 THz,” *Topical Workshop on Heterostructure Microelectronics (TWHM 2015)*, CP-6, Takayama, Japan, 2015.

(7) T. Maekawa, H. Kanaya, S. Suzuki and M. Asada, "1.92 THz Oscillator using Resonant Tunneling Diode Integrated with Slot Antenna with Reduced Conduction Loss," *The 6th Int. Symp. Terahertz Nanoscience (Teranano 2015)*, P1-7, Okinawa, Japan, 2015.

Award

(1) IPRM 2012 Best student paper award

H. Kanaya, H. Shibayama, S. Suzuki, M. Asada, "Fundamental Oscillation up to 1.31 THz in Thin-Well Resonant Tunneling Diodes," *Int. Conf. Indium Phosphide and Related Materials (IPRM 2012)*, Tu-1E.5, Santa Barbara, USA, 2012.

(2) 2013 JSAP Young Scientist Award (Koen Syorei Syo in Japanease)

H. Kanaya, R. Sogabe, S. Suzuki, and M. Asada, "Fundamental oscillation up to 1.31 THz with Thick spacer and Thin Well," *60th JSAP Spring Meeting*, 11p-B1-8, Ehime, Japan, 2013.